Assessment of the Response of Offshore Monopile Foundations to Vibratory Hammer Action

A parametric study to the response of offshore monopile foundations to a proper definition of a vibratory hammer including imperfections

MSc Thesis
Cansu Cirak

Delft University of Technology

TUDelft

Assessment of the Response of Offshore Monopile Foundations to Vibratory Hammer Action

A parametric study to the response of offshore monopile foundations to a proper definition of a vibratory hammer including imperfections

by

Cansu Cirak

Student Name	Student Number
Cansu Cirak	4403894

Thesis submitted to Delft University of Technology for the degree of
Master of Science
in Civil Engineering
to be publicly defended on 10 March 2023 at 15:00.

Thesis committee:	Dr. ir. A. Tsouvalas
	ir. A. Tsetas
	Dr. ir. S. Sánchez Gómez
Institution:	Delft University of Technology
Place:	Faculty of Civil Engineering, Delft
Project Duration:	March, 2022 - March, 2023

An electronic version of this thesis is available at http://repository.tudelft.nl.

TUDelft

Preface

This thesis is the culmination of my studies towards a Master of Science degree in Civil Engineering at the Delft University of Technology. Throughout my academic journey, I have had the opportunity to explore various aspects of civil engineering, including structural engineering with a focus on structural mechanics followed by structural dynamics. My curiosity for this latter field has led me to delve deeper into the topic of pile driving and the performance of pile foundations.

The research presented in this thesis focuses on the behavior of pile foundations under dynamic loading conditions from a vibratory hammer. Specifically, the study investigates the force transfer from the hammer to the pile, the effect of misalignment on power consumption, and the activation of the elastomere pads in the vibratory hammer. The research builds upon existing knowledge in the field and aims to contribute to the understanding of the response of vibratory driven monopiles to the action from vibratory hammers.

Throughout the research process, I have been fortunate to receive guidance and support from various individuals. I would like to express my sincere gratitude to my supervisor, Athanasios Tsetas, for his invaluable advice, feedback, and encouragement. He provided guidance throughout my entire thesis and always made time for me, even when he was busy. I would also like to thank my committee members, Apostolos Tsouvalas and Sergio Sánchez Gómez, for their insightful comments and suggestions.

I would like to express my gratitude to my family and friends for their constant support and encouragement throughout my academic journey. They have been the driving force behind my accomplishments, and I am forever grateful. I would like to thank my sister Gulsah for always being there for me with my nephew Muhammed who always cheered me up after long days. My brothers Haydar and Serdar who love to criticize me in every move I make, but that keeps me sharp, thank you. Not to forget my dear friends Firas and Karim who became family, and would annoy the hell out of me but at the same time I could always count on, no matter what. And finally, my biggest support during my TU Delft journey, my friend Hagar, who would **tirelessly** help me in every way she could, I can not thank you enough.

Finally, I would like to express my heartfelt gratitude to my mother, who has been my pillar of strength during challenging times. When I had to leave high school at a very young age due to unavoidable circumstances, she stood by me and motivated me to restart my education all over again from scratch at the age of 21, without even a high school diploma in hand. Looking back now, almost thirteen years later, I can proudly say that I have completed my studies, and while my loved ones are likely more relieved than I am, I am immensely thankful for their unwavering patience and support throughout my journey.

Cansu Cirak
Delft, March 2023

Summary

The growing demand for wind energy has led to the need for larger offshore wind turbines. As a result, there is an increasing demand for larger monopiles to support the turbines. Vibratory pile driving is a common technique for installing mono piles. However, the current engineering models used for vibratory pile driving are generally designed for small diameter monopiles and may not be applicable to larger piles. In addition, the vibratory action produced by counter-rotating eccentric masses in the hammer can cause unintended bending motions in the pile if there is a slight misalignment. The current models do not account for the more complex vibratory system and multiple hammers needed for larger diameter monopiles. Therefore, this study aimed to investigate the effects of gear misalignment on the response of monopiles under vibratory action, including these imperfections. To achieve this, a hammer model was created and coupled with a pile model and a simplified soil reaction. A parametric study was then conducted to evaluate the pile response to the modeled vibratory hammer with imperfections over a range of specified variables.

This study examined the transfer of force from the hammer to the pile and the range of driving frequencies that activate the isolation springs in the vibratory hammer. Additionally, the effect of misalignments on the power consumption of the vibratory hammer and the bending displacements caused by these misalignments were investigated.

To simulate the mono pile response, thin circular cylindrical Finite Elements were used. The study has shown that:

- In general, it was found that there was no significant impact on axial vibrations as a result of misalignment of rotating masses.
- The force transfer ratio from hammer to pile is 0.5 to 0.7 for smaller diameter piles. In the initial design phase of pile drivability prediction models, when the decision is made not to model the hammer, it is important to include force transfer ratios in simple engineering models.
- Modeling the hammer-pile-soil system with shell elements in stead of 1D rod elements yields similar trends in the responses, but the absolute response values of large diameter piles with simple 1D rod elements leads to an underestimation of the response in the lower driving frequency range and an overestimation in the higher driving frequency range.
- It was determined that even if as much as 50% of the eccentric masses are misaligned, the impact of bending vibrations on the power consumption of the vibratory hammer is insignificant. Nonetheless, bending displacement can become substantial when 6% of the eccentric masses are misaligned. As a general rule, smaller diameter piles are more susceptible to vibrations at lower frequency ranges, while larger diameters are impacted in higher frequency ranges.
- Only large diameter monopiles are susceptible to axial vibrations near their natural frequencies, while all diameter piles are affected by bending vibrations near their natural frequencies. Within the range of driving frequencies, bending vibrations are more closely spaced. This can result in a dip in the axial vibrations while a peak in the bending vibration occurs under vibratory action with misalignment, leading to relatively increasing bending displacements.
- Isolator springs are effectively activated in the region of higher driving frequencies (> 28 Hz) for large diameter monopiles. In the case of small diameter piles (< 3 m), the relative motion between suppressor housing and pile head remained above unity for all driving frequencies, meaning poor activation of the isolator springs.

Samenvatting

De groeiende vraag naar windenergie heeft geleid tot de behoefte aan grotere offshore windturbines. Als gevolg hiervan is er een toenemende vraag naar grotere monopiles om de turbines te ondersteunen. Trillend heien is een veelgebruikte techniek voor het plaatsen van monopalen. De huidige technische modellen die worden gebruikt voor het heien van trilpalen zijn over het algemeen ontworpen voor monopiles met een kleine diameter en zijn mogelijk niet toepasbaar op grotere palen. Bovendien kunnen bij een lichte afwijking van de tegengesteld draaiende excentrische massa's van de trilhamer onbedoelde buiging in de paal optreden. De huidige modellen houden geen rekening met het complexere trilsysteem en de meerdere hamers die nodig zijn voor de installatie van monopiles met een grotere diameter. Daarom was deze studie gericht op het onderzoeken van de effecten van verkeerde uitlijning van tandwielen op de respons van monopiles onder trillende werking, inclusief deze imperfecties. Hiervoor is een hamermodel gemaakt en gekoppeld aan een paalmodel en een vereenvoudigde grondreactie. Vervolgens werd een parametrische studie uitgevoerd om de paalrespons op het gemodelleerde trilhamer met imperfecties over een reeks gespecificeerde variabelen te evalueren.

In dit onderzoek is gekeken naar de krachtoverdracht van de hamer op de paal en naar het bereik van de aandrijffrequenties die de isolatieveren in het trilblok activeren. Daarnaast is het effect van uitlijnfouten op het energieverbruik van het trilblok en de buiging als gevolg van deze uitlijnfouten onderzocht.

Om de monopaalrespons te simuleren, werden dunne cirkelvormige cilindrische Eindige Elementen gebruikt. De studie heeft aangetoond dat:

- In het algemeen werd gevonden dat er geen significante invloed was op axiale trillingen als gevolg van een verkeerde uitlijning van roterende massa's.
- De krachtoverbrengingsverhouding van hamer naar paal is 0,5 tot 0,7 voor palen met een kleinere diameter. In de initiële ontwerpfase van voorspellingsmodellen voor de heibaarheid van palen, wanneer wordt besloten om de hamer niet te modelleren, is het belangrijk om krachtoverbrengingsverhoudingen op te nemen in eenvoudige technische modellen.
- Het modelleren van het hamer-paal-grondsysteem met schaalelementen in plaats van 1D staafelementen geeft vergelijkbare trends in de responsies, maar de absolute responswaarden van palen met een grote diameter met eenvoudige 1D staafelementen leiden tot een onderschatting van de responsie in de onderbouw. aandrijffrequentiebereik en een overschatting in het hogere aandrijffrequentiebereik.
- Er werd vastgesteld dat zelfs als maar liefst 50% van de excentrische massa's verkeerd zijn uitgelijnd, de impact van buigtrillingen op het energieverbruik van de trilblok onbeduidend is. Desalniettemin kan de buigverplaatsing aanzienlijk worden wanneer 6% van de excentrische massa's niet goed zijn uitgelijnd. Als algemene regel geldt dat palen met een kleinere diameter gevoeliger zijn voor trillingen bij lagere frequentiebereiken, terwijl palen met een grotere diameter worden beïnvloed in hogere frequentiebereiken.
- Alleen monopiles met een grote diameter zijn gevoelig voor axiale trillingen in de buurt van hun natuurlijke frequenties, terwijl alle palen met een diameter worden beïnvloed door buigtrillingen in de buurt van hun natuurlijke frequenties. Binnen het bereik van aandrijffrequenties liggen buigtrillingen dichter bij elkaar. Dit kan resulteren in een dip in de axiale trillingen terwijl een piek in de buigtrilling optreedt bij trilwerking met uitlijnfouten, wat leidt tot relatief toenemende buigverplaatsingen.
- De isolator veren worden geactiveerd in de hogere aandrijffrequenties (> 28 Hz) voor grote diamater palen. Kleine palen (< 3m) hebben geen effectieve activatie van de isolatie veren in de trilhamer voor alle aandrijf frequenties.

Contents

Nomenclature

Abbreviations

Abbreviation	Definition
DOF	Degree of freedom
GBS	Gravity based support structures
MDOF	Multi degree of freedom
OWT	Offshore wind turbine

Symbols

Latin symbols

Symbol	Definition	Unit
A	Cross-sectional area	[m^2]
a_0	Mass proportional Rayleigh damping ratio	[-]
$\mathbf{B}$	Shape function derivative matrix	[-]
b_0	Stiffness proportional Rayleigh damping ratio	[-]
$\mathbf{C}$	Element damping matrix	[kg/s]
c	Stress wave propagation velocity	[m/s]
c_{el}	Elastomer damping coefficient	[Ns/m]
$c_{s,a}$	Axial soil damping coefficient	[Ns/m^3]
$c_{s,t}$	Transverse soil damping coefficient	[Ns/m^3]
c_{el}	Elastomer damping coefficient	[Ns/m]
D	Pile diameter	[m]
$\mathbf{D}$	Elasticity matrix	[-]
E	Young's Modulus	[N/m^2]
f	Frequency	[Hz]
f_n	Natural frequency ($n = 0, 1...N$)	[Hz]
$\mathbf{F}$	Force vector	[N]
F_c	Centrifugal force	[N]
F_s	Static force	[N]
$F_v(t)$	Time dependent vertical force	[N]
$F_x(t)$	Time dependent horizontal force	[N]
$F_z(t)$	Time dependent vertical force	[N]
g	Gravity	[m/s^2]
h	Element size	[m]
h_p	Shell element pile wall thickness	[m]
I	Moment of inertia	[kgm^2]
$\mathbf{K}$	Element stiffness matrix	[N/m]
k_a	Axial soil stiffness coefficient	[N/m]
k_{el}	Elastomer pad stiffness coefficient	[N/m]
k_p	Pile stiffness coefficient	[N/m]
K_s	Soil stiffness coefficient	[N/m]
$\mathbf{K}_{s,a}$	Axial soil stiffness matrix	[N/m]
$\mathbf{K}_{s,t}$	Transverse soil stiffness matrix	[N/m]
$k_{s,a}$	Soil stiffness coefficient	[N/m]
$k_{s,t}$	Transverse soil stiffness coefficient	[N/m]

Symbol	Definition	Unit
L	Pile length	[m]
L_{em}	Embedment depth	[m]
L_{embed}	Embedment depth	[m]
$\mathbf{M}$	Element mass matrix	[kg]
M_{cl}	Mass of hydraulic clamps	[kg]
M_{dyn}	Dynamic mass	[kg]
M_{eb}	Mass of excitation block	[kg]
M_{ib}	Mass of isolator block (a.k.a suppressor housing)	[kg]
M_p	Mass of pile	[kg]
M_{supp}	Mass of suppressor housing	[kg]
M_{vib}	Total mass of vibratory hammer	[kg]
m	Mode number and circumferential modal pattern	[-]
me	Eccentric moment	[kgm]
n	Circumferential half wave number	[-]
N_{me}	Number of rotating eccentrics	[-]
N	Number of modes	[-]
N^e	Number of elements	[-]
$\mathbf{N}$	element shapefunction matrix	[-]
N_z	Axial force resultant	[N]
$\mathbf{p}$	Vector with projections	[-]
$\mathbf{q}$	nodal displacement vector	[-]
R	Radius	[m]
t	Time	[s]
$\mathbf{t}$	Vector with line loads	[-]
T	Maximum suspension force	[N]
u	Particle axial displacement at time t and location z	[m]
$\mathbf{u}^e$	Element displacement vector	[m]
$\dot{\mathbf{u}}^e$	Element velocity vector	$[m/s]$
$\ddot{\mathbf{u}}^e$	Element acceleration vector	$[m/s^2]$
v	Particle torsional rotation at time t and location θ	[rad]
w	Particle radial displacement at time t and location x	[m]
$\dot{w}$	Particle radial velocity at time t and location x	[m/s]
$\ddot{w}$	Particle radial acceleration at time t and location x	$[m/s^2]$
z	Pile longitudinal axis direction	[m]

Greek symbols

Symbol	Definition	Unit
β_z	Particle rotation at time t and location z	[rad]
$\dot{\beta}_z$	Particle rotational velocity at time t and location z	[rad/s]
$\ddot{\beta}_z$	Particle rotational acceleration at time t and location z	$[rad/s^2]$
Δ	Change in value	[-]
ζ_i	Damping ratio	[-]
η	Force transfer ratio	[-]
θ	Angle	[rad]
$\boldsymbol{\Theta}$	Matrix for solution in azimuth	[-]
λ_{min}	Minimum wavelength	[m]
μ	Hammer-pile mass ratio	[-]
ν	Poission's ratio	[-]
ξ	Material damping ratio	[-]
π	Circle circumference to circle diameter ratio	[-]
ρ	Density	$[kg/m^3]$

Symbol	Definition	Unit
$\mathbf{\Phi}$	Eigenmatrix	[-]
$\boldsymbol{\phi}$	Eigenmodes vector	[-]
ϕ	Eigenmodes	[-]
φ	Phase shift	[rad]
ω	Angular velocity	[rad/s]
ω_n	Natural frequency ($n = 0, 1...N$)	[rad]
Ω	FE Space	[-]

Math symbols

Symbol	Definition	Unit
∂	Partial derivative	[-]
ℓ	Element length	[m]

List of Figures

List of Tables

1

Introduction

The urgency of climate change has surpassed its status as a future threat, and it is now considered the most pressing problem facing humanity today [1]. The primary cause of climate change is the release of greenhouse gases resulting from the combustion of fossil fuels [2]. In response to this global crisis, 194 countries and the European Union have ratified the Paris Agreement, which aims to limit the increase in global temperature.

Since fossil fuels are a major contributor to climate change, renewable energy sources, such as offshore wind energy, have become a crucial part of the solution. The global demand for offshore wind energy is rapidly increasing, with a projected annual growth rate of 13% over the next two decades [3]. The Netherlands has committed to generating at least 70% of its electricity from renewable sources, with at least 40% coming from offshore wind turbines by 2030, as outlined in the Dutch Climate Agreement [4]. Similarly, the global goal is to increase offshore wind capacity by a factor of fifteen by 2040 [3]. Figure 1.2, which shows the European Wind Energy Association's forecast for offshore wind capacity, provides an overview of this market trend [5].
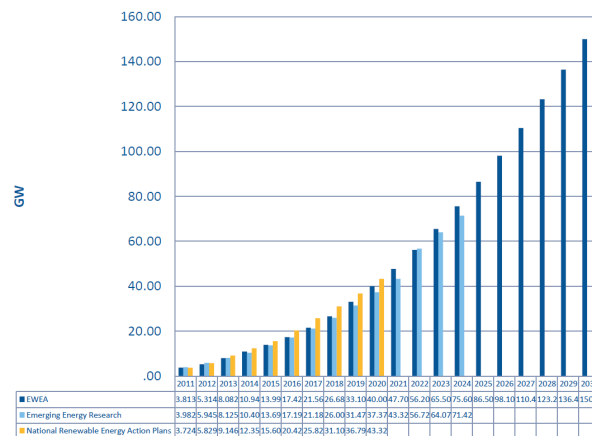
Figure 1.1: Cumulative offshore wind capacity from 2011-2030, after [5]

To meet the energy supply targets set for offshore wind, turbines must possess sufficient capacity. In Europe alone, turbine capacity has grown at an annual rate of 16% since 2014 [6]. As a result, wind turbines are increasing in both size and power, necessitating corresponding adjustments to their support structures. While various types of offshore wind turbine foundations are available, the monopile foundation is the most commonly used [7], and its size has also been growing in terms of weight and diameter. Figure 1.2 below, taken from [3], provides an overview of the increasing size of offshore wind turbines.
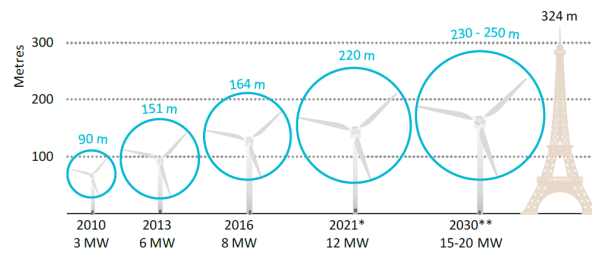
Figure 1.2: Evolution of diameter size of offshore wind turbines from 2010-2030, after [3]

The increasing size of monopiles presents new challenges that must be addressed through research into pile drivability. One such challenge is that current pile driving models, which were originally developed for small-diameter piles, are not applicable to larger-diameter monopiles [8]. The primary approach for installing monopiles into the seabed is through hydraulic impact piling, also known as hammering. An important advantage of using an impact hammer is that the number of hammer blows recorded during pile installation provides a direct indication of the pile's resistance. [9]. However, this method has significant drawbacks, including the loud noise produced during pile driving and the substantial impact forces on the monopiles caused by the hammer strikes [10].

Another technique for installing monopiles is through vibratory pile driving, which involves applying a vibration load on the pile to reduce the ground resistance and allow the pile's penetration into the soil. It has major advantages compared to the impact driving technique, such as faster installation, lower costs and nuisance to the environment, less potential damage to the pile and is applicable on both on-, near- and offshore projects[11]. As a result of these benefits, the offshore wind industry is moving towards using vibratory hammering as the preferred method for installing monopiles [12].

Despite the benefits of vibratory driving, it also has some drawbacks, with the most notable being the challenge of controlling and ensuring the reliability of the bearing capacity achieved with vibrodriven piles. Typically, for permanent installations, vibro piles are struck again with an impact hammer to assess their capacity, which decreases the economic and environmental advantages of using vibratory drivers [13].

In addition, accurately defining the vibratory driving force that acts on the pile during the driving process is becoming increasingly crucial in modern engineering models [11]. Current models assume that the mechanical action of the vibratory hammer is a force acting solely on top of the pile. However, as the size of the piles increases, so does the number of vibratory hammers on top, effectively forming a complete structure atop the pile. When the diameter of the pile becomes too large for a single vibratory hammer to reach from one end of the pile circumference to the other, large-diameter monopiles are driven into the seabed using multiple hammers, as depicted in Figure 1.3. In such cases, it is not sufficient to treat the system as a simple force acting on top of the pile, and it must be accounted for as a dynamic system atop the pile.

Figure 1.3: Offshore vibratory pile driving methods with large diameter monopiles

1.1. State of the art

The prevailing model for pile driving analysis is the one-dimensional wave equation model developed by Smith [14], which characterizes the hammer-pile-soil system as a series of discrete masses and springs. The soil resistance is represented by point resistances consisting of elasto-plastic springs, viscous dashpots, and base resistance at the pile tip. While this model has undergone improvements, particularly with regards to soil reaction during pile penetration, its applicability to larger diameter monopiles is uncertain [8]. Current approaches for assessing pile drivability are restricted to small diameter piles with diameters less than 2 meters, and are insufficient to account for dispersive effects, particularly those induced by impact hammering, that become significant with larger monopiles [8]. As such, a more accurate depiction of the pile is necessary.

Two distinct models have been introduced to consider the effects of wave dispersion in the radial direction during impact hammering. One such model is the three-dimensional axisymmetric model outlined in [8], which models the pile as a cylindrical shell using the Love-Timoshenko thin shell theory. Alternatively, [7] enhances the classical wave equation model by incorporating an extra term that accounts for the lateral movement of the pile, as described by the Rayleigh-Love rod theory. Additionally, there is a reliable representation of the impact hammer driving force in engineering models [15].

Realistic numerical techniques such as wave equation analysis or Finite Element Analysis [11] provide an accurate depiction of the vibratory hammer-pile interaction, whereas closed-form solutions still lack such representation. In engineering models, the load transfer from a vibratory hammer is approximated as a sinusoidal vertical force that operates on a one-dimensional pile. This force is derived from the counter-rotating eccentric masses in the vibrodriver. However, it appears that this assumed force significantly exceeds the forces that have been experimentally observed to be transmitted from the vibrator to the pile [11].

Research gap

One-dimensional pile models solely describe motions parallel to the pile axis and result in the axial compressive or extensional behavior of the pile. Radial expansion or compression can be derived using Poisson's ratio, independent of the pile's interaction with the hammer or soil.

Radial motions are negligible for small diameter (<2m) monopiles. However, as pile diameter increases, the effects of wave dispersion on radial motion become significant, particularly during impact hammering due to the higher frequency spectrum of excited waves in the pile [8][7]. While lateral motions during vibratory pile driving have been observed [12], the low spectrum of frequencies excited during this process is unlikely to have a considerable effect on radial motion. However, it remains unknown whether possible imperfections in terms of gear misalignments in a vibratory hammer may cause considerable radial vibrations.

To investigate the lateral displacement of large diameter monopiles during vibratory pile driving, a three-dimensional model is necessary to account for radial motions, which are not considered in current models [8]. Previous studies have developed models to address radial motions for impact hammering but not for vibratory pile driving.

Additionally, the current formula-based vibrohammer model appears to be inaccurate for estimating the loads transferred to the pile, indicating a need for a more precise description of the vibrohammer-pile interaction.

Therefore, a new study is needed to develop a three-dimensional model capable of describing the behavior of large diameter offshore wind monopiles during vibratory pile driving with a proper hammer model. The model should also incorporate a more realistic driving force to analyze the pile response and use in drivability analyses accurately.

Research relevance

The growing demand for offshore wind energy, has resulted in new challenges in the research of pile driving models for larger monopiles. Pile drivability analysis is one of the key aspects when it comes to the installation of monopile foundations. An inaccurate prediction of the pile drivability can result

in time delay or excessive costs for additional work or other project risks [8].

Accurate models have been developed to describe the drivability of impact hammering, but the same level of precision is yet to be achieved for vibratory hammering, despite the significant financial impact this installation method can have on projects. Vibratory pile driving offers installation times that are only 10% of those required for impact hammering [12], along with lower costs and less disruption to the environment, including sea mammals and other marine life[11].

However, these economic advantages of vibratory pile driving can only be achieved with accurate predictions of the drivability and capacity of the pile [12]. For that reason, a model that accurately describes the circumferential response of monopiles during vibratory pile driving is required.

1.2. Scope of research

An inaccurate description of hammer-pile interaction in engineering models for vibratory pile driving analysis is a concern. The aim of this study is to investigate the accuracy of current engineering models used in the pile drivability analysis of offshore mono pile foundations with vibratory hammers and to propose a model that is more accurate for modeling the pile response to the excitation force from the vibratory hammer for large diameter mono piles. Furthermore, the effect of an imperfection in the vibratory hammer will be studied to understand the effects of a misalignment on the pile response.

1.2.1. Questions and objectives

Objective 1
Create a vibratory hammer model and study the pile response through coupling of the hammer model with the pile model and a simplified soil reaction.

Questions:

- What is the difference between the actual vibratory hammer force from a hammer model and the force assumed in practice?
- Which frequencies activate the isolator springs inside a vibratory hammer?

Objective 2
Conduct a parametric study of the pile response to imperfections in the modeled vibratory hammer by introducing a misalignment of a single rotating eccentric mass, over a range of specified variables for multiple parameters.

Questions:

- What is the effect of a misalignment in the gears of a vibratory hammer on the pile response?
- To what extent does a misalignment lead to pile response in the frequencies that align with low radial pile modes?
- How much of the hydraulic power unit consumption is going in the radial waves due to this misalignment?

2

Literature review

In order to get theoretical background knowledge about the topic of offshore pile driveability, a literature study will be performed. First, a general understanding of offshore wind turbines (OWTs) and their various types of foundations will be gained. After, the focus will lie on the monopile type of foundation only, followed by today's pile driving techniques. Subsequently, the mechanism of the vibratory hammer will be studied thoroughly in order to model the hammer as a multi-degree-of-freedom (MDoF) system. Finally, classic drivability models will be studied together with existing hammer models in order to develop a classic drivability model and generate response data that will be compared to the response from the model that is to be developed in this thesis.

2.1. Offshore wind turbine foundations

Offshore wind turbines are complex structures composed of structural and mechanical elements. From a general point of view, the complete structure consists of four main components: the foundation, a sub/support structure, the tower and the blades, rotor and nacelle combination. The wind turbine is installed through a transition platform on top of a support structure and a foundation. See Figure 2.1 below.
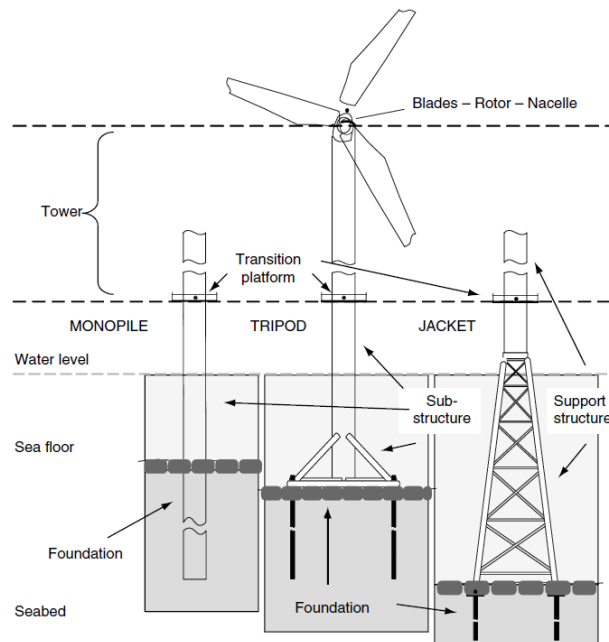
Figure 2.1: Main components of an OWT for various support structures, after [16]

One of the key aspects for economically viable offshore wind-turbines is the efficiency of the foundation solution. Depending on the water depth, maritime environmental conditions and seabed characteristics, the type of foundation structure can be determined. In Figure 2.2 below, common support structures for offshore wind-turbines are shown.
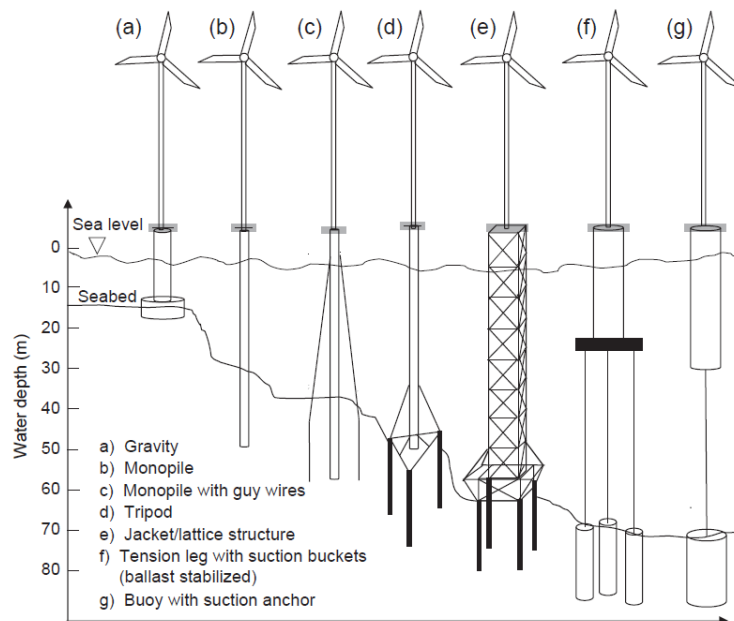
Figure 2.2: Offshore wind-turbine foundation types including ranges of water-depth, after [17]

Gravity-based support structures (GBS)
Gravity-based foundations are heavy support structures which are placed with precision on a prepared seabed to provide support for offshore wind turbines. It's typically installed in shallower water depths due to lower cost efficiency in deeper waters. Since the structure is not driven into the seabed, the stability of the GBS is completely dependent on its weight and the size of the footprint of the structure. Therefore, it is preferred to install it in calm seas with firm soils.

Monopiles
The monopile is the most widely adopted offshore wind foundation [17]. Consisting of a single (large-diameter) circular hollow steel section, the pile is typically used in shallow water depths up to 40 meter. Common diameters of monopiles vary between 4 to 6 meters, which now keep on increasing with diameters up to 11 meters, the so called XL-monopiles. Compared to other foundation types it is relatively cost-efficient, specifically in shallow depths. The drawbacks are the generated noise during installation that can harm marine life. Also, operational loads such as wind, wave and seismic loading are critical concerns and can affect the monopile in terms of early fatigue damage. The excitation frequencies of wind and wave loads are generally very close to the overall natural frequency of the structure, which makes it susceptible to resonance [18]. Therefore, considerable design efforts have to be made.

Tripods
Tripod foundations are a type of offshore wind turbine foundation that consists of three slender piles arranged in a tripod shape, supporting a transition piece that connects to the wind turbine tower. The foundation design is typically chosen for its ability to resist horizontal loads, such as those caused by wind and waves, and its relative ease of installation in deep water. Tripod foundations are often used in offshore wind farms located in deep water, where traditional monopile or jacket foundation designs may not be feasible.

Jacket foundations
Jacket foundations are another type of foundation commonly used in offshore wind turbines. They consist of a lattice structure made of steel beams and columns, resembling an oil platform. The jacket structure is installed on the seabed, and the tower of the wind turbine is mounted on top of it. The jacket foundation is designed to withstand the lateral and vertical loads induced by the wind and waves, as well as the weight of the wind turbine and the rotor. The design of jacket foundations is complex and involves considerations of soil conditions, structural integrity, and fatigue resistance. However, jacket foundations are generally considered to be a reliable and cost-effective solution for offshore wind turbines, especially for water depths greater than 30 meters.

2.2. Offshore pile driving techniques

Offshore pile driving is a critical aspect of the construction of offshore wind farms and other marine structures. It involves the installation of piles into the seabed to support the structure above. Piles can be driven into the seabed using various techniques, including impact pile driving and vibratory pile driving.

2.2.1. Impact pile driving

Impact pile driving involves using a large hammer to strike the top of the pile, driving it into the seabed. These hammers typically comprise a ram and a mechanism that enables the ram to rapidly move upwards and then drop onto the pile and the driving system. The ram should possess adequate mass and impact velocity to effectively displace the pile[9]. Impact pile driving is effective for driving piles, but it can generate high levels of underwater noise, which can be harmful to marine life [19].

2.2.2. Vibratory pile driving

Vibratory hammers are specialized equipment utilized for driving piles into or out of the ground, as opposed to impact hammers which use a heavy weight to strike the pile. Compared to impact hammers, vibratory hammers offer several advantages such as faster installation and quieter operation. Additionally, they can be used underwater, are lightweight and easy to transport. They also facilitate pile extraction and cause minimal impact on the environment, particularly in terms of marine life in offshore applications. Furthermore, vibratory hammers can be employed in close proximity to residential areas without generating noise emissions due to their relatively small size [9].

2.3. Currently used pile driveability models

As mentioned in Chapter 2, in a previous study [11] theoretical solutions for the vibratory force transferred from the vibrator to the pile during vibratory driving are shown with reference to field measurements.

In order to estimate the driveability of piles in terms of blow count (impact driving), rate of penetration (vibratory driving) stresses in the pile and the dynamic response of the soil, the dynamic behaviour of a hammer-pile-soil system has to be modelled prior to execution.

In the early 1900's, pile driving analyses were carried out by using pile driving formulas based on rigid body mechanics [20][14]. However, the piles began to show extensive damage during installation and rigid body mechanics were unable to explain these damages. Isaac was the first to point out in his work from 1931 [21] that what actually was happening in the piles is the phenomenon of one-dimensional wave propagation which was generating tension stresses in the piles due to wave reflections from the pile toe [22].

The interaction between the hammer and pile during pile driving causes energy transmission in the same direction as the exciting force, which is along the longitudinal axis of the pile. This energy is transmitted by longitudinal waves by compression and rarefaction of the pile. Longitudinal waves cause the particles of the medium (the pile in this case) to vibrate parallel to the direction of the energy transfer. See Figure 2.3 below.
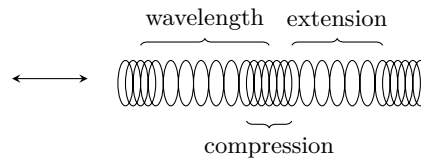
Figure 2.3: Longitudinal wave propagation

Due to this phenomenon, it is to say that pile driving is a longitudinal wave transmission problem that can be covered generally by the wave equation.

2.3.1. 1D wave equation model

In its most general form, the one dimensional wave propagation through an elastic body is given by the classical wave equation:

$$\frac{\partial^2 u(z,t)}{\partial t^2} = c^2 \frac{\partial^2 u(z,t)}{\partial z^2}, \tag{2.1}$$

in which $c = \sqrt{E/\rho}$ represents the velocity of strain wave propagation along the body's length; z is the direction of the longitudinal axis; u stands for the displacement of the cross section in the direction of z; t denotes time; E is the Young's Modulus of the material; and ρ is the mass per unit volume of the material.

The wave equation is a second order partial linear partial differential equation for the description of waves and therefore can be applied in many fields such as acoustics, fluid dynamics and electromagnetics with different physical definitions of the constant c. [23].

One of the solutions to this equation can be obtained by the separation of variables and is a sum of infinite series of sinusoidal plane waves. However, this solution is not feasible for pile driving specifically because it has boundary conditions of zero displacement, while the purpose of the wave equation analysis is to analyse the motion of the pile, which is prevented by these boundary conditions.

Another way to solve the differential equation is to make use of the D'Alembert's solution [24]. This method is one of the most commonly used methods [25] with a major characteristic which does not allow for a distortion in the pulse propagation [24]. At first sight this does not appear to be a problem for the general wave equation. However, the wave equation as stated above does not consider any form of shaft resistance from the surrounding soil. This is an important factor to take into account considering the application of the wave equation on piles [25]. Therefore, in order to apply the wave equation on pile driving a significant modification has to be done on the equation.

In Figure 2.4 below, a sketch of the pile driving process and the drivability model is given.
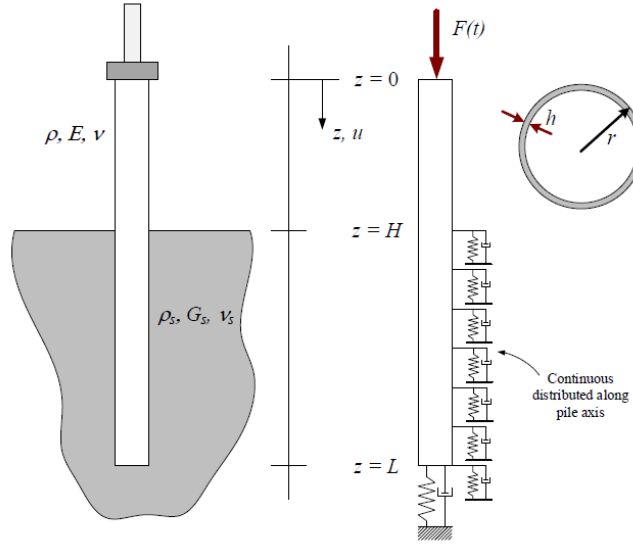
Figure 2.4: Pile driving process (left) and driveability model (right), after [26]

As to be seen from this Figure, the part of the pile embedded in the soil undergoes shaft resistance. Applying force equilibrium on the free body diagram of the one dimensional bar including the friction from the soil, results in the following equation [22]:

$$\rho A \frac{\partial^2 u}{\partial t^2} - EA \frac{\partial^2 u}{\partial z^2} + R_s = 0, \tag{2.2}$$

in which the constants are left as is for the sake of simplicity. Additional constants in eq. (2.2) are as follows; A represents the cross-sectional area of the body; R_s stands for the non-linear soil resistance, which is equal to $K_s u + C_s \frac{\partial u}{\partial t}$, with K_s being the soil stiffness coefficient and C_s being the soil damping coefficient.

Since the early 1900's it has been practically impossible to solve the mathematics on pile driving action in a practical manner [14]. Using the wave equation only has shown many errors, partly because of neglecting the shaft resistance [27]. But even with eq. 2.2 where the soil resistance is implemented in the equation of motion, there are still limitations for the use of pile driving analysis.

First, it assumes a uniform cross-section for the pile without discontinuities, which is not always necessarily true for pile driving [22]. Second, the equation assumes no variation in the soil along the shaft. Consideration of soil variability along the shaft can only be achieved through a numerical approach [28]. Furthermore, it does not count for plastic deformation after passing the yield limit of the soil [29][22], which is essential to the penetration of the pile [25]. Specifically because the goal of pile driving lies in stressing the soil beyond its elastic limit to be able to achieve a permanent set with each blow or any type of excitation [22].

Many attempts have been made to solve the pile driveability problem, like the earlier mentioned separation of variables method, the D'Alembert's solution and Isaac's work. Other solutions like the Fourier type solution from [30] ,method of images used in [31] or solutions for the (semi-)infinite pile method [32], also seem to be not applicable for the prediction of pile behaviour in its *totality* [25].

It is to be noted that pile driving involves many complications and as a result of these difficulties, all pile driving formulae are partly empirical and therefore the applicability is limited up to some certain parameters that were used during the empirical studies [14]. Equation 2.2 which includes shaft resistance from the soil however, is closest to reality in case of pile driving [22].

Smith's method

The problems mentioned above were eventually solved by the work proposed by Smith in 1960 [22]. It is the most convenient and most widely used numerical approach based on a finite difference scheme [28]. This solution simulates the 1D wave propagation in the pile by discretizing the pile into a series of lumped masses interconnected through pile springs. The soil resistance is idealized as an visco-elastic-plastic reaction on each lumped mass along the shaft, as well as below the pile tip [14][22]. Depending on the type of hammer, the components of the hammer are also modelled as either a lumped mass or a spring. See Figure 2.5 below.
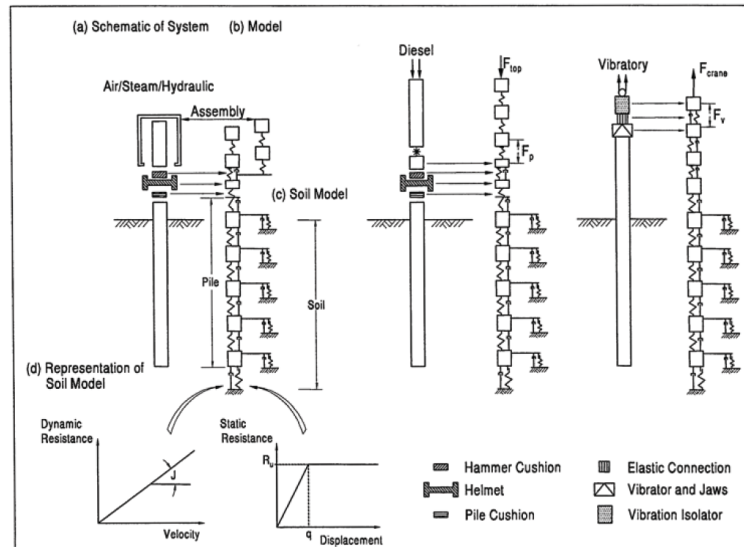
Figure 2.5: Smith's finite difference model with various types of pile driving equipment, after [22]

The pile being discretized into smaller segments enables the possibility to vary the soil properties along the shaft. The soil property is only constant along the length of the segment, instead of being constant along the total length of the pile.

However, the model does have some limitations [33] and over the years there have been some improvements made to the model [22]

2.4. Vibratory hammer mechanism

The vibratory pile driving technique consist of applying a longitudinal vibratory motion of a certain frequency and amplitude onto the monopile. By reducing the ground resistance, vibratory loading allows penetration of the monopile into the soil under its own weight. The characteristics of the hammer suppose to allow only vertical vibrations to be transmitted into the pile, which will be studied in detail in this section.

2.4.1. Basic components of a vibratory hammer

The vibratory hammer can be divided into three main components: (1) a suppressor housing, (2) vibration case (also called exciter block) and (3) one or more clamping devices depending on the type and size of the pile, see Figure 2.6 below.
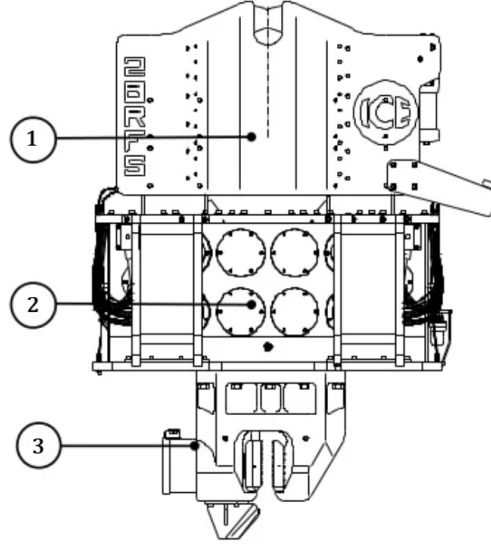
Figure 2.6: Components of a vibratory driver, after [34]

The mechanical action of the vibratory hammer can be divided into two parts: the vibratory action and a stationary action.

Vibratory action
The vibratory action is generated in the vibration case and is powered by a hydraulic power unit. The vibration case consist of multiple pairs of eccentric masses that rotate in opposite direction, causing only a vertical motion of the hammer.

In Figure 2.7 below, a complete cycle of 1 pair of two counter rotating masses is shown. As to be seen from this figure, the work line of the centrifugal forces caused by the counter-rotating masses are intersecting in every direction except the upward and downward directions. The forces with intersecting work lines are therefore cancelled out in these directions, causing only an upward and downward motion of the hammer.
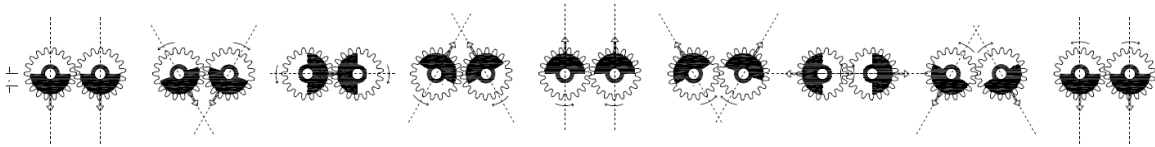
Figure 2.7: Counter-rotating eccentric masses in the vibration case

Counter-rotating eccentric masses generate a centrifugal force from which the magnitude depends on the eccentric moment and frequency of the rotating masses. The actions of an even number of counter-rotating eccentric masses combine into sinusoidal force $F_v(t)$:

$$F_v(t) = me\omega^2 sin(\omega t) = F_c sin(\omega t), \tag{2.3}$$

where
F_c = maximum centrifugal force [N]
me = eccentric moment [kg·m]
ω = angular frequency [rad/s]

An alternative quantification of the angular frequency can be the rotation speed R [rpm] and frequency f [Hz], with:

$$R = 60 \cdot f = 60 \cdot \frac{\omega}{2\pi}, \tag{2.4}$$

see Figure 2.8 below.
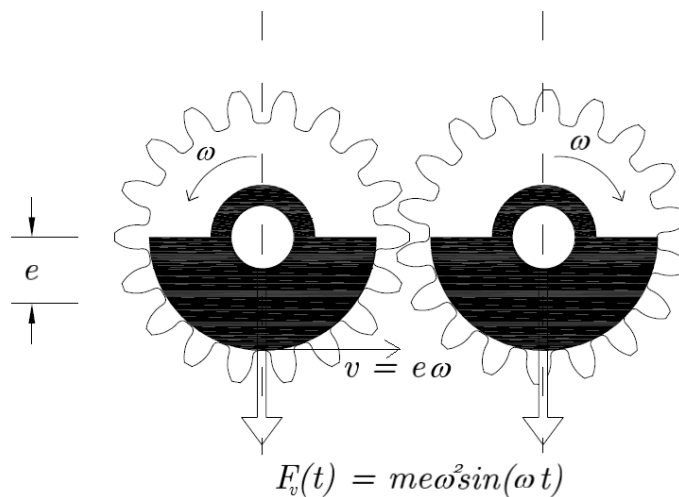
Figure 2.8: Centrifugal force generated by counter-rotating eccentric masses

Depending on the capacity of the hammer, the vibration case can consist of multiple pairs of counter-rotating eccentric masses. Vibrations that are generated by the vibration case are transmitted to the pile through the clamp(s), component (3) in Figure 2.6, which is rigidly connected to the pile [35]. If there is a second clamp, which applies for tubular cross-section piles, the clamps are adjustable according to the diameter of the monopile.

Stationary action
The vibration case is connected to the suppressor housing (component (1)) through a number of elastomer pads and is directly suspended through a suspension hook to a carrier. The suppressor housing functions as a filter for vibrations towards the carrying crane by its mass, as well as through the elastomer pads and simultaneously contributes to the vertical force exerted on the monopile that is being driven. This suppressor housing can therefore be counted as a quasi-stationary mass [11] [36]. The elastomere pads in between the suppressor housing and excitation block are designed such that the vibrations going upwards towards the crane are isolated [11].

Complete mechanical action
The complete mechanical action of the vibrator can be viewed as at least a two degree of freedom (DOF) system consisting of the mass of the exciter block (vibration case) M_{eb} and the mass of the suppressor housing (functioning as an isolator block) M_{ib} and the mass of the clamping devices M_{cl}. Furthermore, it should be noted that the mass M_{eb} is subjected to gravity g and the sinusoidal force given in eq. (2.3) and the mass M_{ib} is subjected to gravity and the suspension force T, see Figure 2.9 below.
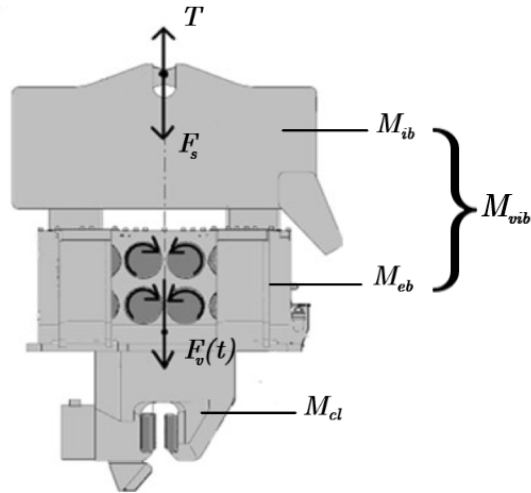
Figure 2.9: Representation of the vibratory load $F_v(t)$, the quasi-static load F_s and the suspension force T, after [11]

Herewith, the vibratory mass becomes $M_{vib} = M_{eb} + M_{ib}$ and the net quasi-static force on the pile is given by [36]:

$$F_s = (M_{vib} + M_{cl}) \cdot g - T \tag{2.5}$$

In current engineering models, the mechanical action acting on top of the pile is assumed to be the sum of the vibratory action and the stationary action [36].

3

Methods

In this chapter, the methodology used to model the hammer-pile-soil system will be described. The classical wave equation (2.1),which is a partial differential equation (PDE), must be transformed into a system of ordinary differential equations (ODE's) in order to analyze the dynamic behavior of the pile in the Python computer language. This will be done using the technique of the Finite Element Method (FEM). A general overview of the finite element model and its assumptions will be provided.

To simulate the vibrations of the pile, three different models will be modelled in Python. The first model will represent the pile with 1-dimensional linear bar elements to capture axial vibrations. The second model will incorporate beam elements to include bending vibrations. These two models, which will use very slender pile dimensions, will be used as verification models. The main model will be created using thin circular cylindrical shell elements to represent the pile.

To validate the accuracy of the shell model, its results will be compared to those obtained using simple 1D bar and beam elements for a case with very slender dimensions. This allows for confirmation that the shell model is set up correctly for studying the behavior of offshore monopiles with larger diameters. The validation of the bar and beam elements will be done by comparing them to the analytical solution for a simple free-free case.

Also, the soil model used in this study, which consists of springs attached to the nodes at specific depth levels, will be described. Finally, an overview of the 225 combinations of the parameters that are studied in this work will be provided.

The vibratory action from the shaker will be applied as a force on top of the pile, like current engineering models, as well as a 2 DOF system.

3.1. Description of the finite element model

In order to examine the structural response of the monopile using a model that assumes a continuously distributed mass throughout the length of the element, the elastic continuum, in this case the pile, will be discretized within the FEM framework.

The deformation of each element is expressed through shape functions depending on the element type and the nodal displacements of a single element:

$$\mathbf{u}^e(z,t) = \mathbf{N}(z)\mathbf{q}(t) \tag{3.1}$$

in which,

- $\mathbf{u}^e(z,t)$ is the element deformation
- $\mathbf{N}(z)$ is the element shape function
- $\mathbf{q}(t)$ is the nodal displacement

The following equation of motion, which is time-dependent only, generally describes the dynamic behavior of the continuum for all element types obtained from the discretization of the FEM [37]:

$$\mathbf{M}\ddot{\mathbf{u}}(t) + \mathbf{C}\dot{\mathbf{u}}(t) + \mathbf{K}\mathbf{u}(t) = \mathbf{F}(t) \tag{3.2}$$

in which,

- $\mathbf{M}$ stands for the global mass matrix
- $\mathbf{C}$ as the global damping matrix
- $\mathbf{K}$ as the global stiffness matrix
- $\mathbf{u}$ as the displacement vector and $\dot{\mathbf{u}}$ and $\ddot{\mathbf{u}}$ being the first and second time derivative describing the velocity and acceleration of the displacement respectively.

The distribution of the masses in the elements is considered continuous. The assumption about the distribution of the masses largely defines the structure of the mass matrices. The notion of virtual work will be used to calculate equivalent forces operating in nodal points for an element with continuously distributed mass. In general, the mass matrix is constructed by using the principle of kinetic energy from which the mass matrix can be obtained:

$$\mathbf{M} = \int_{\Omega} \rho \mathbf{N}^{\mathrm{T}} \mathbf{N} d\Omega \tag{3.3}$$

By using the principle of strain energy, the stiffness matrix can be obtained:

$$\mathbf{K} = \int_{\Omega} \mathbf{B}^{\mathrm{T}} \mathbf{D} \mathbf{B} d\Omega \tag{3.4}$$

in which

- $\mathbf{N}$ is the row matrix of the corresponding shape functions
- $\mathbf{B}$ is the derivative of the relevant shape functions
- $\mathbf{D}$ is the elasticity matrix, which is in the regarded one-dimensional case only represented through the modulus of elasticity E.

The mass and stiffness matrices for the various element types that are implemented in the Python program will be detailed in the chapters that follow.

3.1.1. Eigenvalue problem
In the dynamic response analysis, the generalized eigenvalue problem

$$(\mathbf{K} - \omega^2 \mathbf{M})\mathbf{\Phi} = 0 \tag{3.5}$$

is considered in order to obtain the natural frequencies ω_n and mode shapes $\mathbf{\Phi}_i$ of the vibratory hammer-pile-soil system. In eq 3.5, the stiffness matrix $\mathbf{K}$ is including the soil stiffness, which will be elaborated in the chapters below.

3.1.2. Damping
The damping matrix $\mathbf{C}$ from equation 3.2 will be expressed proportional to the mass and stiffness matrices. This is the so called *Rayleigh* damping and is the most widely form of damping that is used in the FE method [38]:

$$\mathbf{C} = a_0 \mathbf{M} + b_0 \mathbf{K} \tag{3.6}$$

in which a_0 and b_0 are constants which are obtained by estimating the first two modal damping ratios ζ_i, for $i = 0, 1$. By estimating the modal damping ratios of the first two modes of the system, the coefficients a_0 and b_0 can be determined by the following [38]

$$a_0 = \frac{2\omega_0\omega_1(\zeta_0\omega_1 - \zeta_1\omega_0)}{\omega_2^2 - \omega_0^2}$$

$$b_0 = \frac{2(\zeta_1\omega_1 - \zeta_0\omega_0)}{\omega_1^2 - \omega_0^2}$$

(3.7)

Furthermore, the Rayleigh damping is also the most feasible type of damping for this particular problem since it refers to material damping that is evenly dispersed throughout the pile material rather than focused at a single location.

3.1.3. Integration method

In this study, the LSODA method was chosen for time integration in the numerical model of the vibratory hammer-pile-soil system. This decision is based on the fact that the response of the system is governed by low frequency modes and implicit time integration methods, such as LSODA, are well-suited for problems with low frequency responses [39].

3.1.4. Discretization

In order to approximate the solution to the system of differential equations from equation 3.2 as a set of discrete numerical values, the elastic continuum is divided into discrete elements. In addition to spatial discretization, a suitable temporal discretization is performed, dividing the simulation time into discrete time steps that are small enough to accurately capture the behavior of the system.

Spatial discretization

One of the key components to obtaining accurate results is the size of the element. Accuracy in wave propagation simulations requires a ratio between the element size h and the minimum wavelength λ_{min} that is intended to capture to be approximately $\frac{1}{10}$ [40]. The minimum wavelength depends on the maximum frequency of interest $f_{int,max}$.

As discussed in chapter 2, the vibratory action from the shaker is a low frequency action and will be in the range of 20 - 50 Hz. This means that high frequency responses are not of interest. As a result, the maximum frequency of interest is set at 200 Hz. The wavelength of a propagating wave in a medium can then be calculated by the wavespeed c, described for longitudinal waves by

$$c = \sqrt{\frac{E}{\rho}}$$

(3.8)

and for transverse waves

$$c = \sqrt{\frac{EI}{\rho A}}$$

(3.9)

The minimum wavelength can then be calculated by

$$\lambda_{min} = \frac{c}{f_{int,max}}$$

(3.10)

As a result, the maximum element size can be obtained by

$$h \leq \frac{\lambda_{min}}{10} = \frac{c}{10 f_{int,max}}$$

(3.11)

To improve accuracy, more elements per wavelength will be used. It will not impose a significant change in the computation time since it is a linear system. Independent of the pile dimensions, the number of elements will be chosen such that the element length is around around $\frac{3}{5}$. This is much less than the maximum element size h given in eq. 3.11.

Temporal discretization

The use of an implicit time integration approach, which is unconditionally stable, eliminates the requirement for a maximum time step ensuring numerical stability. However, to prevent a wave front from reaching two consecutive nodes at the same time, an accuracy criterion for unconditionally stable time integration will be applied. This condition is given by [39][40]

$$\Delta t \leq \frac{h}{c} \tag{3.12}$$

Boundary- and initial conditions

For all models, it is assumed that both the initial displacement and velocity are zero. In terms of restriction, the boundary conditions for all cases will be Free-Free. Depending on the specific model, either a force will be applied to the top boundary or an external force will be present in a mass-spring system. A detailed discussion of these boundary conditions will follow in the subsequent sections.

3.2. Bar and beam elements pile model

In this section, a more detailed description of the mass and stiffness matrices used in the bar and beam models will be provided. Before diving into the specifics, it is worth briefly reviewing the role of bar and beam elements in this study. As described in the previous section, these elements are used as verification models for the main shell element model. Specifically, very slender bar and beam elements are used to represent the pile, and compare their results to those obtained using the shell model for axial and bending vibrations, respectively. By doing this, it can be confirmed that the shell model is set up correctly for studying the behavior of offshore monopiles with larger diameters.

3.2.1. 1D bar elements

The 1D bar elements are used to model the axial vibrations of the pile. In this subsection, the mass and stiffness matrices for the 1D bar elements are described and how they are incorporated into the overall finite element model. In Figure (3.1) below, the bar is illustrated as a single element with the degrees of freedom on the nodes for a linear approach.
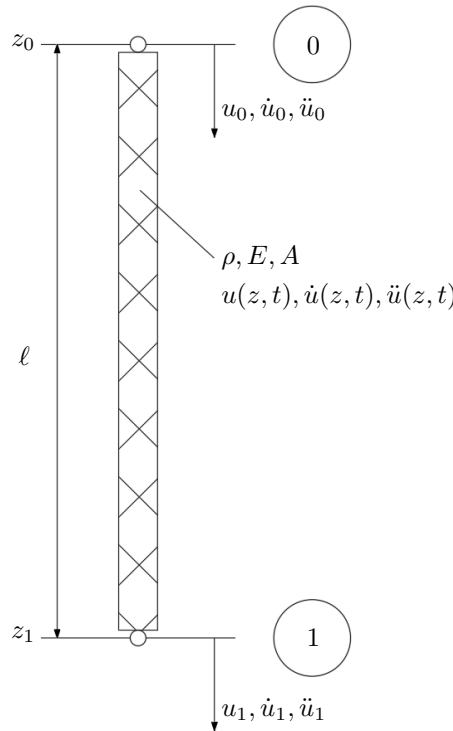
Figure 3.1: Bar element with continuously distributed mass

According to the coordinate system from Figure 3.1 above, the linear shape function matrix $\mathbf{N}$ and its corresponding derivative matrix $\mathbf{B}$ for 1D bar elements is defined as follows:

$$\mathbf{N} = \begin{bmatrix} N_1^l(z) & N_2^l(z) \end{bmatrix} \tag{3.13}$$

$$\mathbf{B} = \begin{bmatrix} N_1^{l\prime}(z) & N_2^{l\prime}(z) \end{bmatrix} \tag{3.14}$$

in which the superscript l stand for *linear* and

$$N_1^l(z) = \frac{1-z}{\ell} \tag{3.15}$$

$$N_2^l(z) = \frac{z}{\ell} \tag{3.16}$$

Mass and stiffness matrices
The model will be analysed with continuously distributed masses along the bar element with constant cross-section. By implementing the linear shape functions from eq. 3.15 and 3.16 in to eq. 3.3 and 3.4, the following mass and stiffness element matrices are obtained[37]:

$$\boldsymbol{M}^e = \int_0^\ell \rho A \begin{bmatrix} \dfrac{1-z}{\ell} \\ \dfrac{z}{\ell} \end{bmatrix} \begin{bmatrix} \dfrac{1-z}{\ell} & \dfrac{z}{\ell} \end{bmatrix} dz = \frac{\rho A \ell}{6} \begin{bmatrix} 2 & 1 \\ 1 & 2 \end{bmatrix} \tag{3.17}$$

$$\boldsymbol{K}^e = \int_0^\ell EA \begin{bmatrix} \dfrac{-1}{\ell} \\ \dfrac{1}{\ell} \end{bmatrix} \begin{bmatrix} \dfrac{-1}{\ell} & \dfrac{1}{\ell} \end{bmatrix} dz = \frac{EA}{\ell} \begin{bmatrix} 1 & -1 \\ -1 & 1 \end{bmatrix} \tag{3.18}$$

The complete EOM in Python for N degrees of freedom is written as the sum of all the element matrices in one global system matrix as follows:

$$\frac{\rho A \ell}{6} \begin{bmatrix} 2 & 1 & & & & \\ 1 & 4 & 1 & & & \\ & 1 & 4 & 1 & & \\ & & \ddots & \ddots & \ddots & \\ & & & 1 & 4 & 1 \\ & & & & 1 & 2 \end{bmatrix} \begin{bmatrix} \ddot{u}_0 \\ \ddot{u}_1 \\ \ddot{u}_2 \\ \vdots \\ \ddot{u}_N \end{bmatrix} + \frac{EA}{\ell} \begin{bmatrix} 1 & -1 & & & & \\ -1 & 2 & -1 & & & \\ & -1 & 2 & -1 & & \\ & & \ddots & \ddots & \ddots & \\ & & & -1 & 2 & -1 \\ & & & & -1 & 1 \end{bmatrix} \begin{bmatrix} u_0 \\ u_1 \\ u_2 \\ \vdots \\ u_N \end{bmatrix} \tag{3.19}$$

Force vector
The bar elements will be subjected to axial forces from the vibratory hammer which will be implemented in the force vector $\mathbf{F}_{bar}$ of length N. This force acts on the first node of the pile and will therefore be implemented on the first pile node as follows:

$$\mathbf{F}_{bar} = \begin{bmatrix} F_z(t) \\ 0 \\ 0 \\ \vdots \\ 0 \end{bmatrix} \tag{3.20}$$

The complete description of the vertical force $F_z(t)$ will be given in section 3.4.

3.2.2. 1D beam elements
The beam elements will be used to capture the bending vibrations of the pile and solve for the transverse disaplcement w and rotation β_z. In the same way as the rod elements, the stiffness and mass matrices for the beam elements are derived using the assumptions of small deformations and constant cross-sectional

properties. Figure (3.2) below, the beam element is illustrated as a single element with the degrees of freedom on the nodes for a linear approach.
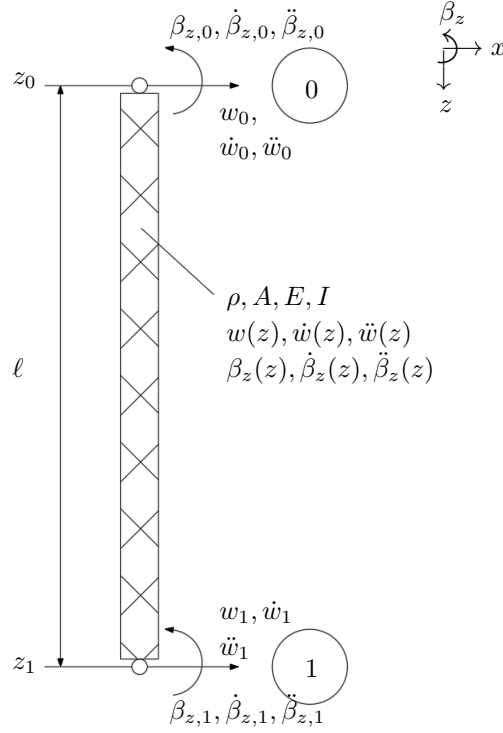
Figure 3.2: Beam element with continously distributed mass

According to the coordinate system from Figure 3.2 above, the shape function matrix $\mathbf{N}$ and its corresponding derivative matrix $\mathbf{B}$ for 1D beam elements are defined as follows:

$$\mathbf{N} = \begin{bmatrix} N_1^c(z) & N_2^c(z) & N_3^c(z) & N_4^c(z) \end{bmatrix} \tag{3.21}$$

$$\mathbf{B} = \begin{bmatrix} N_1^{c\prime}(z) & N_2^{c\prime}(z) & N_3^{c\prime}(z) & N_4^{c\prime}(z) \end{bmatrix} \tag{3.22}$$

in which the superscript c stand for *cubic* and

$$N_1^c(z) = 1 - 3(\tfrac{z}{\ell})^2 + 2(\tfrac{z}{\ell})^3 \tag{3.23}$$

$$N_2^c(z) = z - 2\frac{z^2}{\ell} + \frac{z^3}{\ell^2} \tag{3.24}$$

$$N_3^c(z) = 3(\tfrac{z}{\ell})^2 - 2(\tfrac{z}{\ell})^3 \tag{3.25}$$

$$N_4^c(z) = -\frac{z^2}{\ell} + \frac{z^3}{\ell^2} \tag{3.26}$$

Mass and stiffness matrices

By implementing the shape functions in the same way as the bar elements, the following mass and stiffness matrices are obtained:

$$\boldsymbol{M}^e = \frac{\rho A \ell}{420} \begin{bmatrix} 156 & 22\ell & 54 & -13\ell \\ 22\ell & 4\ell^2 & 13\ell & -3\ell^2 \\ 54 & 13\ell & 156 & -22\ell \\ -13\ell & -3\ell^2 & -22\ell & 4\ell^2 \end{bmatrix} \tag{3.27}$$

$$\boldsymbol{K}^e = \frac{EI}{\ell^3} \begin{bmatrix} 12 & 6\ell & -12 & 6\ell \\ 6\ell & 4\ell^2 & -6\ell & 2\ell^2 \\ -12 & -6\ell & 12 & -6\ell \\ 6\ell & 2\ell^2 & -6\ell & 4\ell^2 \end{bmatrix} \tag{3.28}$$

The complete EOM in Python for N degrees of freedom will be written as the sum of all the element matrices in one global system matrix in the same way as the bar elements:

$$\begin{bmatrix} \boldsymbol{M}^e & & \\ & \ddots & \\ & & \boldsymbol{M}^e \end{bmatrix} \begin{bmatrix} \ddot{\boldsymbol{u}}_0^e \\ \vdots \\ \ddot{\boldsymbol{u}}_{N^e}^e \end{bmatrix} + \begin{bmatrix} \boldsymbol{K}^e & & \\ & \ddots & \\ & & \boldsymbol{K}^e \end{bmatrix} \begin{bmatrix} \boldsymbol{u}_0^e \\ \vdots \\ \boldsymbol{u}_{N^e}^e \end{bmatrix} \tag{3.29}$$

in which the superscript e stands for *element* and

$$\ddot{\boldsymbol{u}}_j^e = \begin{bmatrix} \ddot{w}_j \\ \ddot{\beta}_{z,j} \\ \ddot{w}_{j+1} \\ \ddot{\beta}_{z,j+1} \end{bmatrix} \quad \text{and} \quad \boldsymbol{u}_j^e = \begin{bmatrix} w_j \\ \beta_{z,j} \\ w_{j+1} \\ \beta_{z,j+1} \end{bmatrix} \tag{3.30}$$

for $j = 0, 1..N^e$ and N^e stands for number of elements. The total number of modes N for beam elements with Free-Free boundary conditions, is equal to $2N^e + 2$.

Force vector
The misalignment in the gears of the vibratory hammer will introduce a phase shift φ, resulting in the application of horizontal forces on the pile. These forces will act on the first degree of freedom of the beam model and will be included in the force vector $\mathbf{F}_{beam}$ of length N below. The potential moment caused by this misalignment will not be considered in the model.

$$\mathbf{F}_{beam} = \begin{bmatrix} F_x(t) \\ 0 \\ 0 \\ \vdots \\ 0 \end{bmatrix} \tag{3.31}$$

Since a moment acting on the pile is disregarded in this study, the first rotational degree of freedom $\beta_{z,0}$ in the force vector will remain zero. The complete description of the horizontal force $F_x(t)$ will be given in section 3.4.

3.3. Thin circular cylindrical shell elements

Thin circular cylindrical shell elements are a type of finite element used to represent thin-walled structures such as pipes and tubes and are considered thin-walled when the diameter over thickness ratio is greater than 20 [41]. These elements are particularly useful for analyzing the behavior of structures subjected to bending, torsion, and axial loads. In this study, thin circular cylindrical shell elements are used to model the pile in order to capture the dynamic behavior of the hammer-pile-soil system. The use of shell elements allows for a more realistic representation of the pile, as they can capture both bending and axial vibrations, and account for the effect of the pile's diameter on its behavior.

Sign convention
The cylindrical shell can be modelled as a collection of rings of constant cross sections, with their center lying on the z-axis. The coordinate system of the thin circular cylindrical shell elements used in this study is shown in Figure 3.3 below , with the z-axis in the axial direction, the θ-axis in the circumferential direction, and the x-axis in the radial direction. The shell is defined by its height ℓ, radius R, constant thickness h, density ρ, modulus of elasticity E, and Poisson's ratio ν. The displacements of the shell are represented by u, v, and w in the z, θ, and x directions, respectively.
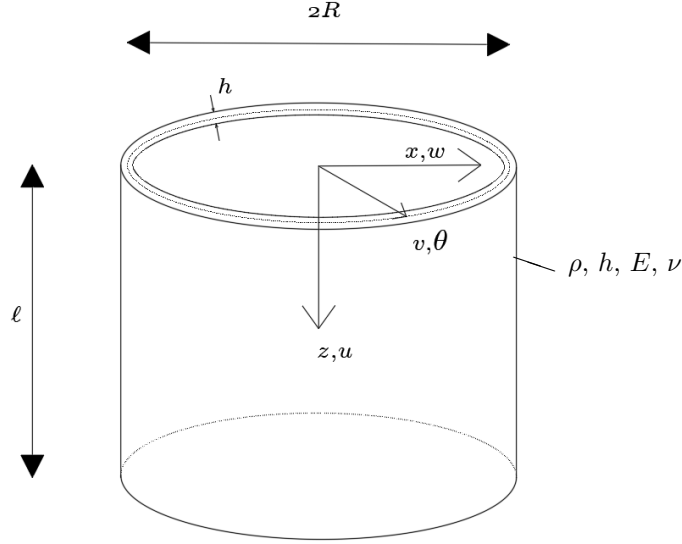
Figure 3.3: Coordinate system of the shell element

The circular cylindrical shell vibrates in both axial and circumferential modes, as shown in Figure 3.4 below. Any combination of these modes defines the modal frequencies of the shell.
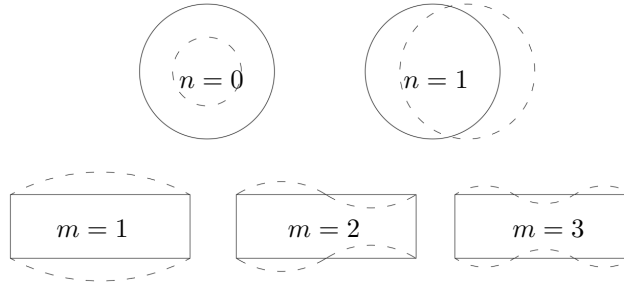
Figure 3.4: Axial nodal patterns m and circumferential nodal patterns n

This study covers the cases $n = 0$ and $n = 1$ only. Higher circumferential nodal patterns are out of the scope of this study. In subsequent sections of the report, the term "axial" refers exclusively to the axial response in the axisymmetric case corresponding to the $n = 0$ mode. This means that when axial vibrations are mentioned, it is specifically referring to the $n = 0$ case. Similarly, the term "bending" or "bending-like motion" is used to describe the lateral pile motion resembling bending that corresponds to the $n = 1$ mode only, and radial vibrations are also associated with the $n = 1$ mode.

3.3.1. Semi-analytical finite element model

The Semi-Analytical Finite Element (SAFE) method proposed in [42] will be utilized to model the thin circular cylindrical shell elements. In accordance with the Love-Timoshenko shell theory and the consideration of n harmonics, the displacement field for each element can be expressed as stated in [42] as follows:

$$\tilde{\mathbf{u}} = \begin{bmatrix} u & v & w & \beta_z \end{bmatrix}^T = \mathbf{\Theta}_n \mathbf{N} \mathbf{u}_n, \quad \mathbf{u}_n = \begin{bmatrix} u_n^i & v_n^i & w_n^i & \beta_{z,n}^i & u_n^{i+1} & v_n^{i+1} & w_n^{i+1} & \beta_{z,n}^{i+1} \end{bmatrix} \quad (3.32)$$

in which $\beta_z = \dfrac{\partial w}{\partial z}$ and the $\mathbf{\Theta}_n$-matrix is defined as:

$$\mathbf{\Theta}_n = \begin{bmatrix} \cos(n\theta) & 0 & 0 & 0 \\ 0 & \text{-}\sin(n\theta) & 0 & 0 \\ 0 & 0 & \cos(n\theta) & 0 \\ 0 & 0 & 0 & \cos(n\theta) \end{bmatrix} \quad (3.33)$$

The shapefunction matrix $\mathbf{N}$ contains the same linear and cubic shapefunctions as defined for the bar and beam elements. For the approximation of u an v, linear shape functions from eq. 3.15 and 3.16 will be used and for the approximation of w and β_z, cubic shape functions from eq. 3.23 to 3.26 will be used:

$$\mathbf{N} = \begin{bmatrix} N_1^l(z) & 0 & 0 & 0 & N_2^l(z) & 0 & 0 & 0 \\ 0 & N_1^l(z) & 0 & 0 & 0 & N_2^l(z) & 0 & 0 \\ 0 & 0 & N_1^c(z) & N_2^c(z) & 0 & 0 & N_3^c(z) & N_4^c(z) \\ 0 & 0 & \dfrac{\mathrm{d}N_1^c(z)}{\mathrm{d}z} & \dfrac{\mathrm{d}N_2^c(z)}{\mathbf{d}z} & 0 & 0 & \dfrac{\mathrm{d}N_3^c(z)}{\mathrm{d}z} & \dfrac{\mathrm{d}N_4^c(z)}{\mathrm{d}z} \end{bmatrix} \tag{3.34}$$

3.3.2. Mass and stiffness matrices

In this chapter the mass and stiffness matrices obtained from [42] will be given for thin circular cylindrical shell elements for the cases $n = 0$ and $n > 0$. Only the symmetric cases will be used.

Case n = 0
In the case of symmetry where $n = 0$, the analysis takes into account only three degrees of freedom. Consequently, the element matrix has dimensions of 6×6. The displacement vector for a single element, specifically for $i = 0$ and $i = 1$, includes axial, radial, and rotational displacements denoted by u, w, and β_z, respectively, and can be defined as follows:

$$\mathbf{u}_0 = \begin{bmatrix} u_0^0 & w_0^0 & \beta_{z,0}^0 & u_0^1 & w_0^1 & \beta_{z,0}^1 \end{bmatrix} \tag{3.35}$$

The mass and stiffness matrices $\mathbf{M}_0$ and $\mathbf{K}_0$ are given in Annex A, eq. A.1 and A.2 respectively.

Case n = 1
In the case where $n = 1$, all four degrees of freedom are taken into account. As a result, the size of the element matrix is 8×8. The displacement vector for a single element, particularly for $i = 0$ and $i = 1$, comprises axial, tangential, radial, and rotational displacements denoted by u, v, w, and β_z, respectively, and can be defined as follows:

$$\mathbf{u}_n = \begin{bmatrix} u_n^0 & v_n^0 & w_n^0 & \beta_{z,n}^0 & u_n^1 & v_n^1 & w_n^1 & \beta_{z,n}^1 \end{bmatrix} \tag{3.36}$$

The mass and stiffness matrices $\mathbf{M}_n$ and $\mathbf{K}_n$ are given in Annex A, eq. A.3 and A.4 respectively.

3.3.3. Force vector

The force vector will vary depending on the value of the wavenumber n, so each case must be analyzed separately.

Case n = 0
In this case, only axial forces from the vibratory hammer are considered. These will act on the first element. Assuming the force $F_z(t)$ from the vibro-hammer is a pointload and is distributed uniform along the circumference, the force vector $\mathbf{F}_0$ is defined as in [42]:

$$\mathbf{F}_0 = \mathbf{p}_{n=0} = \int_0^{2\pi} \left[\mathbf{\Theta}_n^\mathrm{T} \mathbf{t}^{(i)} \right] R \mathrm{d}\theta \tag{3.37}$$

in which

$$\mathbf{t}^i = \begin{bmatrix} p_z \\ p_r \\ m_{zz} \end{bmatrix} = \begin{bmatrix} \dfrac{F_z(t)}{2\pi R} \\ 0 \\ 0 \end{bmatrix} \tag{3.38}$$

in which the vector $\mathbf{t}^i$ contains linethoads and $\mathbf{p}_n$ contains the projected forces. Carrying out the integral from eq. 3.37, with the $\mathbf{\Theta}_n$-matrix from eq. 3.33 results in:

$$\mathbf{p}_n = \begin{bmatrix} F_z(t) & 0 & 0 \end{bmatrix}^T \tag{3.39}$$

This is in accordance with the mass and stiffness matrices obtained by [42]. When comparing this force to the force from the bar elements, the first element $F_{bar}^{i=0}$ in the vector $\mathbf{F}_{bar}$ from equation 3.20 will be:

$$F_{bar}^{i=0} = \int_0^{2\pi} p_z R_p d\theta = F_z(t) \tag{3.40}$$

Case n = 1

The transverse force applied on the shell will have a radial component p_r and tangential component p_θ along the circumference. See Figure 3.5 below
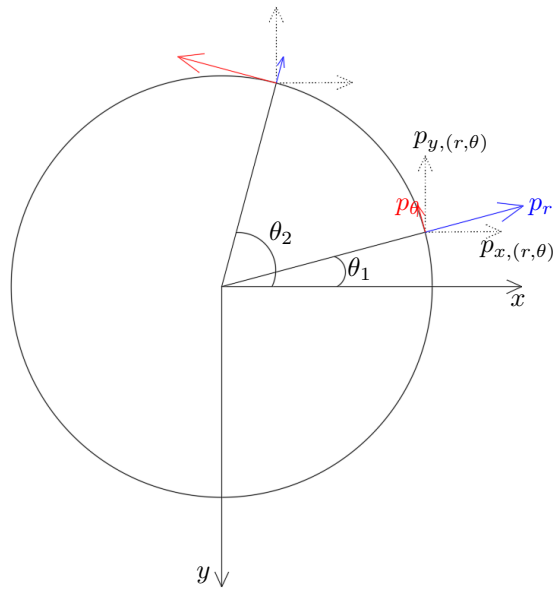
(a) Example of the distribution of the polar coordinates of the transverse force $F_x(t)$ along the circumference for two arbitrary $\theta's$ θ_1 and θ_2
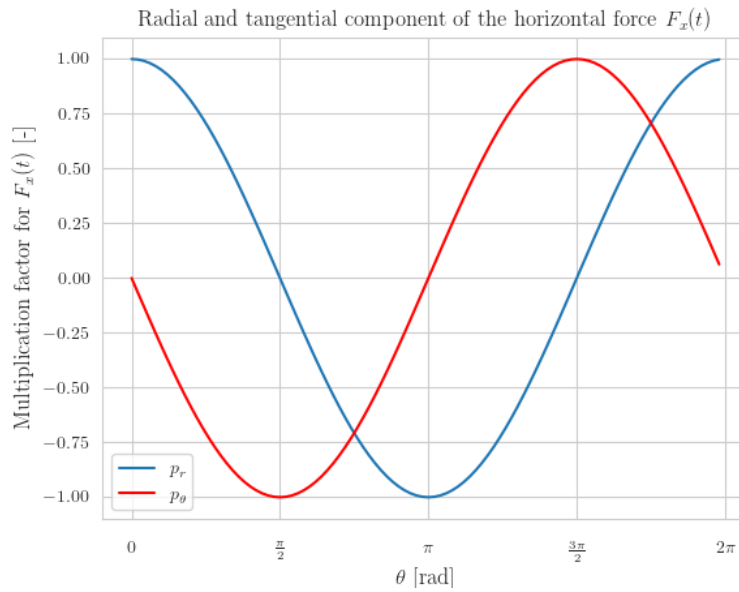
(b) Magnitude of radial and tangential force components p_r and p_θ respectively

Figure 3.5: The polar force components for the transverse force $F_x(t)$

This means that the force will act on both v and w nodes in case of n = 1. The force vector $\mathbf{F}_1$ will be obtained in the same way as for the case $n = 0$ above:

$$\mathbf{F}_1 = \mathbf{p}_{n=1} = \int_0^{2\pi} \left[\mathbf{\Theta}_n^{\mathrm{T}} \mathbf{t}^{(i)} \right] R\mathrm{d}\theta \tag{3.41}$$

with

$$\mathbf{t}^i = \begin{bmatrix} p_z \\ p_\theta \\ p_r \\ m_{zz} \end{bmatrix} = \begin{bmatrix} 0 \\ \dfrac{-F_x(t)\sin(n\theta)}{2\pi R} \\ \dfrac{F_x(t)\cos(n\theta)}{2\pi R} \\ 0 \end{bmatrix} \tag{3.42}$$

Substituting eq. 3.33 and 3.42 in to eq. 3.41 results in:

$$\mathbf{F}_1 = \mathbf{p}_{n=1} = \begin{bmatrix} 0 \\ \dfrac{F_x(t)}{2} \\ \dfrac{F_x(t)}{2} \\ 0 \end{bmatrix} \tag{3.43}$$

Hereafter, the normalization has to be carried out in order to compare to the beam elements. As to be seen from Figure 3.5a the projection p_x and p_y of the components p_r and p_θ on the Cartesian coordinates are defined as follows:

$$p_{x,(r,\theta)} = p_r\cos(\theta) - p_\theta\sin(\theta) \tag{3.44}$$
$$p_{y,(r,\theta)} = p_r\sin(\theta) + p_\theta\cos(\theta) \tag{3.45}$$

which gives:

$$p_x = \int_0^{2\pi} p_{x,(r,\theta)} R d\theta = F_x(t) \tag{3.46}$$

$$p_y = \int_0^{2\pi} p_{y,(r,\theta)} R d\theta = 0 \tag{3.47}$$

In the following section, the modeling of the vibratory hammer will be discussed, including the expressions for the axial and lateral loads $F_z(t)$ and $F_x(t)$ respectively.

3.4. Modeling of the vibratory hammer

In this section the implementation of the vibratory hammer in the finite element (FE) models will be addressed, following the broad discussion of the vibratory hammer mechanism in Chapter 2.

In Figure 3.6 below, one of the hammers used in the study will be broken down into parts and the part names will be assigned.
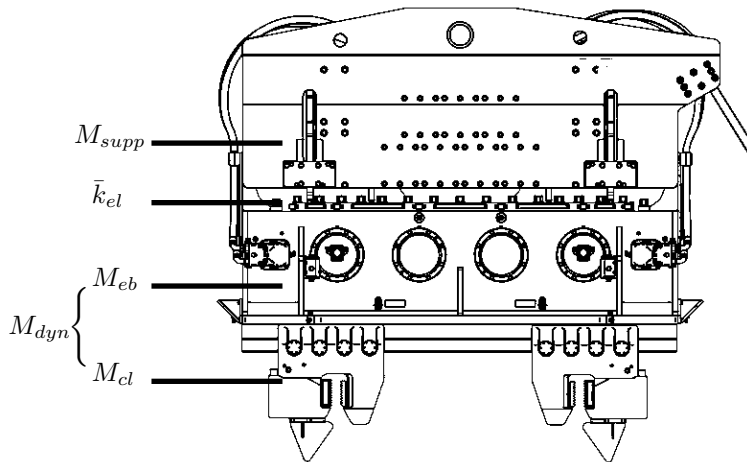
Figure 3.6: Vibratory hammer parts and designation used in this study

M_{supp} represents the suppressor mass, while the stiffness and damping of the elastomer pads are indicated by $\bar{k}_{el}$, which is the sum of the individual values of axial springs k_{el} and damping $c_{el}\frac{d}{dt}$. The excitation block in which the forces $F_z(t)$ and $F_x(t)$ are generated, has a mass of M_{eb}, and the clamps that are rigidly attached to it have a mass of M_{cl}. The total dynamic mass of the system, including both the excitation block and the clamps, is denoted by M_{dyn} and equals $M_{eb} + 2M_{cl}$. The complete mass of the hammer is equal to $M_{supp} + M_{dyn} = M_{vib}$. In all cases, the clamps are connected rigidly to the first element of the pile.

3.4.1. Mechanical action of the hammer

The mechanical action from the hammer in axial and lateral direction will be incorporated in the $n = 0$ and $n = 1$ models respectively.

The axial force is produced by the rotating eccentric masses. Without a misalignment, the vertical force developed by the rotating eccentrics can be defined as follows:

$$F_z(t) = \sum_{}^{N_{me}} me\omega^2 sin(\omega t) \tag{3.48}$$

in which me stands for the eccentric moment in kgm, ω stands for the rotational speed in rad/sec and N_{me} stands for the number of rotating eccentric masses.

However, when a single gear of one pair of rotating eccentrics has a misalignment, this will be incorporated in the developed force in terms of a phase shift φ see Figure 3.7 below. This will alter 3.48 and for one pair of rotating eccentrics is described by eq.3.49

$$F_z(t) = me\omega^2 sin(\omega t) + me\omega^2 sin(\omega t + \varphi) \tag{3.49}$$

From Figure 3.7 below, it can be seen that the phase shift in one rotating mass relative to the other produces a horizontal force $F_x(t)$.

$$F_x(t) = me\omega^2 cos(\omega t + \varphi) - me\omega^2 cos(\omega t) \tag{3.50}$$
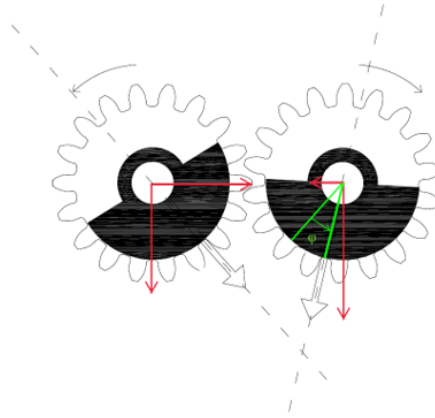
Figure 3.7: Single gear misalignment in one pair of rotating eccentrics in terms of a phase shift φ

Since with increasing pile diameter, also the size as well as the number of hammers and rotating eccentrics increases, the complete vertical and horizontal force $F_z(t)$ and $F_x(t)$ generated by the total amount of gears with only a single gear misaligned in the complete system is described as follows:

$$F_z(t) = (N_{me} - 1)\frac{1}{N_{me}}me\omega^2 sin(\omega t) + \frac{1}{N_{me}}me\omega^2 sin(\omega t + \varphi) \tag{3.51}$$

$$F_x(t) = \frac{N_{me} - 2}{2}\left(-\frac{1}{N_{me}}me\omega^2 cos(\omega t) + \frac{1}{N_{me}}me\omega^2 cos(\omega t)\right) + \tag{3.52}$$
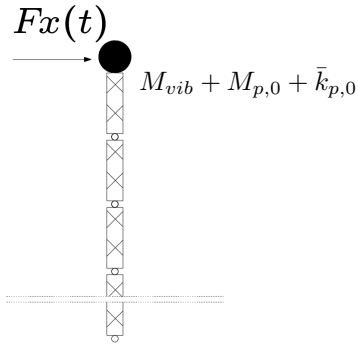
$$\frac{1}{N_{me}}me\omega^2 cos(\omega t + \varphi) - \frac{1}{N_{me}}me\omega^2 cos(\omega t) \tag{3.53}$$

3.4.2. Rigid mass on top

As the vibratory hammer lacks transverse springs, when considering bending motion, it will be represented by a single point mass situated on the pile. This point mass will represent the entire mass of the hammer, which is the sum of M_{supp} and M_{dyn} and is denoted as M_{vib}, as previously noted in this section. It will solely be applied to the beam elements, while the rod elements will incorporate a 2DOF system on top.

Beam elements

Assuming that the clamps are rigidly attached to the pile, the hammer can be modelled as a point mass on top, which would only add mass to the first degree of freedom. Since there are no transverse springs between the suppressor housing and excitation block, the clamps are also rigidly connected to the excitation block and suppressor. As a result, the complete hammer can be considered a point mass added solely to the first degree of freedom of the beam elements, as demonstrated in Figure **??**. The mass of the vibratory hammer, denoted as M_{vib}, will be added to the first component of the mass matrix $\mathbf{M}^e_{1,1}$ in equation 3.27, resulting in the mass matrix for the first element given in eq. 3.54. A complete overview will be provided in section 3.6

$$\mathbf{M}^e = \frac{\rho A \ell}{420} \begin{bmatrix} 156 + \frac{M_{vib}420}{\rho A \ell} & 22\ell & 54 & -13\ell \\ 22\ell & 4\ell^2 & 13\ell & -3\ell^2 \\ 54 & 13\ell & 156 & -22\ell \\ -13\ell & -3\ell^2 & -22\ell & 4\ell^2 \end{bmatrix} \quad (3.54)$$

Figure 3.8: Beam elements with the complete vibratory hammer as point mass on top and the lateral force acting on the pointmass, in which $M_{p,0}$ is the mass and $\bar{k}_{p,0}$ is the stiffness and damping of the first pile element

Ring mass on shell elements

The vibratory hammer mass M_{vib} will be applied to the thin circular cylindrical shell elements as a ring mass, as shown in Figure 3.9. This will be accomplished by using equation 3.41 to apply the mass as a lineload.
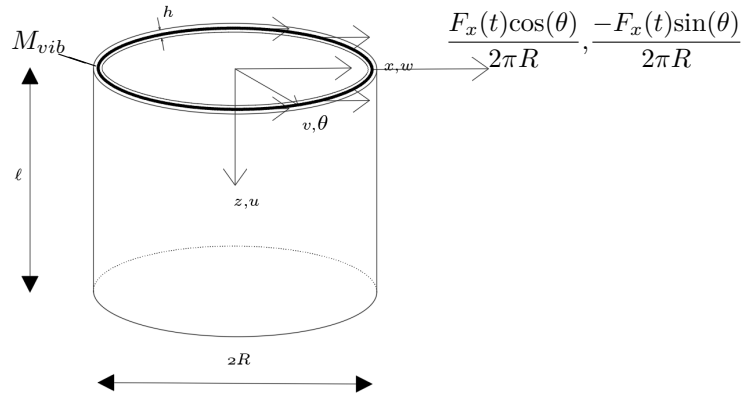
Figure 3.9: Shell element with lateral load and ringmass M_{vib} for the case $n = 1$

To achieve this, it is necessary to modify the boundary conditions for $z = 0$. By adding the mass as a force on the circular cylindrical shell elements, the boundary conditions at $z = 0$ can be altered, as described in [43]:

$$N_z + m\ddot{u} \qquad\qquad = \quad 0 \tag{3.55}$$

$$N_{z\theta} + \frac{1}{R_p}M_{z\theta} + m\ddot{v} \quad = \quad 0 \tag{3.56}$$

$$Q_z + \frac{1}{R_p}\frac{\partial M_{z\theta}}{\partial \theta} + m\ddot{w} \quad = \quad 0 \tag{3.57}$$

$$M_z \qquad\qquad = \quad 0 \tag{3.58}$$

in which the rigid ring mass m is a distributed mass along the circumference of the cylindrical shell $m = \dfrac{M_{vib}}{2\pi R}$, in which M_{vib} is the total mass of the vibratory hammer. The last terms of eq. 3.56 to 3.58 are substituted in to eq. 3.41, with:

$$\mathbf{t}^i = \begin{bmatrix} m\ddot{u} \\ m\ddot{v} \\ m\ddot{w} \\ 0 \end{bmatrix} = \begin{bmatrix} m & 0 & 0 & 0 \\ 0 & m & 0 & 0 \\ 0 & 0 & m & 0 \\ 0 & 0 & 0 & 0 \end{bmatrix} \begin{bmatrix} \ddot{u}^{(i)} \\ \ddot{v}^{(i)} \\ \ddot{w}^{(i)} \\ \ddot{\beta_z}^{(i)} \end{bmatrix} = \mathbf{M}_{vib}^{(i)}\ddot{\mathbf{u}}^{(i)} \tag{3.59}$$

The solution is formulated in the form given by eq. 3.32. By considering only the top boundary, filling in $z = 0$ in the shape function matrix in eq. 3.34 eliminates the second node terms from the shape function matrix, resulting in:

$$\ddot{\mathbf{u}}^{(0)} = \mathbf{\Theta}_n\mathbf{N}(z=0)\ddot{\mathbf{u}}_n^{(0)}, \quad \ddot{\mathbf{u}}_n^{(0)} = \begin{bmatrix} \ddot{u}_n^{(0)} & \ddot{v}_n^{(0)} & \ddot{w}_n^{(0)} & \ddot{\beta}_{z,n}^{(0)} \end{bmatrix}^{\mathrm{T}} \tag{3.60}$$

Substituting equation 3.60 in to equation 3.59, the following is obtained:

$$\mathbf{t}^{(i)} = \mathbf{M}_{vib}^{(i)}\mathbf{\Theta}_n\mathbf{N}^{(i)}\ddot{\mathbf{u}}_n^{(i)} \tag{3.61}$$

Consequently, substituting equation 3.61 in to equation 3.41, one obtains:

$$\mathbf{p}_n^l = \underbrace{\int_0^{2\pi}\left[\mathbf{\Theta}_n^{\mathrm{T}}\mathbf{M}_{vib}^{(0)}\mathbf{\Theta}_n\mathbf{N}(z=0)\right]R\mathrm{d}\theta}_{\mathbf{M}_{n,ring}}\begin{bmatrix} \ddot{\mathbf{u}}_n^{(1)} \end{bmatrix} \tag{3.62}$$

By evaluating the integral, the ring mass matrix for $n = 1$ given in equation 3.63 is obtained. As only node $i = 0$ has added mass, the resulting matrix, denoted $\mathbf{M}n, ring$, is a 4×4 matrix. The elements of this ring mass matrix will then be incorporated into the first three elements, $M_{1,1}$, $M_{2,2}$, and $M_{3,3}$, of the thin cylindrical circular shell mass matrix $\mathbf{M}_{n=1}$ provided in Appendix A, equation A.3.

$$\mathbf{M}_{n,ring} = \frac{M_{vib}}{2}\begin{bmatrix} 1 & 0 & 0 & 0 \\ 0 & 1 & 0 & 0 \\ 0 & 0 & 1 & 0 \\ 0 & 0 & 0 & 0 \end{bmatrix} \tag{3.63}$$

3.4.3. 2 DOF system

As the vibratory hammer is assumed to only have axial springs, the vibratory hammer as a 2DOF system will be applied on the 1D bar elements and the $n = 0$ case in the circular cylindrical shell elements which cover the axisymmetric longitudinal motion of the model. As stated in the introduction of this section, the 2 DOF vibratory hammer is rigidly attached to the first pile element, irrespective of the element type. This implies that an extra degree of freedom, denoted as u_{supp}, for the suppressor motion must be incorporated into the overall system for both types of elements.

Bar elements

For rod elements, the hammer-pile-soil system (with Free-Free BC's) will comprise of $N^e + 1$ elements, which will add an extra degree of freedom to the system, leading to a total of $1N^e + 2$ degrees of freedom.

To incorporate the mass of the suppressor housing, M_{supp}, an extra degree of freedom is added to the mass matrix $\mathbf{M}^e$ in equation 3.17. The dynamic mass M_{dyn}, which comprises of the mass of the excitation block M_{eb} and clamps M_{cl} rigidly connected to each other and to the pile, will be added to the first component of the mass matrix $M_{1,1}^e$ in equation 3.17, thereby resulting in the mass matrix for the first element, as given in equation 3.64. For clarification, the hammer-pile system is demonstrated in Figure 3.10 below.

The same procedure will be applied on the stiffness matrix given in eq. 3.18. This results in the stiffness matrix $\mathbf{K}^e$ in eq. 3.64, including the vibratory hammer as a 2DOF system.

$$\mathbf{M}^e = \begin{bmatrix} M_{supp} & 0 & 0 \\ 0 & \frac{\rho A \ell}{3} + M_{dyn} & \frac{\rho A \ell}{6} \\ 0 & \frac{\rho A \ell}{6} & \frac{\rho A \ell}{3} \end{bmatrix}$$

$$\mathbf{K}^e = \begin{bmatrix} 2k_{el} & -2k_{el} & 0 \\ -2k_{el} & 2k_{el}l + \frac{EA}{\ell} & -\frac{EA}{\ell} \\ 0 & -\frac{EA}{\ell} & \frac{EA}{\ell} \end{bmatrix}$$

(3.64)
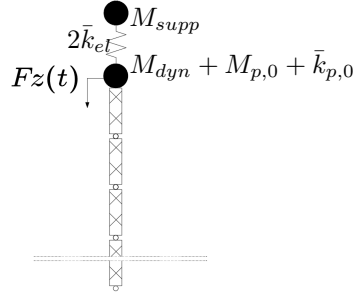
Figure 3.10: Bar elements with the vibratory hammer as 2 DOF system on top and the axial force acting on the excitation block, in which $M_{p,0}$ is the mass and $\bar{k}_{p,0}$ is the stiffness and damping of the first pile element

The addition of the remaining mass and stiffness matrix elements goes the same way as given in eq. 3.19. After adding the soil reaction in following sections, the complete overview will be provided in section 3.6

Shell elements

In the same way as in the bar elements, an additional DOF will be added to the total number of DOF's in the complete system. This DOF will only be in the axisymmetric longitudinal direction u. The mass M_{supp} will be added as the extra DOF, and the mass M_{dyn} will be added to the mass matrix of the first pile element. The thin circular cylindrical shell element for the axisymmetric case $n = 0$ with a vibratory hammer modelled as a 2DOF system is illustrated in Figure 3.11.
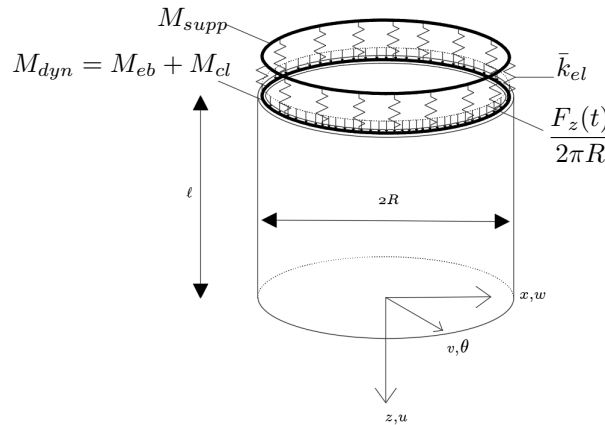
Figure 3.11: Shell element with axial load and hammer as 2DOF system in which ringmass M_{supp} and ringmass M_{dyn} are connected through the elastomer spring dashpot system $\bar{k}_{el}$ for the case $n = 0$. The lineload $\frac{F_z(t)}{2\pi R}$ is applied at M_{dyn}

The ringmasses for both M_{supp} and M_{dyn} are obtained in the same way as discussed earlier in section 3.4.2, using eq. 3.37. For the ringmass M_{dyn} rigidly attached on the pile, the following boundary conditions from [43] will be used:

$$N_z + m\ddot{u} \qquad\qquad = \quad 0 \tag{3.65}$$

$$Q_z + \frac{1}{R_p}\frac{\partial M_{z\theta}}{\partial \theta} + m\ddot{w} \quad = \quad 0 \tag{3.66}$$

$$M_z \qquad\qquad\qquad = \quad 0 \tag{3.67}$$

in which m is the distributed dynamic mass $\frac{M_{dyn}}{2\pi R}$.

For the suppressor housing ringmass M_{supp} and the elastomer stiffness and damping $\bar{k}_{el}$, the following boundary conditions will be used:

$$N_z + m\ddot{u} \quad = \quad 0 \tag{3.68}$$

$$N_z + k_{el}u \quad = \quad 0 \tag{3.69}$$

in which m is the distributed suppressor housing mass $\frac{M_{supp}}{2\pi R}$ and k_{el} are the distributed springs. As to be seen from eq. 3.68, the suppressor housing only has the axial DOF u, and therefore it is sufficient to add a single row and column to the existing mass and stiffness matrices given in Annex A eq. A.1 and A.2 respectively.

The same procedure as in section 3.4.2, eq. 3.59 to 3.62 is followed to obtain the mass matrices for the ring mass M_{supp} and M_{dyn}. However, the vector $\mathbf{t}$ in eq. 3.59 for the dynamic ring mass will be

$$\mathbf{t}^i = \begin{bmatrix} m\ddot{u} \\ m\ddot{w} \\ 0 \end{bmatrix} = \begin{bmatrix} m & 0 & 0 \\ 0 & m & 0 \\ 0 & 0 & 0 \end{bmatrix} \begin{bmatrix} \ddot{u}^{(i)} \\ \ddot{w}^{(i)} \\ \ddot{\beta}_z^{(i)} \end{bmatrix} = \mathbf{M}_{dyn}^{(i)}\ddot{\mathbf{u}}^{(i)} \tag{3.70}$$

and for the suppressor housing ring mass:

$$\mathbf{t}^i = \begin{bmatrix} m\ddot{u} \\ 0 \\ 0 \end{bmatrix} = \begin{bmatrix} m & 0 & 0 \\ 0 & 0 & 0 \\ 0 & 0 & 0 \end{bmatrix} \begin{bmatrix} \ddot{u}^{(i)} \\ \ddot{w}^{(i)} \\ \ddot{\beta}_z^{(i)} \end{bmatrix} = \mathbf{M}_{supp}^{(i)}\ddot{\mathbf{u}}^{(i)} \tag{3.71}$$

For the sake of completeness, the mass for the suppressor housing is written as a vector term, however, only the axial motion u will be considered. After following the same procedure as mentioned above, the mass matrices for the $n = 0$ case are obtained:

$$\mathbf{M}_{0,ring,dyn} = M_{dyn}\begin{bmatrix} 1 & 0 & 0 \\ 0 & 1 & 0 \\ 0 & 0 & 0 \end{bmatrix} \tag{3.72}$$

and

$$\mathbf{M}_{0,ring,supp} = M_{supp}\begin{bmatrix} 1 & 0 & 0 \\ 0 & 0 & 0 \\ 0 & 0 & 0 \end{bmatrix} \tag{3.73}$$

To clarify the process, the dynamic ring mass elements $M_{1,1}$ and $M_{2,2}$ in eq. 3.72 will be integrated into the existing mass matrix M_0, at the corresponding positions as in Annex A, eq. A.1. On the other hand, the suppressor housing mass will be added as an extra DOF above the existing mass matrix M_0, disregarding the zeros in $\mathbf{M}_{0,ring,supp}$. Similarly, the stiffness terms will be integrated into the stiffness matrix $\mathbf{K}_0$ from Annex A, eq. A.2, with an additional DOF on top of the matrix. The stiffness terms for the elastomer pads, k_{el}, will remain unchanged and in the same positions as in the bar elements shown in eq. 3.64.

3.5. Soil model

To investigate how the pile response is affected by embedment depth, a simple soil reaction will be assigned to the element nodes of all types of elements.

A Winkler-type linear elastic foundation is utilized, employing this method on both axial and transverse soil springs. This foundation model calculates the corresponding reaction force per unit length, which is proportional to the element's deflection. The soil stiffness matrix matrix of the linear foundation is given by [44] [45]:

$$\mathbf{K}_s = \int_0^\ell \mathbf{N}(z)^{\mathrm{T}} k_s \mathbf{N}(z) \mathrm{d}z \tag{3.74}$$

in which the soil stiffness parameter is denoted by k_s. By inserting the shape functions from equation 3.13 into equation 3.74, and replacing the soil stiffness parameter k_s with k_a, the axial soil stiffness matrix is obtained:

$$\mathbf{K}_{s,a} = \frac{k_a \ell}{6} \begin{bmatrix} 2 & 1 \\ 1 & 2 \end{bmatrix} \tag{3.75}$$

By using a similar approach for the transverse soil stiffness matrix, the shape functions from equation 3.21 can be substituted into equation 3.74. By replacing the soil parameter k_s with k_t, the resulting matrix is the transverse soil stiffness matrix:

$$\mathbf{K}_{s,t} = \frac{k_t \ell}{420} \begin{bmatrix} 156 & 22\ell & 54 & -13\ell \\ 22\ell & 4\ell^2 & 13\ell & -3\ell^2 \\ 54 & 13\ell & 156 & -22\ell \\ -13\ell & -3\ell^2 & -22\ell & 4\ell^2 \end{bmatrix} \tag{3.76}$$

It has been observed that the soil stiffness matrix for bar and beam elements is equivalent to the mass matrix. This same concept is applied to shell elements. To obtain the axisymmetric ($n = 0$) soil stiffness matrix, the mass matrix provided in Annex A, equation A.1, is utilized. The soil stiffness parameter k_a replaces the mass per meter parameter ρA in the matrix.

Similarly, the transverse soil stiffness matrix is obtained using the mass matrix from $n = 1$ motion, equation A.3 in Annex A, where the soil stiffness parameter k_t replaces the mass per meter ρA in the matrix.

The next section provides a comprehensive overview of the hammer-pile-soil system, which includes the integration of the hammer and soil with the pile elements.

3.6. Overview of complete hammer-pile-soil system

Now that all the elements in the model have been presented, the next section will provide a detailed overview of the main models, namely the thin circular cylindrical shell elements, along with their corresponding validation models. By verification models, I refer to the bar and beam elements. Specifically, the bar elements are utilized for the shell elements with axisymmetric case $n = 0$, while beam elements are used for the bending-like motion case $n = 1$.

On the left side of Figure 3.12, thin circular cylindrical shell elements for the axisymmetric longitudinal motion ($n = 0$) is presented. Meanwhile, the validation model is shown on the right side using 1D bar elements. Both models incorporate a 2DOF system vibratory hammer situated on top of the pile elements. The first degree of freedom corresponds to the suppressor housing mass, denoted as M_{supp}, and subsequently, the dynamic mass M_{dyn} which includes the mass of the excitation block M_{eb} and the hydraulic clamps M_{cl}, which are rigidly attached to the pile. Depending on the depth of embedment L_{embed} , the soil reaction denoted as k_a for the axisymmetric case, is introduced to the hammer-pile-soil system at the bottom part of the pile.
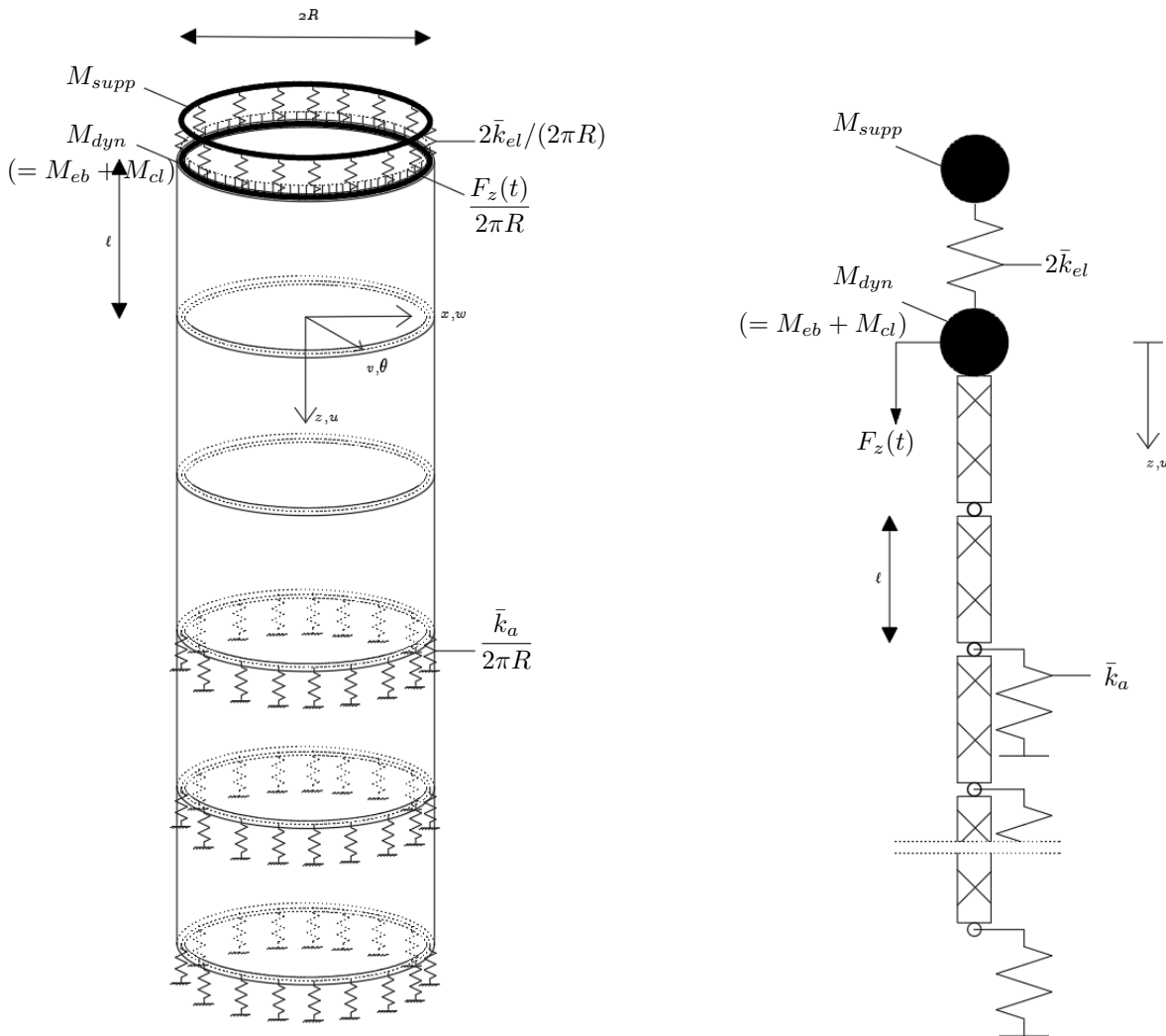
Figure 3.12: Complete overview for the axial response of the hammer-pile-soil system, left with axisymmetric shell elements $n = 0$ and right with 1D bar elements.

Similarly, Figure 3.13 depicts the presentation of thin circular cylindrical shell elements for the lateral motion ($n = 1$) on the left side, whereas the validation model using 1D beam elements is shown on the right side. Both models involve a vibratory hammer placed on top of the pile elements as a rigid mass denoted as M_{vib}, in the form of a ringmass for shell elements and a pointmass for 1D beam elements and is rigidly connected to the pile. The introduction of the transverse soil reaction, indicated as k_t for the $n = 1$ case, to the hammer-pile-soil system at the lower part of the pile, depends on the depth of embedment L_{embed}.
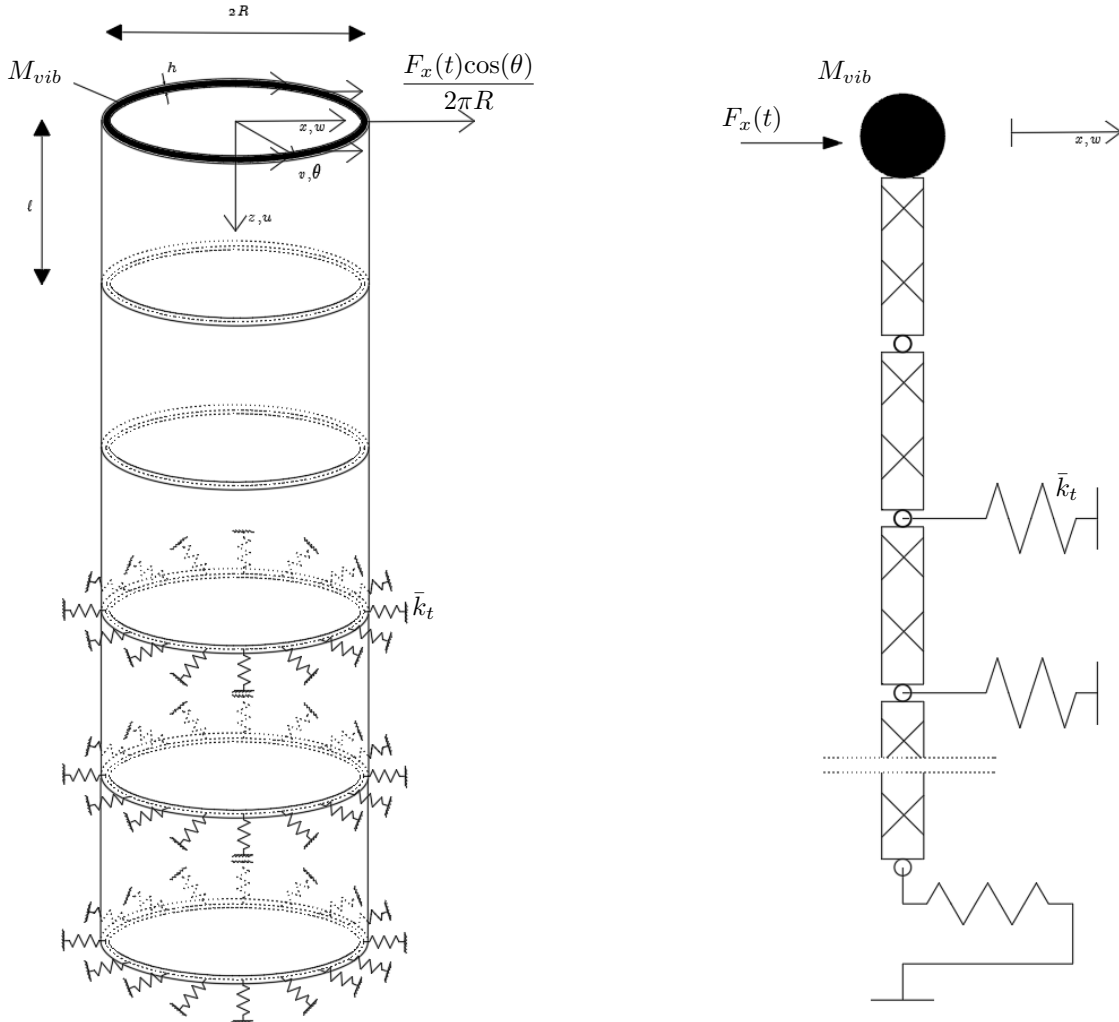
Figure 3.13: Complete overview for the response in lateral motion of the hammer-pile-soil system, on the left with shell elements $n = 1$ and on the right with 1D beam elements.

3.7. Validation of the shell model

Validation of the shell models for $n = 0$ and $n = 1$ will involve comparing their natural frequencies and time-domain responses to those of the bar and beam elements, respectively. A slender pile with dimensions as specified in Table 4.1 will be utilized for all the models, as the response of a slender shell element is similar to that of 1D bar or beam elements. Additionally, the natural frequencies of the bar and beam elements will be validated by comparing them to the analytical solution.

3.7.1. Modal analysis

To reduce computational time, modal analysis will be employed in all models, resulting in significantly smaller matrices to be computed in the finite element analysis (FEA). The determination of which modes to include in the modal analysis will depend on each mode's contribution to the displacement. Moreover,

in finite element approximation, the natural frequencies of higher-order modes tend to be higher than those obtained through analytical solutions. Hence, a comparison of the numerically obtained natural frequencies to those obtained analytically will be performed to ensure that the participating modes in the modal analysis have an error of less than 5% of the analytical solution.

3.7.2. Participating modes

Participation factor and effective mass

To quantify the most important modes and the number of modes to extract, the mode participation factor and the effective mass will be used. The mode participation factor is described as

$$\gamma_i = \{\Phi\}_i^T [M] \{D\} \tag{3.77}$$

in which

- γ_i is the participation factor of the ith mode
- $\{\Phi\}_i$ is the ith mass normalized eigen vector
- $[M]$ is the mass matrix
- $\{D\}$ is an assumed unit displacement vector and depends on the direction of the excitation.

and the effective mass (per mode i)

$$M_{eff,i} = \gamma_i^2 \tag{3.78}$$

which is the amount of mass moving in each direction of each mode. The modes included are sufficient after the total effective mass M_{eff} reaches a ratio of at least 0.9 to the total mass of the pile M_p

$$\sum_{i=0}^{m_{max}<N} M_{eff,i} \geqslant 0.9 M_p \tag{3.79}$$

with m_{max} being the highest mode number to participate, which is less than the total number of modes N.

The contribution of each mode to the quantity of mass that is excited in each direction with various types of finite elements, is displayed in Figure 3.14 below. The pile properties given in table 4.1 have been applied to this with clamped-free boundary conditions.
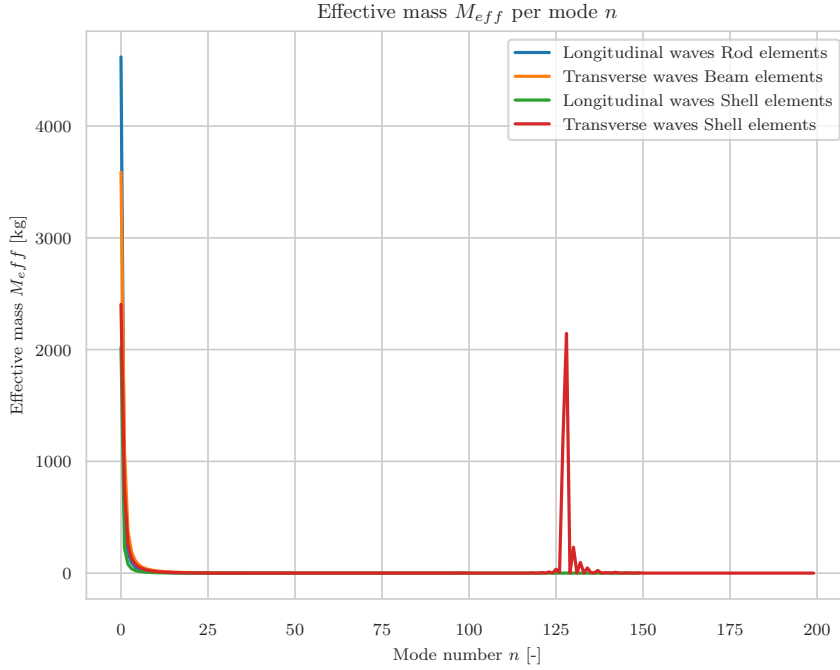
Figure 3.14: Effective mass per mode for longitudinal and transverse waves for different element types

As to be seen from this graph, after approximately the 10th mode, the contribution of the modes are not significant anymore to the amount of excited mass. Applying $m_{max} = 10$ to eq. 3.79 results in a total effective mass of

$$M_{eff,t} = 0.96M_p$$
$$M_{eff,l} = 0.95M_p$$
$$M_{eff,t,shell} = 0.97M_p$$
$$M_{eff,l,shell} = 0.95M_p$$

with t and l subscripts being the transverse and longitudinal waves respectively. The transverse waves from shell elements experience a remarkable phenomenon in that a significant peak is observed close to mode number 125. This is either a numerical error or indicates that a sizable quantity of mass is excited by this mode. This behavior will be disregarded nevertheless because this mode is associated with extremely high frequencies, in which the pile will never be excited. This denotes that only the first 10 modes will be taken into account in the modal analysis.

Comparison of analytical and numerical natural frequencies
In addition to the modal participation analysis, the natural frequencies of the modes considered will also be compared from both numerical and analytical solutions to make sure that the numerical solution is accurate enough, with an error range of no more than 5%.
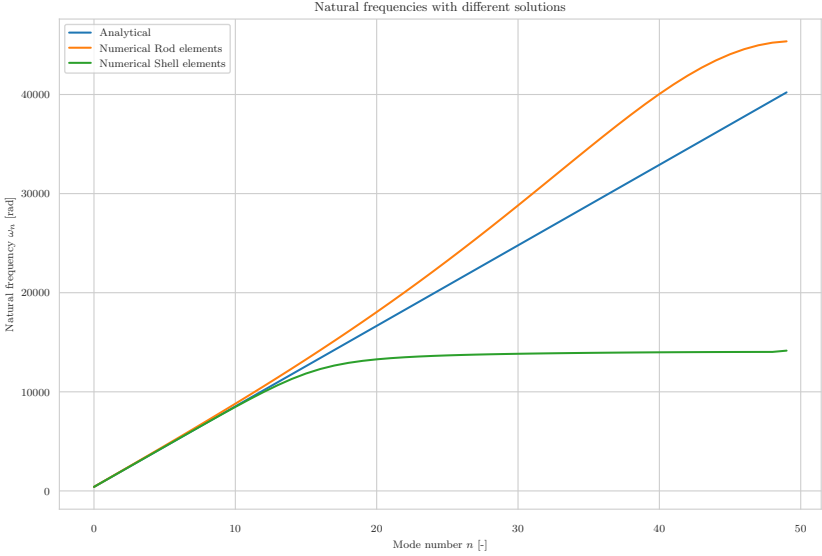
Figure 3.15: Comparison of the natural frequencies with different solutions for (axial) axisymmetric model

The graph in Figure 3.15 compares the analytical and numerical solutions for the natural frequencies of axial vibrations, and demonstrates that the two methods produce nearly identical results up to at least the 10th mode. A similar analysis was performed for bending vibrations, as illustrated in Figure 3.16. The excellent agreement between the analytical and numerical results in both cases provides strong evidence for the accuracy and reliability of the computational approach.
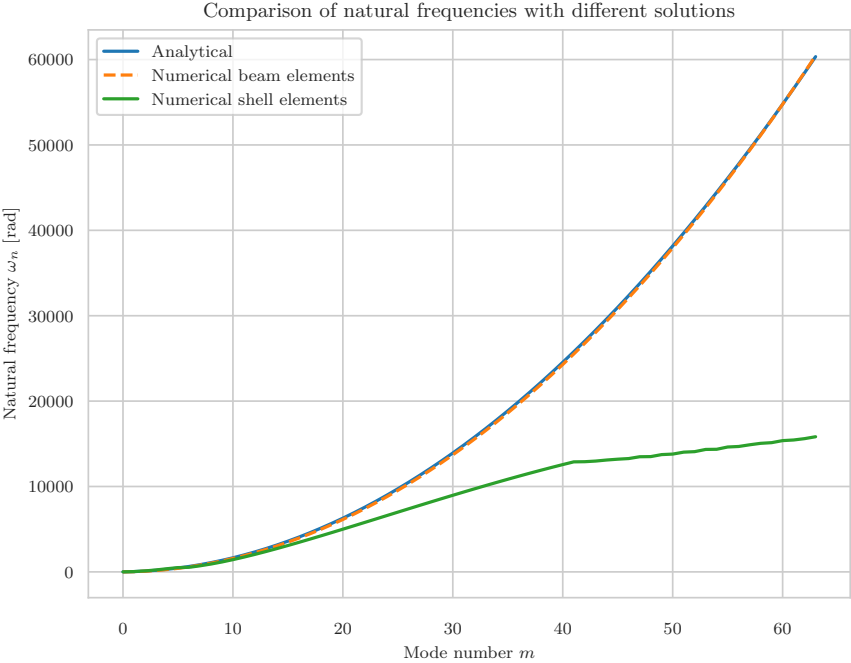
Figure 3.16: Comparison of the natural frequencies with different solutions for bending ($n = 1$) model

3.7.3. Application of modal analysis

Having the maximum number of modes to be included allows us to apply the modal analysis to all three element types. It will then be used in the numerical analysis with the reduced matrices.

In section 3.1.1 the eigenvalue problem is solved resulting in the natural frequencies and natural modes of the system. The modal analysis will be applied with the reduced modal matrix:

$$\mathbf{\Phi}_{red} = \begin{bmatrix} \mathbf{\phi}_1 & \mathbf{\phi}_2 & ... & \mathbf{\phi}_m \end{bmatrix}, \quad m = 10 \tag{3.80}$$

Recalling the original equation of motion of the damped system:

$$\mathbf{M}\ddot{\mathbf{u}}(t) + \mathbf{C}\dot{\mathbf{u}}(t) + \mathbf{K}\mathbf{u}(t) = \mathbf{F}(t) \tag{3.81}$$

and considering the modal transformation in which the physical displacements $\mathbf{u}(t)$ are set as a function of the modal coordinates $\mathbf{q}(t)$:

$$\mathbf{u}(t) = \mathbf{\Phi}_{red}\mathbf{q}(t) \tag{3.82}$$

Substituting equation 3.82 in to the original equation of motion 3.81 and pre-multiplying every term by the transpose of the reduced modal matrix, one obtains:

$$(\mathbf{\Phi}^{\mathrm{T}}\mathbf{M}\mathbf{\Phi})\ddot{\mathbf{q}}(t) + (\mathbf{\Phi}^{\mathrm{T}}\mathbf{C}\mathbf{\Phi})\dot{\mathbf{q}}(t) + (\mathbf{\Phi}^{\mathrm{T}}\mathbf{K}\mathbf{\Phi})\mathbf{q}(t) = \mathbf{\Phi}^{\mathrm{T}}\mathbf{F}(t) \tag{3.83}$$

The modal mass, stiffness and damping matrices and the modal force vector are defined by the term within the parenthesis in equation 3.83:

$$\mathbf{M}_m = \mathbf{\Phi}_{red}^{\mathrm{T}}\mathbf{M}\mathbf{\Phi}_{red} \tag{3.84}$$

$$\mathbf{K}_m = \mathbf{\Phi}_{red}^{\mathrm{T}}\mathbf{K}\mathbf{\Phi}_{red} \tag{3.85}$$

$$\mathbf{C}_m = \mathbf{\Phi}_{red}^{\mathrm{T}}\mathbf{C}\mathbf{\Phi}_{red} \tag{3.86}$$

$$\mathbf{Q} = \mathbf{\Phi}_{red}^{\mathrm{T}}\mathbf{F}(t) \tag{3.87}$$

in which the modal matrices are reduced to diagonal $m \times m$ matrices with unit values in the diagonals of the modal mass matrix $\mathbf{M}_m$ and frequency squared values on the diagonals of the modal stiffness matrix $\mathbf{K}_m$ and the force vector to $m \times 1$. Compared to using all the modes, this drastically cuts down on computation time without derogating from the accuracy.

Before implementing it in the Python solver for ODE's, the initial conditions have to be specified in modal space:

$$\{\mathbf{q}_0, \dot{\mathbf{q}}_0\}^{\mathrm{T}} = \{\mathbf{0}, \mathbf{0}\}^{\mathrm{T}} \tag{3.88}$$

The same procedure has been followed for all three element types and solved with a Python ODE solver which returns displacements and velocities in modal coordinates:

$$\left\{ \frac{\mathbf{q}_{(t=t_k)}}{\dot{\mathbf{q}}_{(t=t_k)}} \right\} = \begin{bmatrix} q_{1,t_0} & \cdots & q_{1,t_{end}} \\ q_{2,t_0} & \cdots & q_{2,t_{end}} \\ \vdots & \cdots & \vdots \\ q_{m,t_0} & \cdots & q_{m,t_{end}} \\ \dot{q}_{1,t_0} & \cdots & \dot{q}_{1,t_{end}} \\ \dot{q}_{2,t_0} & \cdots & \dot{q}_{2,t_{end}} \\ \vdots & \cdots & \vdots \\ \dot{q}_{m,t_0} & \cdots & \dot{q}_{m,t_{end}} \end{bmatrix}, k = 0,...,end \quad \left(= \frac{t_{signal}}{\Delta t} \right) \tag{3.89}$$

The system response in physical coordinates is obtained using the modal transformation:

$$\mathbf{u}_{(t)} = \mathbf{\Phi}_{red}\mathbf{q}_{(t=t_k)} = \sum_{j=0}^{m} \mathbf{\phi}_j q_{j\,(t=t_k)} \tag{3.90}$$

$$\dot{\mathbf{u}}_{(t)} = \boldsymbol{\Phi}_{red}\dot{\mathbf{q}}_{(t=t_k)} = \sum_{j=0}^{m} \boldsymbol{\phi}_j \dot{q}_{j\,(t=t_k)}, \quad k = 0, ..., \frac{t_{signal}}{\Delta t} \tag{3.91}$$

$$\ddot{\mathbf{u}}(t) = \frac{\mathrm{d}\dot{\mathbf{u}}(t)}{\mathrm{d}t} = \frac{\dot{\mathbf{u}}_{(t_{k+1})} - \dot{\mathbf{u}}_{(t_k)}}{t_{k+1} - t_k} \tag{3.92}$$

in which each displacement vector $\mathbf{u}_{(t)}$ and velocity vector $\dot{\mathbf{u}}_{(t)}$ is a vector of time instant $t = t_k$.

3.7.4. Computational analysis for comparative results

Modal analysis was conducted on all models, and the time domain responses were compared specifically for the slender pile, with properties outlined in Table 4.1. The comparative analysis involved comparing the models from Figure 3.12 to each other, and similarly for the models from Figure 3.13. Some of the time-domain responses are included in Annex B Figure B.1 through Figure B.6.

Analysis of the time-domain responses reveals that the (axial) axisymmetric model aligns perfectly with the 1D bar elements, as well as the beam elements and the shell model for $n = 1$ motion. With the validation of the models complete, the following section will focus on the parametric study.

3.8. Overview parametric study

The parametric study will be carried out for the models discussed in section 3.6 and various parameters.

First, the study aims to compare the force transfer ratio of models with and without a modeled 2DOF hammer system to the force transfer ratio found in previous numerical and experimental studies [11]. This will determine whether modeling the hammer as a 2DOF system is more realistic than simply considering it as a force. The results of this comparison will allow us to understand the difference between the actual force transferred by the hammer and the assumed force in practice. This comparison will be conducted for both a circular cylindrical shell model and a simple bar model. This will determine whether it is important to not only accurately model the hammer, but also the pile, especially for piles with larger diameters. Carrying out this study for all the different parameters will also allow to not only see the effect with larger diameters, but also the effect with various forcing frequencies and gear misalignment.

Second, the relative motion between the pile and suppressor will be analyzed for different parameters. This will allow to understand which forcing frequencies more effectively activate the elastomere pads in the vibro-hammer, and how pile diameter influences this effect.

Finally, the impact of misalignment on the power consumption of the pile will be examined. The response of the pile to near frequencies will also be studied. For each degree of misalignment, the percentage of power that goes into bending waves will be calculated, with the assumption that all power goes into axial waves. The effect of various forcing frequencies and different pile diameters will also be analyzed.

3.8.1. Models

The parameters from Table 4.2 above will be used as an input for the following models.Furthermore, to study what the effect of the soil stiffness will be, the four main parameters from Table 4.2 will be studied for all the models with the standard soil stiffness values given in Table 4.1 and for the soil stiffness that is twice the value of $k_{s,a}$ and $k_{s,t}$. To avoid confusion, the models used in the study will be assigned specific names for reference in the subsequent chapters.

Thin circular cylindrical shells

An overview of the models for thin circular cylindrical shells with their corresponding outputs are given in Figure 3.17 below:
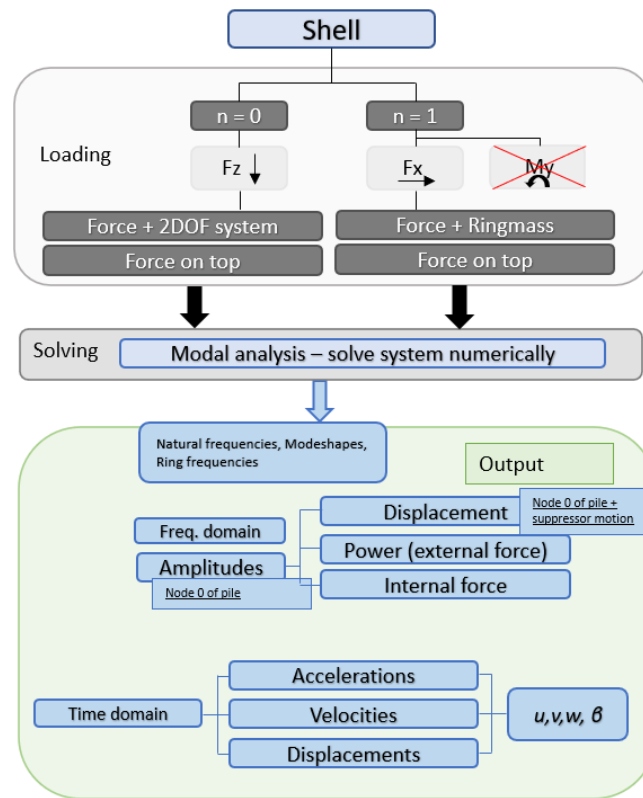
Figure 3.17: Model scheme for thin circular cylindrical shells

Four cases will be studied, as shown in the figure. These include a model with $n = 0$ with and without the hammer modeled as a 2DOF system, and a model with $n = 1$ with and without the hammer modeled as a ringmass. As previously mentioned, the hammer is only considered as a ringmass in the bending model ($n = 1$) because no translational springs are included in the hammer model.

The main outputs of these models will be used to determine the power consumption in axial and bending waves, as well as to compare the force transfer ratio and the relative motion of the pile to the suppressor, as described in Section 3.8 above.

Rod and beam model

A parametric study will also be conducted for the simple bar model in order to compare it to existing engineering models, see Figure 3.18 below. The purpose of the parametric study on the bar model is to contrast the results with the proposed model. On the other hand, the beam model will not undergo a parametric study, it will only serve as a verification of the shell model for the case $n = 1$.
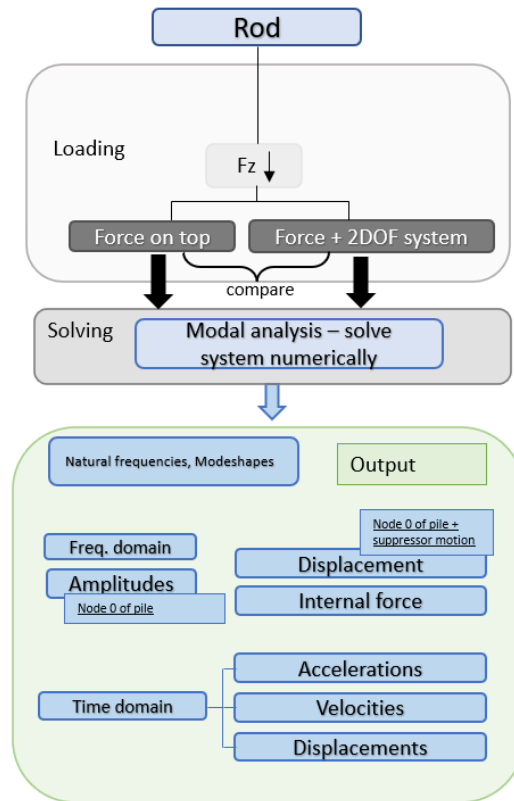
Figure 3.18: Model scheme for bar elements

Two scenarios will be examined for the bar elements. The first scenario assumes that the hammer force is applied at the top of the bar, which is comparable to current engineering models in practice. The second scenario will examine a model in which the hammer is a 2DOF system and the force generated by the rotating eccentrics is included in the 2nd degree of freedom, as explained in 3.4, which will be compared to the results from the first scenario. Additionally, the difference in the results between larger diameters will be compared to those of the shell models.

Model names

A complete overview of the specific names assigned to these models are given in Table 3.1 below:

Model names			
Element type	Load direction	Hammer model	Name
Thin circular cylindrical shell	Axial ($n = 0$)	2DOF system	shell$_{a,sys}$
Thin circular cylindrical shell	Axial ($n = 0$)	no	shell$_{a,f}$
1D Bar elements	Axial	2DOF system	bar$_{sys}$
1D Bar elements	Axial	no	bar$_f$
Thin circular cylindrical shell	Bending ($n = 1$)	Ringmass	shell$_{b,sys}$
Thin circular cylindrical shell	Bending ($n = 1$)	no	shell$_{b,f}$
1D Beam element	Bending	Pointmass	beam$_{sys}$
1D Beam element	Bending	no	beam$_f$

Table 3.1: Hammer-pile-soil system model names

The table indicates that any representation of a hammer model, whether it has 2 degrees of freedom or is a simplified point mass or ring mass, is designated with the subscript "*sys*". Furthermore, the subscript f stands for *force*, a for *axial* and b for *bending*.

4
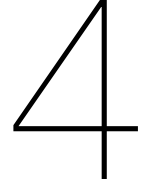
Results and discussion

In this chapter, the results from a study on the dynamics of vibratory hammer-pile-soil systems will be presented and discussed. The force transfer from the hammer to the pile will be examined and how it is affected by various factors such as pile diameter and forcing frequencies will be investigated. The effect of misalignment on power consumption by bending-like motion (lateral pile motion described by $n = 1$) will be studied. Furthermore, the activation of the elastomer pads in the hammer will be analyzed and how it affects the system's dynamics will be evaluated. Through this analysis, the goal is to provide a comprehensive understanding of the behavior of vibratory hammer-pile-soil systems and the factors that influence their performance.

To provide contextual support for the interpretation of the results, a brief overview of the background information will be presented first. Then, the results will be presented and the discussion will be centered around the objectives and research questions, and will be substantiated by the results obtained from the assessment, as well as those found in the literature review. Results and discussions starting with the force transfer and moving on to the activation of the elastomer pads and finally the effect of a misalignment on power consumption. The results will be supported by figures and tables, and the key findings will be highlighted.

To facilitate a clear comparison, the amplitudes generated by the rotating eccentric masses are normalized with respect to the amplitude generated by the first forcing frequency from the parametric study:

$$\xi_i = \frac{F_{c,1}}{F_{c,i}} = \frac{me(2\pi f_1)^2}{me(2\pi f_i)^2}, \quad i = 1, 2, .., 5 \tag{4.1}$$

in which $F_{c,i}$ is the amplitude caused by the i-th rotating frequency f_i.

4.1. Input variables

To provide a comprehensive understanding of the results obtained, this chapter will first outline the input properties of the hammer-pile-soil system.

4.1.1. Parameters

For the parametric study, the general hammer-pile-soil properties are given in Table 4.1.

Description of the model properties			
General properties	Symbol	Value	Unit
Young's modulus	E	$2.1e10^{11}$	N/m^2
Steel density	ρ	7850	kg/m^3
Steel Poission's ratio	ν	0.3	-
Steel damping ratio	ζ	0.0015	-
axial soil stiffness	$k_{s,a}$	$6e10^6$	N/m^3
Transverse soil stiffness	$k_{s,t}$	$1.5e10^7$	N/m^3
axial soil damping	$c_{s,a}$	$1.7e10^4$	Ns/m^3
Transverse soil damping	$c_{s,t}$	$1.5e10^4$	Ns/m^3
Vibrohammer elastomere pads stiffness	k_{el}	$110e10^6$	N/m
Vibrohammer elastomere pads damping	c_{el}	$0.54e10^6$	Ns/m
Slender model pile properties $\lambda << 1$			
Diameter	D	0.762	m
Length	L	30	m
Wallthickness	h_p	0.0159	m

Table 4.1: Vibratory hammer, pile and soil properties

The input variables for the parametric study are given in Table 4.2

Description of the parameters			
Description	Symbol	Value	Unit
Pile diameter	D	0.762, 3, 6, 8, 10	m
Forcing frequency	f	23.3, 28.3, 33.3, 38.3, 46.7	Hz
Gear phase shift	φ	0, 1 , 3	°
Embedment depth	L_{em}	$L/10$, $L/3$, $L/2$	m
Stiff and loose soil			
Soil stifness	$k_{s,a}$ and $k_{s,t}$	$[k_{s,a}$, $k_{s,t}]$, $[2k_{s,a}$, $2k_{s,t}]$	N/m^3

Table 4.2: Parametric study variables

Also, with the increasing pile diameter, the length of the pile is also increased. This is done to use realistic pile dimensions. Common offshore pile dimensions are obtained from [46]. From the same study, an estimation for the the wall thickness of the pile is given:

$$h_p = 6.35 + \frac{D}{100} \quad [mm] \tag{4.2}$$

In Table 4.3 below, the corresponding lengths with each pile diameter are given

Monopile dimensions			
Diameter D	Length L	Thickness h_p	Unit
0.762	30	0.0159	m
3	40	0.036	m
6	60	0.067	m
8	70	0.086	m
10	80	0.106	m

Table 4.3: Pile dimensions

Hammer-pile selection

Finally, the hammer selection is based on common vibro-hammers used in specific range of pile diameters [13]. Table 4.4 below summarizes the vibro hammers used for each pile dimension. The specification sheet for each vibro hammer are given in Annex B.

Vibratory Hammer Specification Per Hammer by Pile Diameter						
Diameter D	Hammer type and amount	Eccentric moment [kgm]	Static mass [kg]	Dynamic mass [kg]	Elastomere pads stiffness k_{el} [N/m] and damping c_{el} [Ns/m]	Suppressor housing natural frequencies f_0 and f_1 [Hz]
0.762	1 PVE110M	110	5000	10100	k_{el}, c_{el}	16.1, 38.7
3	1 PVE130M	130	6480	13020	$0.4k_{el}$, $0.4c_{el}$	16.9, 21.3
6	2 PVE500M	500	15000	46420	$2k_{el}$, $2c_{el}$	12.3, 20.0
8	3 PVE500M	500	15000	46420	$3k_{el}$, $3c_{el}$	10.8, 19.8
10	4 PVE500M	500	15000	46420	$4k_{el}$, $4c_{el}$	9.7, 19.6

Table 4.4: Vibratory hammer specifications

The properties of the elastomere pads are as given in Table 4.1 and based on the hammer PVE110M. The damping and stiffness values increase linearly with increasing hammer amount and mass, except in the case of PVE130M. The elastomere pads there are chosen such that the natural frequency of the suppressor house remains constant for all hammer-pile systems.

The natural frequency of the suppressor housing is obtained by modelling the hammer seperatly as a 2DOF system, with the pile assumed as a spring with stiffness $\frac{EA}{L}$. See Figure 4.1 below:
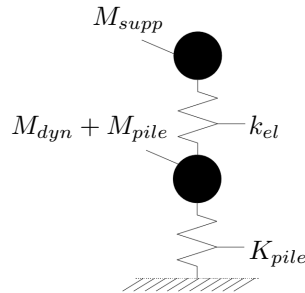

Figure 4.1: Hammer model as 2DOF system

4.2. Context for interpreting results

To provide context for the results presented in each section, first the impact of a properly modelled hammer-pile system with a simplified soil reaction on pile properties will be discussed. This information will be relevant in the subsequent results and discussions.

To accurately predict the natural frequencies of a pile, it is important to consider the pile within the context of the hammer-pile-soil system, as there are several factors that cause the natural frequencies to shift lower, potentially within the vibratory hammer's forcing frequency range. Neglecting the influence of the hammer or soil can result in unrealistically high natural frequency values, particularly for smaller diameter or slender piles, as shown in Figure 4.2 (a).
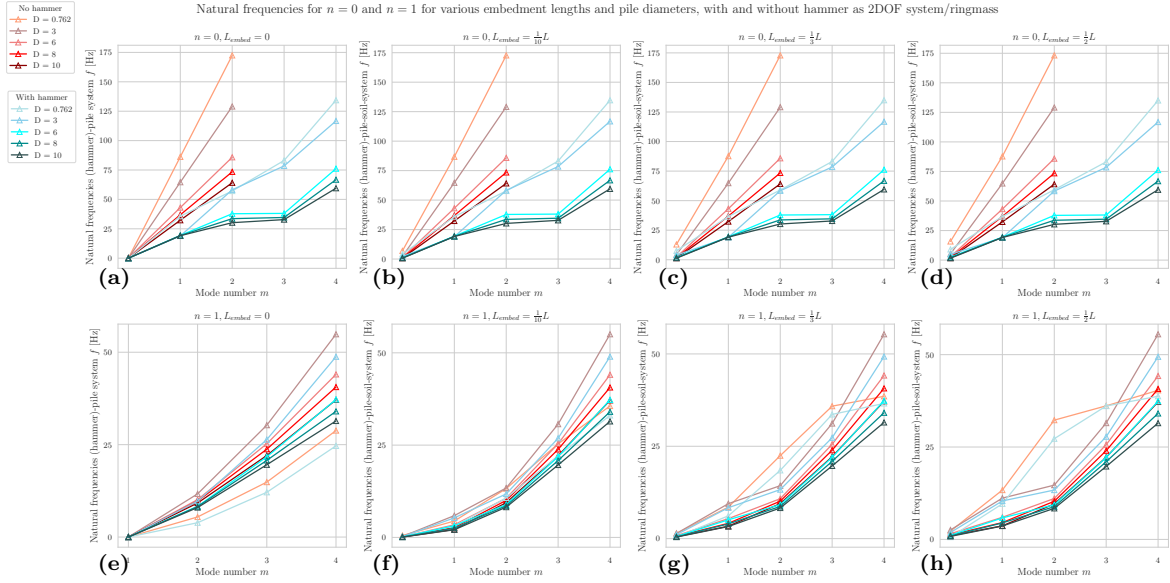

Figure 4.2: Natural frequencies for (a) $n = 0$, pile, with and without hammer as 2DOF system, (b) - (d) $n = 0$, pile-soil-system, with and without hammer as 2DOF system, (e) $n = 1$, pile, with and without hammer as ringmass,(f) - (h) $n = 1$, pile-soil-system, with and without hammer as ringmass

Figure 4.2(a) demonstrates that a pile modeled in isolation, without accounting for the hammer or soil, has a significantly higher natural frequency compared to the same pile modeled with the hammer as a 2DOF system. This is because the hammer adds substantial mass on top of the pile while the stiffness change is negligible. The natural frequency decreases as mass is added while stiffness remains relatively constant. This is especially evident for slender piles, as dropping the natural frequency from approximately 80 Hz to 30 Hz places it within the range of vibratory hammer forcing frequencies.

Moreover, accounting for the soil reveals that at increasing embedment depths, the slender pile with a diameter of 0.762 meters approaches a common forcing frequency of 23.3 Hz in mode 0. This mode is significantly amplified for slender piles compared to its other modes, as shown in Figure 4.4 (a). As seen from Figure 4.2 (e) to (h), the natural frequencies of radial modes up to mode number 4 are always within the driving frequencies, which may lead to resonance behaviour of the system.

When considering only the pile, without the hammer-pile-soil system, increasing the diameter of the pile causes the natural frequencies to shift towards lower values. This is because the mass of the pile increases at a faster rate than its axial stiffness when using typical pile dimensions [46] from practical applications. As the pile diameter increases, the mass of the pile increases at a higher rate than the stiffness of the corresponding pile. Consequently, the ratio of stiffness over mass, becomes smaller and smaller with increasing pile diameters, resulting in decreasing natural frequencies. In addition, the hammer, which adds extra mass and negligible stiffness compared to the stiffness of the pile, further reduces the natural frequencies, bringing them closer to the range of vibratory hammer driving frequencies.

4.3. Force transfer from hammer to pile

In this section, the results of the force transfer from the hammer to the pile will be presented. The aim of this study is to understand the difference between the actual force transferred by the hammer and the assumed force used in practice, and to investigate the significance of accurately modeling not only the hammer but also the pile, particularly for piles with larger diameters. The results of this comparison will be shown for both a circular cylindrical shell model and a simple bar model, both with the hammer modeled as a 2 degree of freedom system on top, and will demonstrate the impact of various parameters such as pile diameter, forcing frequency, and gear misalignment.

The current simplified closed form solutions are simple 1D bar models with the mechanical action from the vibratory hammer assumed as a force on top of the pile. This model assumes that the nominal force produced by the rotating eccentric masses $me\omega^2$ is completely transferred to the pile, which is by far not the case in practice [11].

The figures in Figure 4.3 (a) to (e) depict the amplitudes of the external applied force $\hat{F}_{me\omega^2}$ and the amplitudes of the internal forces $\hat{N}_z$ developed at the pile top, for different forcing frequencies and eccentric mass misalignments $\varphi = 0°, 1°$, and $3°$. For clarification, the amplitudes are obtained from the first pile node, which is the second node in the hammer-pile-soil system. Additionally, the figures include the natural frequencies $\omega_i^{n=0}$ of the hammer-pile-soil system. Figure 4.3 (f) shows a consolidated view of the force ratio for different diameters and forcing frequencies, making it easy to compare the effect of diameter and forcing frequency on force transfer. Both amplitudes are taken from the first pile node.

Table 4.5 presents the first five natural frequencies and the properties of each pile presented in Figure 4.3.

Pile properties and corresponding natural frequencies for the axisymmetric mode $n = 0$ for the Hammer-Pile-Soil system					
Diameter D [m]	0.762	3	6	8	10
Length L [m]	30	40	60	70	80
Wall thickness t [m]	0.0159	0.036	0.067	0.086	0.106
ω_0 [Hz]	7.5	3.9	2.0	1.6	1.3
ω_1 [Hz]	36.5	18.9	19.4	19.2	19.1
ω_2 [Hz]	59.0	58.3	37.8	33.7	30.2
ω_3 [Hz]	83.1	78.4	38.2	34.6	32.8
ω_4 [Hz]	135.0	116.8	76.2	66.8	59.5

Table 4.5: Properties of the piles presented in Figure 4.3

It can be seen from Figures 4.3 (a) to (e) that the misalignment has a minimal impact on the decrease in amplitude. When analyzing the data from these figures, it is found that the decrease in amplitude caused by the misalignment is on average 0.01%. As a result, in the subsequent analysis in this section, only the case without misalignment will be considered.
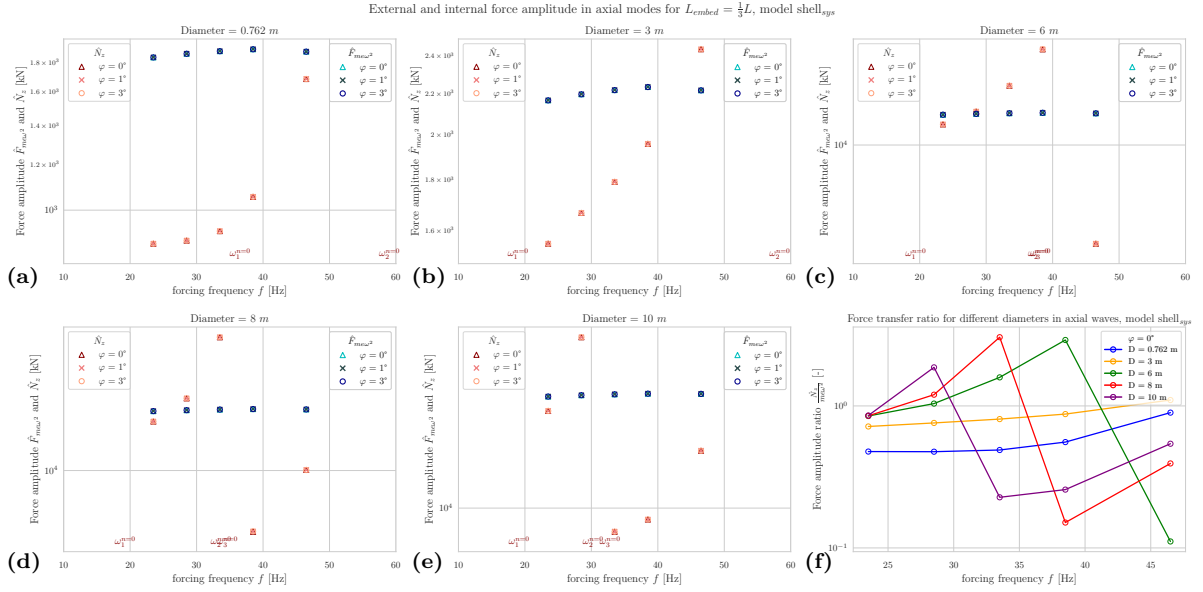
Figure 4.3: External applied force amplitude $\hat{F}_{me\omega^2}$ and internal force $\hat{N}_z$ for various diameters, forcing frequencies and gear misalignment for model shell$_{sys}$. Embedment depth $\frac{L}{3}$

The ratio of force transfer, represented by $\frac{\hat{N}_z}{\hat{F}_{me\omega^2}}$, for a slender pile with a diameter of 0.762m varies between 0.48 and 0.88 as the frequency of the force increases. In figure (b), a peak is observed at the highest forcing frequency, where the force transfer ratio exceeds 1. As the pile diameter increases up to figure (e), the observed amplification of the internal force $\hat{N}_z$ shifts towards lower frequencies on the horizontal axis. In Figure (f), it can be seen that, overall, the force transfer ratio is lowest for the smallest diameter at lower forcing frequencies and increases as the diameter also increases. However, there is a disruption in this trend in the mid-range frequencies, and the trend repeats at the higher forcing frequencies, but with a distinction between the two smallest diameter piles and the three largest diameter piles. The two smallest piles do not experience large amplifications like the three largest diameter piles. The three largest diameter piles have the smallest force transfer ratio for diameter D = 6 and increases as the diameter increases up to 10m. For the two small diameter piles, this trend remains unchanged throughout the forcing frequencies.

The findings from the analysis of the force transfer ratio will be compared to those of prior investigations [11]. As mentioned earlier, a previous study [11], which was reviewed in Chapter 2, provided an analytical solution for the force transfer ratio at the pile top ($z = 0$) in a free toe scenario. This solution, which is expressed by eq. 4.3, characterizes the proportion of force transmitted from the vibrator to the pile during vibratory driving and is derived by solving the 1D wave equation (eq. 2.1) while treating the hammer as a rigid mass at the top boundary.

$$\eta_{F,pile}(z = 0) = \frac{1}{1 + \frac{\mu\alpha}{\tan(\alpha)}} \tag{4.3}$$

in which μ is the mass ratio $\frac{M_{vib,dyn}}{M_{pile}}$ of the mass of the dynamic part of the vibrator $M_{vib,dyn}$ and the pile mass M_{pile} and α is the pile relative wave length $\frac{2\pi L}{\lambda}$. The wavelength λ is further defined in eq. 3.10, and is dependent on the frequency of interest, which in this case is the forcing frequency f.

Figure 4.3 illustrates the amount of force transferred from the hammer to the pile. It is apparent that the transfer of force is significantly lower than the external force calculated using the eccentrics, with the exception of a few peak values that are present.

Figure 4.3 (a) shows that the internal force remains below the external force for the full range of forcing frequencies, between 0.48 and 0.88. A peak is observed at the highest forcing frequency, which,

according to that figure, is located between ω_1 and ω_2, which are the second and third natural frequencies of the hammer-pile-soil system. When looking at D = 3 in Figure 4.3 (b), a peak in internal force is observed at the highest forcing frequency, where the internal force surpasses the external applied force. This behaviour repeats it self for all the diameters, except with increasing diameter the peak amplitude shifts one frequency each time towards the lower frequencies. The natural frequencies of each case are given in the same figure. From there it can be seen as the pile diameter increases, the natural frequencies of the pile decrease, with the natural frequencies that fit within the limits of the horizontal axis being included in the figures, which are in these cases ω_1 up to ω_3 and moving towards lower frequencies on the horizontal axis. The peaks in the force transfer ratio for the remaining pile diameters follow this shift in natural frequencies. This pattern persists as the pile diameter continues to increase and the natural frequencies of the pile decrease, causing an amplification in the response in lower frequencies. However, looking at ω_1 in each graph, it looks like it has no effect on the internal force, even though it is very close to a forcing frequency.

As shown in Figure 4.3 (a), the internal force remains below the external force throughout the entire range of forcing frequencies between 0.48 and 0.88. A peak is observed at the highest forcing frequency, which, based on the figure, is located between the second and third natural frequencies (ω_2 and ω_3) of the hammer-pile-soil system. Figure 4.3 (b) displays the same behavior for D = 3, with an internal force peak at the highest forcing frequency exceeding the external applied force. This trend persists across all diameters, with each peak amplitude shifting one frequency towards lower frequencies as the diameter increases. The natural frequencies for each diameter are provided in the same figure, with the natural frequencies that fall within the limits of the horizontal axis included in the figures (in these cases, ω_1 through ω_3 and shifting towards lower frequencies). As the pile diameter increases and its natural frequencies decrease, there is a corresponding increase in the response amplification at lower frequencies. However, it appears that ω_1 has no impact on the internal force, despite being close to a forcing frequency, as observed in each graph.

This behaviour can be explained by looking at the natural frequencies, mode shapes and modal amplitudes of the hammer-pile-soil system.
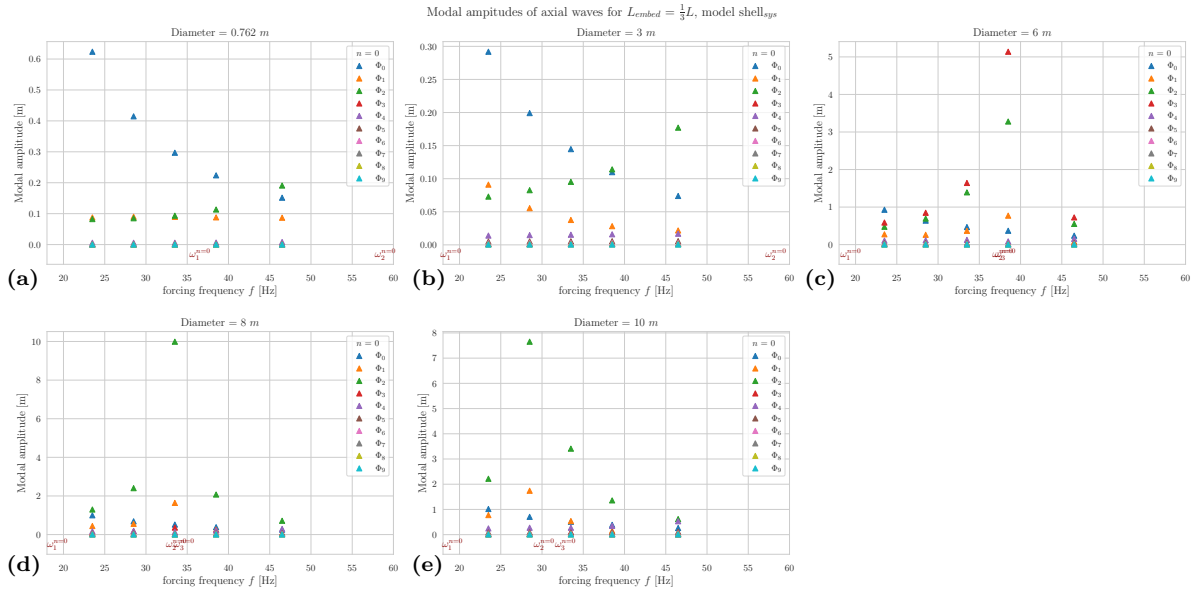
Figure 4.4: Modal amplitudes of the first ten axisymmetric modes, $L_{embed} = \dfrac{L}{3}$

From examining Figure 4.4 (a), it is apparent that ϕ_0 is greatly amplified. Nevertheless, upon examining the zeroth mode shape factor depicted in Figure 4.5 (a), it becomes evident that this corresponding mode constitutes a rigid body motion with negligible difference between the first and second nodes of the pile (which are the second and third nodes of the complete hammer-pile-soil system). As

such, this mode has no effect on the internal force, as rigid body motions do not affect internal forces because they do not exhibit elastic properties. The amplitudes of mode 1 and mode 2 increase as the forcing frequency increases. Mode 1 is the dominant mode in the suppressor motion, exhibiting elastic behavior, while mode 2, which has the highest modal amplitude at the highest forcing frequency, also has a larger strain. This explains the amplification of the internal force near the higher forcing frequencies.

The pile with a diameter of 3m, as shown in Figure 4.3 (b), exhibits a pattern in which the first and second modes, ϕ_0 and ϕ_1, are rigid body modes. This means that they have a minimal impact on the internal force despite having high amplitudes. However, the third mode, ϕ_2, displays elastic behavior and has a greater amplitude, which explains the internal force following the trend of the modal amplitude of this mode.
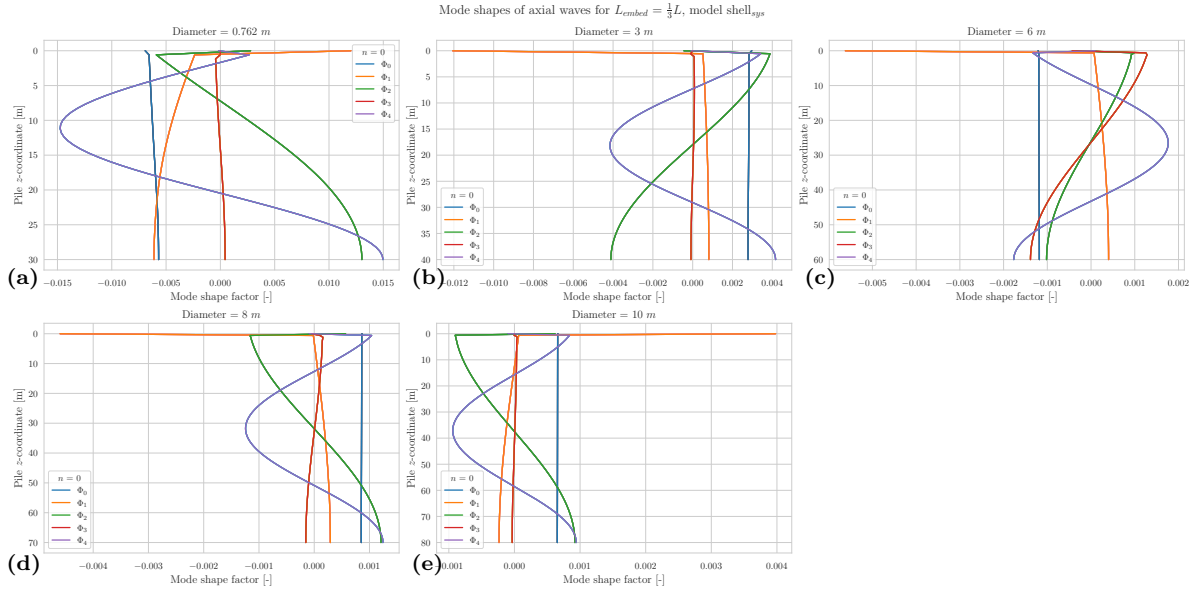

Figure 4.5: Mode shapes of first five axisymmetric modes, $L_{embed} = \dfrac{L}{3}$

In overall, it can be observed that the force transfer ratio for smaller diameter piles is lower than for larger diameter piles, as shown in Figure 4.6. This graph also includes the force transfer ratio η from the study referenced in [11] for comparison.

One explanation for this is that the force transfer ratio is heavily influenced by the hammer-pile mass ratio μ, as stated in [11] and demonstrated in equation 4.3. As the mass ratio increases, the force transfer ratio decreases. This is often the case for small diameter piles, as the mass of the vibratory hammer can be proportionally larger than the total pile mass, leading to a smaller force transfer ratio. This trend can also be seen in the Figure 4.6
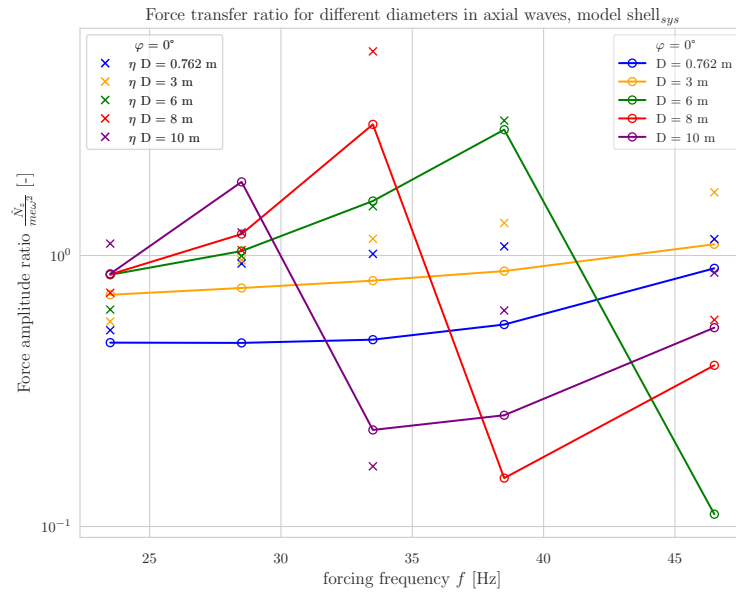
Figure 4.6: Force transfer ratio including the ratio η obtained from [11]

The peaks in the graph indicate high levels of strain at specific frequencies for the three large diameter piles. After the drop, the trend of small diameter piles having the lowest force transfer ratio remains consistent when looking at the 3 large diameter piles. Additionally, by observing the trend of shifting natural frequencies and noting that the pile with a diameter of 3m exceeds unity at the highest frequency, it can be predicted that the slender pile with a diameter of 0.762m will exceed unity at a slightly higher forcing frequency. This prediction is supported by the graph, which shows that the force transfer ratio for D = 0.762m is increasing towards the end.

In general, when designing for small diameter piles, it's important to consider the potential for a small force transfer ratio. For larger diameter piles, it's important to anticipate potential high levels of strain within the typical driving frequencies and expect to see a higher force transfer ratio at lower forcing frequencies and a lower force transfer ratio at higher forcing frequencies.

Effect of embedment depth and soil stiffness
Figure 4.7a demonstrates that, the force transfer ratio is unaffected by the embedment depth, with the exception of the small diameter pile at higher forcing frequencies. However, if the soil stiffness is increased to a higher range, as shown in Figure 4.7b, the force transfer ratio values are influenced by the embedment depth. Despite this, the overall trend remains the same, except for the small diameter pile, which exhibits the opposite trend compared to looser soil, with greater influence observed in the lower forcing frequency range in stiffer soils. For all other diameters, and when resonance effects are disregarded, a higher force transfer ratio is generally observed with increasing embedment depth in stiffer soils.
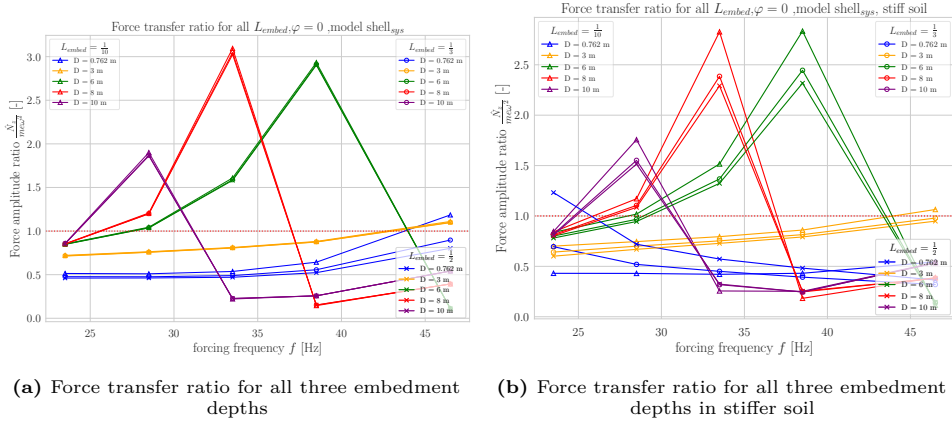
(a) Force transfer ratio for all three embedment depths

(b) Force transfer ratio for all three embedment depths in stiffer soil

Figure 4.7: The effect of embedment depth and soil stiffness on the force transfer ratio in **(a)** looser soil and **(b)** stiffer soil

It is observed from Figure 4.7a that the impact of the embedment depth on the pile response is limited to small diameter piles in looser soil. In Figure 4.7b, as the soil stiffness increases, larger diameter piles are also affected. This can be attributed to the relative stiffness of the soil and the pile. When the pile diameter increases, its stiffness becomes so high that the addition of looser soil doesn't significantly affect its response. However, with small diameter piles, the soil stiffness relative to the pile is not much different, so the addition of soil stiffness can modify the pile properties and lead to a noticeable effect on the pile response.

4.4. Activation of elastomer pads

In this section, the relative motion of the suppressor housing and the pile during vibratory pile driving is studied. The motion of the suppressor housing and the pile is analyzed for different forcing frequencies and pile diameters. By comparing the motion of the suppressor housing to the motion of the pile, the effect of the properties of the pile and the forcing frequency on the isolation of the vibrations from the excitation block to the crane is determined. Additionally, the effect of the embedment depth on the relative motion of the suppressor housing and the pile is also investigated. The properties of the pile and hammer are as given in Tables 4.4 and 4.1.

4.4.1. Effect of misalignment, forcing frequency and pile diameter

In Figure 4.8 below, the displacement amplitudes of the suppressor and first pile node are represented by $\hat{U}_{supp}$ and $\hat{U}_{pile}$ respectively. For clarity, the amplitudes for the suppressor housing are obtained from the first node, and for the pile from the second node of the whole hammer-pile-soil system. The graph, from (a) to (e), illustrates the displacement amplitude for different pile diameters, and each graph shows the impact of three different phase-shifts φ. In Figure 4.8 (f), the relative motion between the pile and suppressor for the different diameters and forcing frequencies is presented in a consolidated view, allowing for easy comparison of the effect of diameter and frequency on the motion. It's noteworthy that the pile motion includes the motion of the excitation block, as the excitation block is rigidly connected to the pile.
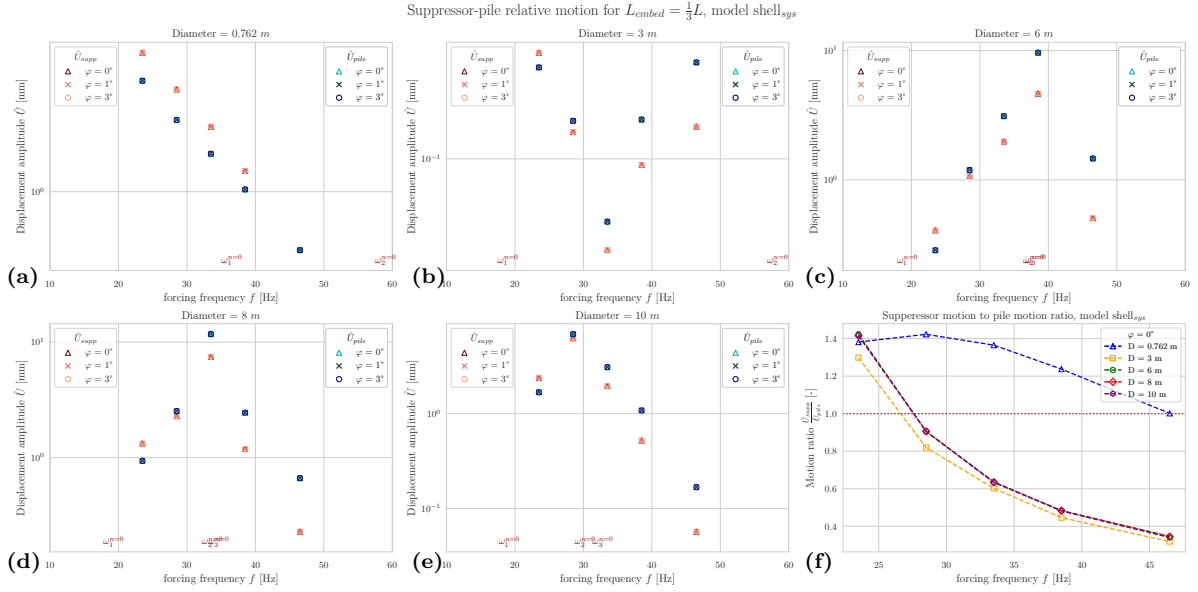
Figure 4.8: Relative suppressor pile motion for various diameters, forcing frequencies and gear misalignment for model $shell_{sys}$. Embedment depth $\frac{L}{3}$

From Figures 4.8 (a) to (e) it is observed that the misalignment has minimum effect on the amplitude decrease relative to eachother. When extracting the data from these graphs, the decrease in amplitude due to the misalignment is on average 0.01%. Therefore, in the further analysis in this section, only the case without misalignment will be considered.

In Figure 4.8 (f) which displays all the graphs combined, it can be observed that as the frequency increases, the relative motion between the suppressor and pile decreases. At the lowest forcing frequency, the relative motion for all diameters starts above 1, indicating that the suppressor motion is excited greater than the pile motion. As the frequency increases, the relative motion for the D = 3 to D = 10 m decreases at a faster rate than for the slender pile with D = 0.762. In fact, the relative motion between the suppressor and pile for the slender pile is always greater than 1, only becoming equal at the highest frequency and never crossing the unity line. However, for the larger diameter piles, the relative motion falls below 1 from the second forcing frequency and beyond and decreases until a ratio of approximately 0.35.

The activation of the isolator springs (elastomere pads) in the vibratory hammer can be different for different forcing frequencies. The relative motion of the suppressor housing to the first pile node is strongly dependent on the design of these elastomere pads. In Figure 4.9 (a) below, the relative motion is given for the misalignment of $\varphi = 0°$. As mentioned before in section 4.4 none of the misalignment degrees have impact on these results.

The effectiveness of the elastomere pads can be compromised if the pile mass is too small. This is because the mass of the pile, together with the stiffness of the pads, contributes to the natural frequency of the hammer system. If the pile mass is below the minimum mass threshold for which the pads were designed, the natural frequency of the hammer system may increase, potentially bringing it closer to the operating frequency. This can result in higher transmission of vibration from the pile to the crane, which undermines the ability of the elastomere pads to isolate the vibrations. To address this issue, it may be necessary to increase the driving frequency to move away from the natural frequency.

In addition, the analysis of the stiffness of the elastomere pads has been limited to the scope of the thesis. Generally, these pads are designed with low stiffness to achieve a low natural frequency for the hammer system. While this is true for the first natural frequency, the low stiffness has little impact on the second natural frequency, as shown in Table 4.6. For commonly used pile dimensions, the second natural frequency approaches the driving frequencies of the vibratory hammer. The axisymmetric

mode shapes in Figure 4.5 indicate that the mode corresponding to this natural frequency (mode ϕ_1) dominates the suppressor motion. Furthermore, a lighter pile mass, such as in small diameter piles, can exacerbate the situation by increasing the natural frequency even further. Only with significantly larger pile masses can both the first and second natural frequencies remain low, as to be seen in the last column of Table 4.6, but achieving this is impractical as pile wall thicknesses are typically designed to be as thin and lightweight as possible. It is important to note that the pile dimensions used in this study are commonly used in practice and cannot achieve the goal of lowering both natural frequencies to a level far outside the range of driving frequencies. The results shown in Table 4.6 indicate that achieving this goal would require pile weights that are ten times greater than those currently used in practice. However, this is unrealistic because the trend is to use lighter pile weights for optimal material usage.

System natural frequencies with different elastomer stiffness k_{el} and pile mass M_p						
	$1 \cdot k_{el}$, $1 \cdot M_p$		$0.01 \cdot k_{el}$, $1 \cdot M_p$		$0.01 \cdot k_{el}$, $10 \cdot M_p$	
Diameter D [m]	f_0	f_1	f_0	f_1	f_0	f_1
0.762	16.1	38.7	3.3	18.8	3.3	8.3
3	16.9	21.3	1.9	19.4	1.9	6.5
6	12.3	20.0	1.9	12.7	1.9	4.3
8	10.8	19.8	1.9	11.1	1.9	3.7
10	9.7	19.6	1.9	9.9	1.9	3.2

Table 4.6: System natural frequencies (Hz) with changing elastomere stiffness and pile mass

This can explain the behaviour that is observed in Figure 4.8 (f), where in the smallest pile, the suppressor motion is relatively higher than the pile motion, meaning poor spring activation. This is due to the natural frequency of the system being closer to the forcing frequencies, resulting in higher motion of suppressor, thus poor activation of isolator springs. The larger piles show strong activation of the springs in higher forcing frequency range.

In Figure 4.9 (a), the system natural frequencies are given along with the relative motion between suppressor and pile head and Figure 4.9 (b) the hammer-pile mass ratio.
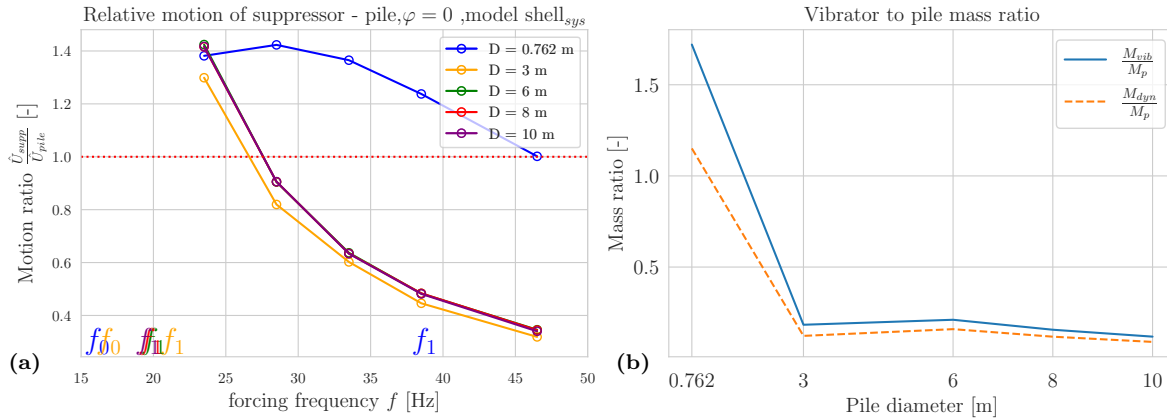

Figure 4.9: (a) Suppressor-pile relative motion for $L_{embed} = \dfrac{L}{3}$, $\varphi = 0$, model shell$_{sys}$,including vibrator natural frequencies f_0 and f_1, (b) Vibrator to pile mass ratio with and without the suppressor housing

The relative motion of the suppressor and slender pile with D = 0.762 m remains above unity at all forcing frequencies. This can be explained by the fact that the natural frequency of the hammer-pile system is within the range of forcing frequencies, which makes it prone to excitation within these frequencies.

As depicted in Figure 4.9 (b), the vibrator-pile mass ratio is notably greater for the smaller pile compared to the larger diameter piles. This is reflective of real-world scenarios and may impact the relative motion. In practice, reducing the ratio by employing a lighter vibratory hammer would worsen the problem with regards to natural frequencies, and is not a realistic solution.

In general it can be said that in the range of higher forcing frequencies, the isolator springs are activated more, since it moves further away from the natural frequencies of the hammer system.

For the small diameter piles, it has to be taken into account that the lower mass of the pile can influence the activation of the isolator springs because it will increase the natural frequency of the complete system. If that happens, it might end up in the range of driving frequencies, and the suppressor motion can therefore remain amplified, as to be seen in Figure 4.9

In the next chapter, factors that need to be taken into account will be given, based on the observation that the efficacy of the elastomere pads may be reduced when the natural frequency of the vibration system is in close proximity to the forcing frequency.

4.4.2. Effect of embedment depth

Figure 4.8 has been constructed for all three embedment depths, to give an insight in the effect of the embedment depth on the activation of the isolation springs in the vibratory hammer. The results of the three different embedment depths are combined in a single graph for looser soil in Figure 4.10a and stiffer soil in Figure 4.10b.
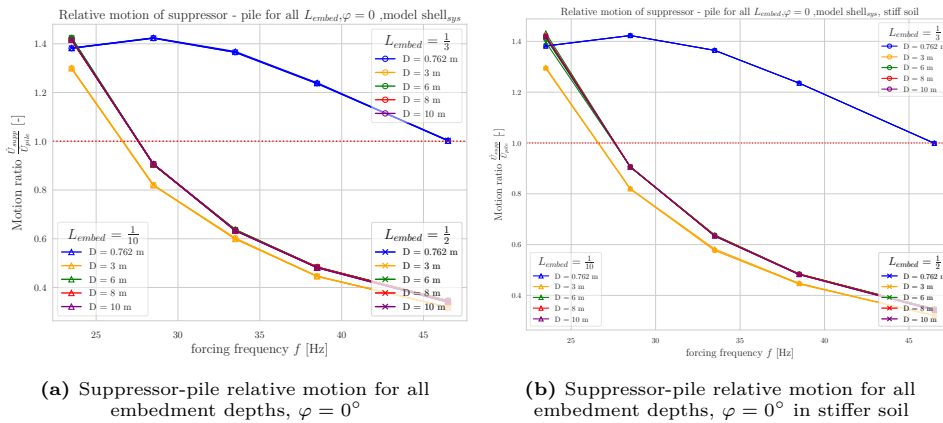

(a) Suppressor-pile relative motion for all embedment depths, $\varphi = 0°$

(b) Suppressor-pile relative motion for all embedment depths, $\varphi = 0°$ in stiffer soil

Figure 4.10: The effect of embedment depth and soil stiffness on the relative motion of suppressor housing and pile head in **(a)** looser soil and **(b)** stiffer soil

According to Figure 4.10, the suppressor and pile head exhibit a consistent relative motion regardless of the depth at which the pile is embedded. The negligible effect of embedment depth on the relative motion between suppressor and pile head remains unchanged even as the soil stiffness increases. This is because the absolute values for suppressor housing and pile head are affected in the same way by increasing soil stiffness due to the linearity of the system. From Figure 4.4 and B.24 it can be seen that the modal amplitudes remain unaffected, while the relative values of the modal shapes remain the same for mode ϕ_1 where the suppressor motion is very dominant.

4.5. Effect of misalignment

In this section, the primary focus is to study the impact of misalignment on power consumption by bending vibrations and the extent of bending-like motion (lateral pile motion described by $n = 1$) it contributes to. The study will compare the power absorbed by the pile with misalignment and without misalignment. Additionally, it will evaluate how misalignment affects the energy transfer between the vibratory hammer and the pile by examining the contribution of misalignment to bending-like motion.

The findings of this analysis will give a deeper understanding of the influence of misalignment on the energy transfer.

4.5.1. Power consumption

Single gear misalignment

The graphs in Figure 4.11 (a)- (e) illustrate the power amplitudes in the axial and lateral direction, represented by $\hat{P}_u$ and $\hat{P}_w$ respectively, for different pile diameters. Each graph shows the impact of three different phase-shifts $\varphi = 0°, 1°$ and $3°$, except for the bending-like motion where zero phase shift does not produce any force. Additionally, the graphs include the natural frequencies for both cases, where $n = 0$ is represented in red and $n = 1$ is represented in blue. As the external force is applied only to the corresponding first degree of freedom, the results in the graph are obtained solely from the node of that degree of freedom. Figure 4.11 (f) presents a consolidated view of the power consumed for bending vibrations described by $n = 1$ for different diameters and forcing frequencies, making it easy to compare the effect of diameter and forcing frequency on power consumption.
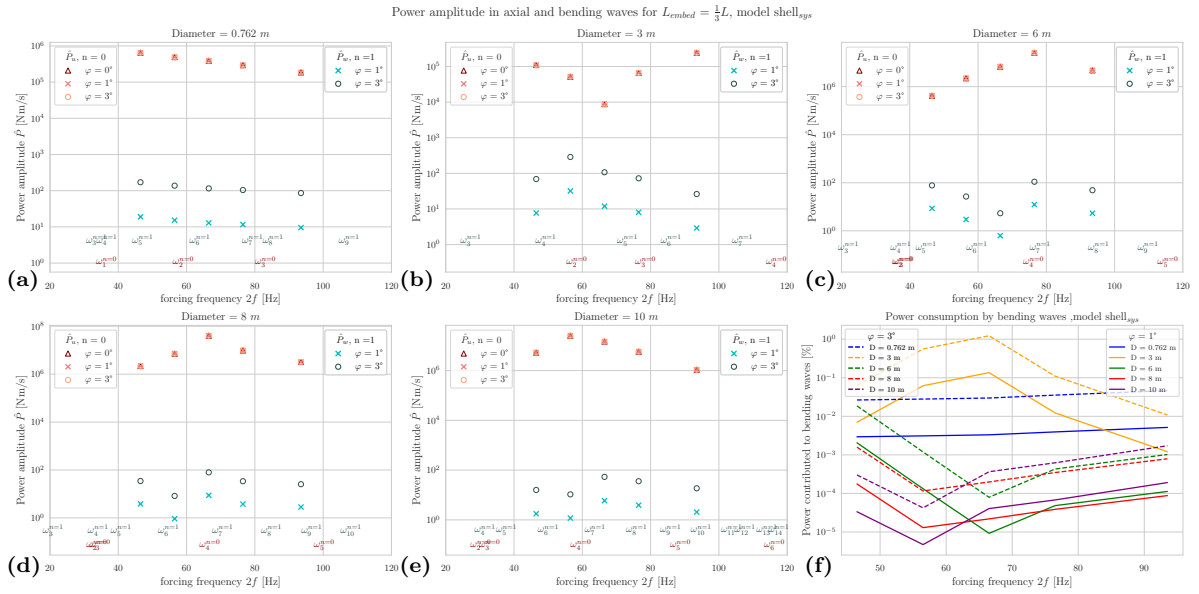

Figure 4.11: Power consumption in axisymmetric ($n = 0$) and bending-like vibrations ($n = 1$) for various diameters, forcing frequencies and gear misalignment for model shell$_{sys}$. Embedment depth $\frac{L}{3}$

Figures 4.11 (a) to (e) show that there is no change in power consumption when there is a phase shift in axisymmetric (axial response in $n = 0$) vibrations compared to when there is no phase shift, regardless of the diameter or forcing frequency. This is because the change in axial force amplitude remains negligible with a phase shift (misalignment) in a gear.

However, for the radial vibrations, the power amplitude does exhibit a more pronounced difference with increasing eccentric mass misalignment, as the phase shift increases from 1°to 3°. The variations in power amplitude for bending-like motions for the increasing degree of misalignment are presented in Annex B,Figure B.11. As shown in this figure, the difference in power amplitude between the two different misalignment degrees remains relatively constant at approximately 9 times, regardless of the variations in forcing frequency and pile diameter.

Upon analyzing Figure 4.11 (f), which displays the power consumption for bending vibrations at various diameters and frequencies, it is evident that the energy needed to produce bending vibrations is significantly lower than that required for axisymmetric vibrations. Considering that the power consumed by axisymmetric vibrations is 100% of the total power utilized for driving, the proportion of power consumed by bending vibrations for a slender pile with a diameter of 0.762m ranges from 0.025% to 0.045% as the forcing frequency increases. With increasing pile diameters, these values decrease even more, reaching as low as 10e-06%. Except for the pile with diameter of 3 meter, which shows an

opposite and distinct trend, the maximum power consumed by bending vibrations is approximately 1.3 % at a forcing frequency of 33.3 Hz, and lower at neighbouring frequencies. When examining the power consumption of bending vibrations for larger diameter piles (D = 6 to 10 m), it is apparent that as the diameter increases, the power consumed by bending vibrations decreases in the lower range of forcing frequencies. However, in the higher range of forcing frequencies, this trend is inverted, with the power consumed by bending vibrations increasing as the diameter increases.

This is because the natural frequencies of both axisymmetric and bending-like modes shift towards lower values as pile diameter increases. Specifically, the bending-like mode ϕ_3 is excited the most by lower driving frequencies and its modal amplitude decreases as pile diameter increases, as illustrated in Figure B.21 in Annex B. As a result, at low forcing frequencies, the natural frequency of the smallest diameter pile is closer to the forcing frequency than the natural frequency of the larger diameter piles. Consequently, the smallest diameter pile (6m) experiences more bending-like motions in the lower frequency region and requiring more power. However, as the diameter increases, the smaller natural frequencies move further away from the range of driving frequencies, and therefore the amplitude decreases in the lower frequency region. At the same time, as the diameter increases, the higher natural frequencies (modes ϕ_4 and ϕ_5) shift into the range of driving frequencies from the highest side, allowing the larger diameter piles to resonate more efficiently in the higher frequency range, requiring more power.

Generally, the impact of misalignments reduces with increasing diameter. This is due to the fact that, initially, the analysis was conducted on a single misaligned gear. As the pile diameter increases, the number of gears also increases, and a single gear misalignment becomes a much smaller proportion of the total gears compared to a hammer with larger amount of gears. To ensure a fair comparison, the number of misaligned gears will be increased for all cases up to 25% and 50% of the total number of gears per hammer.

Effect of embedment depth and soil stiffness
Figure 4.12a shows that changes in embedment depth have little effect on the power consumption by bending-like motion. However, Figure 4.12b demonstrates that soil stiffness can influence the power consumption by radial vibrations, with shallower embedment depths resulting in greater power consumption for the two smallest diameter piles across all driving frequencies. This observation is consistent with the fact that shallower embedment depths provide less radial restriction, allowing for greater displacement and ultimately resulting in higher power consumption than deeper embedment depths.

Moreover, as mentioned previously, the relative stiffness between the soil and the small diameter piles is much smaller than the relative stiffness between soil and large diameter piles. Therefore, local changes in stiffness due to changing embedment depths can have a greater impact on the smaller diameter piles, making them more susceptible to the effects of embedment depth and soil stiffness.
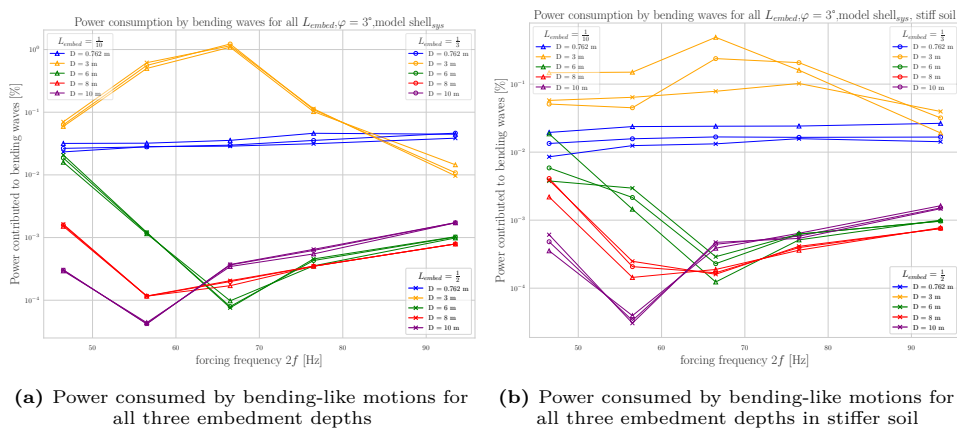

(a) Power consumed by bending-like motions for all three embedment depths

(b) Power consumed by bending-like motions for all three embedment depths in stiffer soil

Figure 4.12: The effect of embedment depth and soil stiffness on the power consumption by bending-like motions in **(a)** looser soil and **(b)** stiffer soil

The influence of embedment depth on the power consumption by bending-like motions for large diameter piles (>6m) is limited to stiffer soils and only affects the low driving frequency range (<33 Hz).

As illustrated in Figure B.20 and B.24, changes in soil stiffness have little effect on the axisymmetric modal amplitudes, while the radial modal amplitudes shown in B.21 and B.25 are only affected at lower frequencies. As a result, larger diameter piles are primarily impacted by soil stiffness in the low driving frequency range, whereas higher frequency ranges remain largely unaffected by.

As demonstrated by the results discussed above, a single gear misalignment has minimal effect on power consumption by bending-like motions when compared to axisymmetric vibrations. This is primarily due to the lower bending stiffness relative to axial stiffness, but also because the horizontal force resulting from a gear misalignment of 1° - 3° remains relatively small compared to the vertical load. This effect is particularly pronounced for larger diameter piles, where the single gear misalignment constitutes a small proportion of the total number of gears.

Increased amount of misaligned gears
The results presented above are based on a single gear misalignment, regardless of the number of vibratory hammers and the total number of rotating eccentric masses. In the following section, the results for cases where the misaligned gears comprise 25% and 50% of the total number of gears will be presented in order to determine a range and the upper limit for worst-case scenarios. This upper limit will be reached if the effect of bending-like motions is 10% of higher relative to the axisymmetric vibrations, for both power consumption and displacement ratio.

25% misaligned gears
In Figure B.7, the percentage of misaligned gears is increased from one gear to 25% of the total gears. Each graph in the figure depicts the power consumed by the bending-like motions on the y-axis for different forcing frequencies, with the proportion of misaligned gears on the x-axis, starting at a single gear misalignment. It is important to note that the graphs do not begin at the same point on the horizontal axis because the different diameter piles have varying amounts of total rotating masses and one gear represents a different proportion of these masses for each pile. For example, for a pile diameter of D = 6, the graph starts at $\frac{1}{24}$ on the horizontal axis because one hammer has 12 rotating masses and two hammers are needed to drive this pile, as specified in Table 4.4. Furthermore, the first two pile diameters D = 0.762 and D = 3 are only available as a single point on the graphs since according to Table 4.4, the hammer that those piles are driven with already consist of only 4 gears, which makes a single gear misalignment already 25% of the total gears.
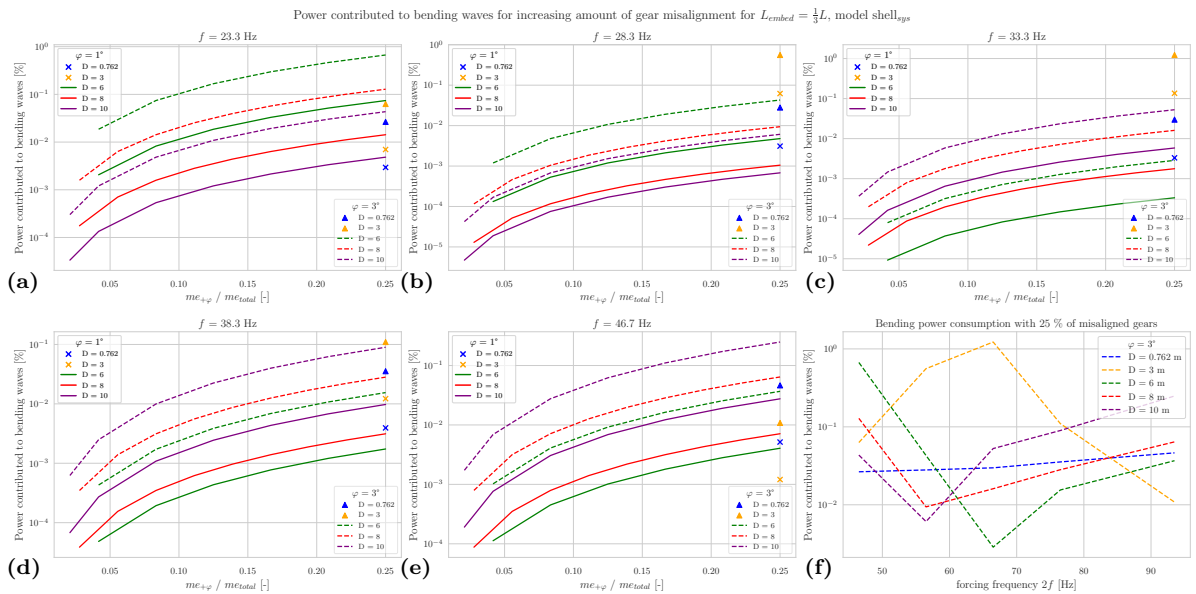

Figure 4.13: Power consumption by bending-like motions for various diameters, forcing frequencies and gear misalignment in case of 25% of misaligned gears for model shell$_{sys}$. Embedment depth $\frac{L}{3}$

When looking at the largest phase shift of $\varphi = 3°$, it is clear that the power contribution for the three largest diameters increases substantially, with an increase equivalent to two orders of magnitude. Additionally, when reviewing Figure B.7, it is apparent that the smaller diameter of D = 6 experiences the highest increase in power contribution in the lower frequency range, while the larger diameter sees the highest increase in the higher frequency range. Despite these increases, it is worth noting that the overall power contribution to bending-like motions remains below 1%, with the highest contribution being equal to 0.66%. Furthermore, the power contribution for the two smallest diameters remains unchanged, as the single gear misalignment is already 25% of the total gears in those vibratory hammers.

50% misaligned gears
Increasing the the proportion of misaligned gears to 50% increases the power consumed by bending-like motions by a factor of 4, with the highest contribution being equal to 4.8 %. The detailed results and figures of this analysis are provided in the Annex B Figure B.9 of the report.

Based on the results presented above, it can be said that a misalignment of 1-3 degrees has a negligible effect on power consumption for bending-like motions. However, for a gear misalignment of 25%, the power contribution to bending-like motion increases substantially for the larger diameters, although the overall contribution remains relatively low.

4.5.2. Bending-like displacement contribution
Single gear misalignment
Performing the same analysis for the bending-like displacement contribution results in Figure 4.14 below. Herein, the axisymmetric (axial) and bending-like displacement amplitudes are represented by $\hat{U}$ and $\hat{W}$ respectively, for various pile diameters and misalignment phase-shifts φ. The displacement amplitudes are all taken from the first pile node. Furthermore, the natural frequencies for both cases are included in the graphs, where $n = 0$ is represented in red and $n = 1$ is represented in blue.
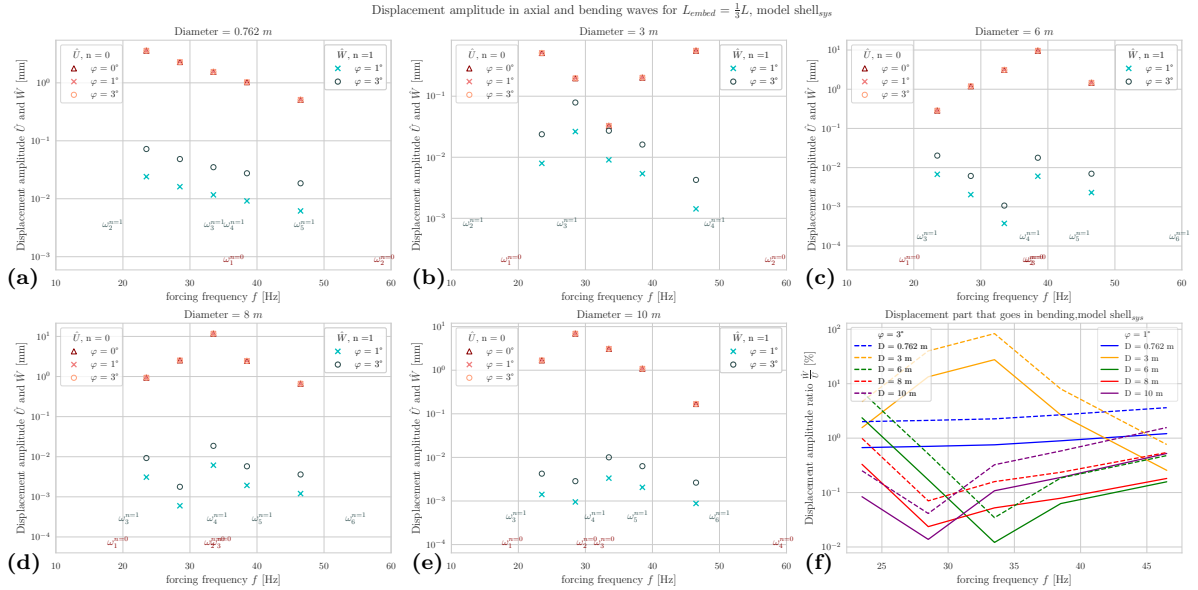

Figure 4.14: Displacement ratio in axisymmetric (axial) and bending-like motion for various diameters, forcing frequencies and gear misalignment for model shell$_{sys}$. Embedment depth $\frac{L}{3}$

When reviewing Figure 4.14 (a) to (e), it is clear that the misalignment has little to no effect on the axisymmetric deformation. However, the bending-like displacement does see an increase, with a factor of 3, as the misalignment angle increases from 1 degree to 3 degrees. It is observed that this increase by a factor of 3 remains consistent throughout all the diameters and forcing frequencies, as shown in Annex B, Figure B.16.

As shown in Figure 4.14 (a), for the most slender pile, there is a clear decrease in amplitude as the forcing frequency increases for both axisymmetric and bending-like deformations. This trend is not

consistent across all pile diameters, as the pile with a diameter of 3m shows a dip in the axisymmetric amplitudes and a peak in the bending-like amplitudes. Piles with diameters between 6m and 10m display a single peak in the axisymmetric displacement amplitudes and two peaks in the bending-like displacement amplitudes.

In Figure 4.14 (f), the amplitude ratios for bending-like deformation relative to axisymmetric deformation for all diameters and forcing frequencies is presented. The bending-like displacement of the slender pile with a diameter of 0.762m ranges from 2% to 3.7% relative to the axisymmetric deformation as the forcing frequency increases for a misalignment angle of 3 degrees. On the other hand, the pile with a diameter of 6m starts at 7% of bending-like deformation for the lowest forcing frequency and decreases to 0.5% at the highest frequency. Similar trend is seen for diameters 8m and 10m, but with a decreasing amplitude ratio for increasing pile diameters. The pile with 3m diameter shows a unique and opposite behavior, it starts around 4.3% of bending-like deformation at the lowest forcing frequency range, increases up to 83% of the axisymmetric deformation at the 33.3 Hz range of forcing frequency and then drops back to 0.8% for the highest forcing frequency. These observations are for a phase shift of $\varphi = 3°$, and for the misalignment of $\varphi = 1°$, these values can be divided by three, as previously mentioned in the text.

Effect of embedment depth and soil stiffness
The contribution to bending-like displacement due to a misalignment has the same trend as the power consumption by bending-like vibrations. The embedment depth has little to no effect on changing of contribution to bending-like displacement. For stiffer soil, also similar trend as power consumption, with larger diameter piles (> 6m) less affected in higher forcing frequencies and smaller diameter piles are affected along all forcing frequencies. See Figure B.17 in Annex B.

Increased amount of misaligned gears
The same way as done for the power contributed to bending-like motions in Section 4.5.1, in this section, the effect of increasing the proportion of misaligned gears to the total gears up to 25 and 50% will be analyzed.

25% misaligned gears
In Figure B.12, the percentage of misaligned gears is increased from one gear to 25% of the total gears. Each graph in the figure depicts the bending-like deformation (as a portion of the axisymmetric deformation) on the y-axis for different forcing frequencies, with the proportion of misaligned gears on the x-axis, starting at a single gear misalignment. As mentioned before, it is important to note that the graphs do not begin at the same point on the horizontal axis because the different diameter piles have varying amounts of total rotating masses and a single gear represents a different proportion of these masses for each pile. Furthermore, the first two pile diameters D = 0.762 and D = 3 are only available as a single point on the graphs since according to Table 4.4, the hammer that those piles are driven with already consist of only 4 gears, which makes a single gear misalignment already 25% of the total gears.
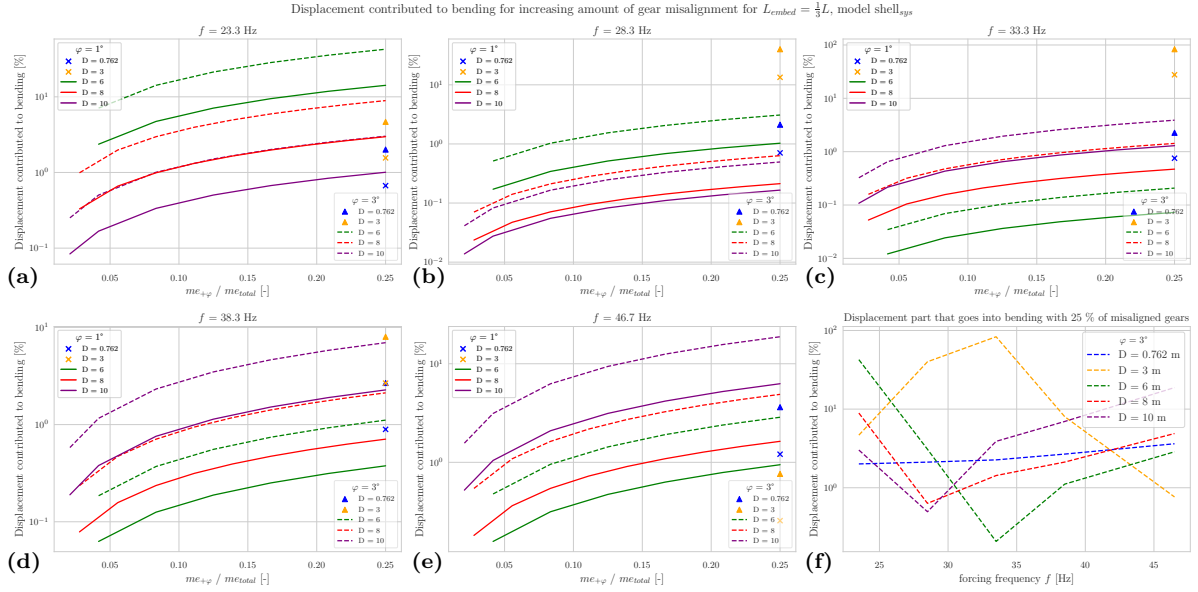
Figure 4.15: Displacement ratio with increased amount of misaligned gears up to 25 % of the total for all diameters, forcing frequencies and gear phase-shifts for model shell$_{sys}$. Embedment depth $\frac{L}{3}$

As shown in Figure B.12 (a), it is evident that the highest displacement ratio in the lowest forcing frequency range is for the pile with diameter 6. This ratio increases at an exponential rate, from 7% to 43% with an increase in the proportion of misaligned gears. At this lower forcing frequency range, the bending-like displacement values decrease as the pile diameter increases. However, as the forcing frequency reaches the mid-range, specifically at $f = 33.3$ Hz, this trend changes, and at higher forcing frequencies, the bending-like displacement portion is higher for larger diameter piles. This applies on a phase shift of $\varphi = 3°$. This applies on a phase shift of $\varphi = 3°$. As previously mentioned, for the misalignment of 1°, these values can be divided by three. For a clear overview of this described trend, see Figure B.12 (f), where the displacement contributed to bending-like with a misaligned gear proportion equal to 25% is combined in 1 graph.

50% misaligned gears
Increasing the proportion of misaligned gears to 50% of the total amount causes a doubling of all the values from Figure B.12 (f). The upper limit value of around 10% is not reached for a slender pile of diameter $D = 0.762$m and $L = 30$m, as the displacement ratio for bending remains between 4 and 7% across the entire range of forcing frequencies. For the pile with diameter of 3m, the bending-like displacement effect falls below the threshold only in the highest range of forcing frequencies above 40 Hz. However, at lower frequencies, specifically in the mid-range of 28-35 Hz, the bending-like deformation contribution exceeds 100%, which means that the pile will only displace in the lateral direction. For the three largest diameter piles from 6 to 10 m, the trend is opposite, with the mid-range of forcing frequencies having the least effect and still remaining below the threshold value of 10%, and only increasing in the highest and lowest forcing frequencies. A detailed graph is included in Annex B, Figure B.14.

Even a small misalignment of gears, as low as 6%, can significantly impact displacement contributed to lateral pile motion during offshore pile driving. This is due to the lower bending stiffness of piles compared to their axial stiffness. In this study, the amount of lateral pile motion is considered as significant when it is more than 10% that of the axisymmetric displacement. Unintended bending-like displacement can affect the drivability. The drivability can be affected since the main purpose of vibro driving is the axial penetration of the pile in the soil. If bending-like displacements are involved, it can hinder the efficiency of axial penetration.

On the other side, radial vibrations resulting from circumferential mode $n = 1$, can also have bene-

fits if the absolute displacement is not too large, particularly in terms of loosening soil and improving drivability, provided the bending-like displacement remains relatively small. However, when it comes to offshore pile driving, the sound waves produced by these radial vibrations are a significant concern. Misalignment can cause radial vibrations ($n = 1$) across a range of frequencies up to the highest forcing frequency. Figure B.19 in Annex B demonstrates that radial vibrations resulting from $n = 1$ modes, are excited at all their natural frequencies, while axisymmetric vibrations are not, as shown in Figure B.18. Moreover, the inherent frequencies of axisymmetric vibrations are more spaced out and show a dip. Consequently, when radial vibrations are excited across all natural frequencies and axisymmetric vibrations experience a dip, bending-like displacement can become significant in comparison to axisymmetric displacement. This is more likely to happen with larger diameter piles because their radial vibrations are more densely distributed within the range of forcing frequencies, while axisymmetric vibrations have more separated frequencies.

In the case of a 3-meter diameter pile, up to 98% of the contribution to bending-like displacement can be observed. This can be explained by examining the modal amplitudes of axisymmetric and bending-like modes and displacement frequency responses shown in Annex B, Figures B.20 and B.21, as well as Figures B.18 and B.19. The dip in axisymmetric vibrations at a driving frequency of 33.3 Hz, with a corresponding peak in bending-like vibrations, causes an increase in relative displacement between axisymmetric and bending-like motion, which can hinder axial penetration efficiency.

Response to near frequencies
The displacement frequency response for both axisymmetric and bending ($n = 1$) vibrations are attached in Annex B, specifically in Figures B.18 and B.19. As previously discussed above, the range of frequencies that excite bending vibrations extends from near zero up to the highest forcing frequency, while axisymmetric vibrations do not respond to all frequencies. Instead, axisymmetric vibrations have a high response only at the fundamental and at most of the driving frequencies. Conversely, bending vibrations respond to all the natural frequencies. At certain forcing frequencies, axisymmetric vibrations experience a dip while bending vibrations become more pronounced. This can lead to large bending-like deformations compared to axisymmetric deformations.

4.6. Effect of element type on pile response
As mentioned in section 3, the parametric study was done on both shell elements and simple 1D bar elements in order to compare the response of large diameter piles, when modeled as simple 1D bar elements. The displacement response of the piles with diameter of 6m and larger are given in Figure 4.16 below.
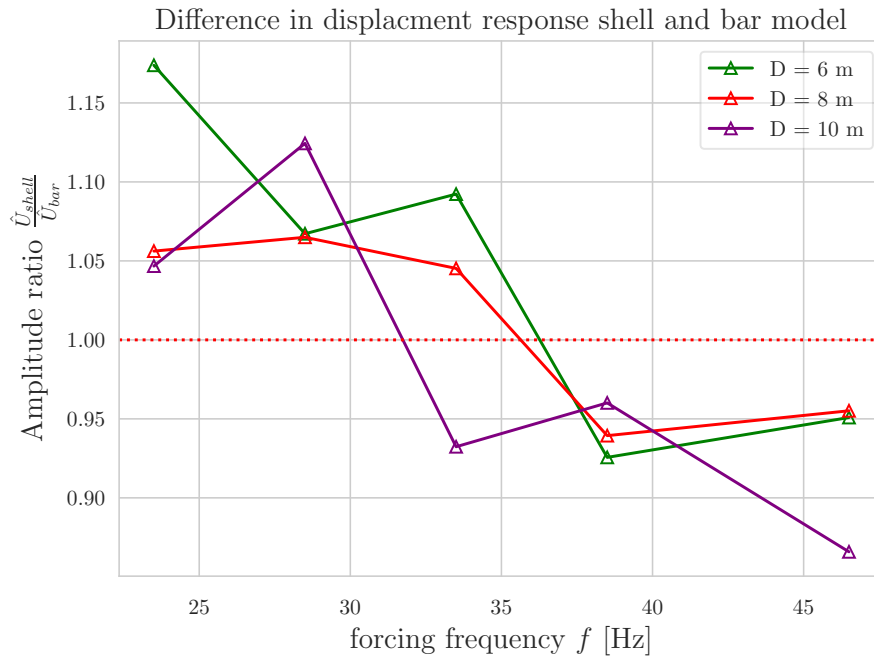
Figure 4.16: Shell elements to bar elements displacement response ratio for large diameter piles

The figure shows a similar trend across all three large diameter piles, with the shell element model yielding a greater response (compared to the 1D bar element model) at lower forcing frequencies and a lower response at higher forcing frequencies. Therefore, the degree to which the 1D bar element model overestimates or underestimates the response, relative to the shell element model, depends on the driving frequency.

On the premise that the shell model provides a more accurate representation of the behavior of monopiles in real-world scenarios, the use of 1D bar elements in modeling can lead to a maximum underestimation of 17% and a maximum overestimation of 14% in the pile response.

5

Conclusions

The aim of this thesis was to investigate the effects of misalignments in vibratory hammers on the response of monopiles under vibratory driving. The growing demand for wind energy has led to the need for larger offshore wind turbines, and vibratory pile driving has become a common technique for installing the large monopiles needed to support these turbines. However, current engineering models for vibratory pile driving are generally not well defined for larger pile diameters and more complex vibratory action on top of the pile. Additionally, misalignments in the counter-rotating eccentric masses of the vibratory hammer can produce unintended bending motions in the pile. Therefore, this study aimed to develop a vibratory hammer model and study the pile response through coupling of the hammer model with the pile model and a simplified soil reaction, as well as conducting a parametric study of the pile response to imperfections in the modeled vibratory hammer. The effects of gear misalignment on the response of monopiles under vibratory driving, including force transfer, driving frequency range for spring activation, power consumption, and bending displacements, were investigated in this study. The following sections summarize the main findings and conclusions of this research.

5.1. Summary of the main findings

The main findings of this study are summarized in this section answering the research questions, with a focus on results that pertain to all three subjects of the study. Further, more detailed findings for each subject will be presented in this section.

- In general, it was found that there was no significant impact on axial vibrations as a result of misalignment of rotating masses. This means that the force transfer ratio, the relative motion between the hammer and pile, and power consumption for axial vibrations remained unchanged, regardless of whether there was misalignment or not.

- The embedment depth had little to no effect on the three subjects studied. However, the impact increased with increasing soil stiffness, thus, having a lesser effect in looser soil.

- There is a noticeable discrepancy between the actual force exerted by the hammer and the assumed force in current practices, leading to a force transfer ratio of 0.5 to 0.7 for smaller diameter piles. In the initial design phase of pile drivability prediction models, when the decision is made not to model the hammer, it is important to include force transfer ratios in simple engineering models.

- Modeling the hammer-pile-soil system with shell elements in stead of 1D rod elements yields similar trends in the responses.
  However, for large diameter monopiles, the absolute values of the responses differ between rod and shell elements. When modeling large diameter piles with rod elements, displacement responses can differ by up to 17%. This difference could result in either an overestimation or underestimation of the response, depending on the forcing frequency. Modeling large diameter piles with simple 1D rod elements leads to an underestimation of the response in the lower driving frequency range

and an overestimation in the higher driving frequency range.

- It was determined that even if as much as 50% of the eccentric masses are misaligned, the impact of bending vibrations on the power consumption of the vibratory hammer is insignificant. Nonetheless, bending displacement can become substantial when 6% of the eccentric masses are misaligned. As a general rule, smaller diameter piles are more susceptible to vibrations at lower frequency ranges, while larger diameters are impacted in higher frequency ranges.

- Only large diameter monopiles are susceptible to axial vibrations near their natural frequencies, while all diameter piles are affected by bending vibrations near their natural frequencies. Furthermore, bending vibrations have more excited natural frequencies within the frequency range of interest, which is the range of common driving frequencies used by vibratory hammers.

- Isolator springs are effectively activated in the region of higher driving frequencies (> 28 Hz) for large diameter monopiles. In the case of small diameter piles (< 3 m), the relative motion between suppressor housing and pile head remained above unity for all driving frequencies, meaning poor activation of the isolator springs.

5.2. Conclusions and recommendations based on the study

Force transfer
The results suggest that considering hammer-vibrator interactions is important for obtaining a more accurate representation of the driving force that is actually transmitted from the hammer to the pile, particularly for smaller diameter piles (<3m). The vibrator to pile mass ratio has a strong influence on the force transfer ratio, with larger piles having a higher force transfer ratio at lower forcing frequencies. In the case of large diameter piles, resonance in the axial response in $n = 0$ can occur within the typical driving frequencies and strongly excite the pile's natural frequencies, affecting its response. For large diameter piles, the force transfer ratio is lower at higher forcing frequencies (>35Hz) and vice versa. Smaller diameter piles also follow this trend, however, their natural frequencies that get strongly excited are not within the typical range of forcing frequencies, but higher.

- The pile diameter and soil stiffness play an important role in the effect of embedment depth on the force transfer ratio. Large diameter piles are only influenced by stiffer soils, while small diameter piles (0.762m) are also influenced by loose soils at high forcing frequencies (>38Hz). In general, the force transfer ratio decreases with increasing embedment depth.
- In general, the ratio increases with increasing forcing frequency and with increasing diameter.

The study found that proper consideration of hammer-pile interactions is necessary in pile driving models, particularly for smaller diameter piles. There is a noticeable discrepancy between the actual force exerted by the hammer and the assumed force in current practices, leading to a force transfer ratio of 0.5 to 0.7 for smaller diameter piles. On the other hand, in larger diameter piles, resonance behavior may be observed, resulting in a force transfer ratio greater than 1. In the initial design phase of pile drivability prediction models, when the decision is made not to model the hammer, it is important to include force transfer ratios that are less than unity in simple engineering models.

Spring activation
The model provided understanding into the behaviour of elastomere pads in the vibratory hammer and the effect of parametric study parameters was evaluated.

The results suggest that the pile mass has a strong influence on the activation of the isolator springs, particularly in the case of small diameter piles that can be too lightweight. There is a reduced effectiveness of isolator springs in vibratory hammers for small diameter piles. Increasing the driving frequency improves the effectiveness. In contrast, hammers used for large diameter piles are activated at all driving frequencies above 28 Hz due to the great mass of the monopiles.

For small diameter piles, it is important to consider the negative effects of not activating isolator springs correctly. This can result in excessive vibrations transmitted to the crane, as well as reduced driving efficiency due to extra energy being lost as vibrations.

On the other hand, offshore monopile foundations are typically of large diameter and length, so the weight of the pile is less likely to cause problems with isolator spring activation. Even with thin-walled pile designs, the overall weight of the pile remains significant, ensuring that isolator springs will activate, specifically at higher driving frequencies. At low driving frequencies however, (<28 Hz) it is less likely that the isolator springs are activated, regardless of the size of the pile. When deciding on low frequency driving, this should be taken into account when estimating the driving efficiency.

When designing the vibratory hammer, the isolator springs are given a low stiffness to keep the natural frequency of the suppressor system much lower than the driving frequency, which is crucial for proper vibration isolation. However, the system has multiple natural frequencies, and when connected to the pile, the natural frequencies can change significantly. Although designing the elastomeric pads with low stiffness ensures a low first natural frequency (around 1-2 Hz), the second natural frequency can come close to the driving frequencies, especially if the pile mass is too light. And as it was seen in Figure 4.5, in the modes that correspond to the second natural frequency, the suppressor motion was dominant, while the pile showed a rigid body motion. This should be considered for small diameter piles in particular.

- When using piles with a smaller diameter, it may lead to higher natural frequencies that come close to driving frequencies and contribute to the suppressor motion. This was observed for pile with diameter of 0.762 m.

- Based on the observations, the effectiveness of the elastomere pads may be reduced when the natural frequency of the vibration system is close to the forcing frequency. This was the case for all diameter piles of 3 m and above for the lowest driving frequency.

- **Stiffness elastomer pads** It's important to ensure that the stiffness of the elastomere pads is appropriate for the intended pile size and driving frequency. This will help prevent resonance and ensure effective isolation of vibrations.

- **Operating frequency** Consider the operating frequency of the pile driving system, as this can affect the spring activation. If the natural frequency is close to the operating frequency, there may be a risk of resonance, which can reduce the effectiveness of the elastomere pads. Higher operating frequencies for large diameter piles is effective in spring activation.

- **Pile mass** The pile mass also influences the natural frequency of the hammer system. Ensuring that the stiffness of the elastomer pads are sufficiently small can provide effective isolation. However, there is no information on documentations of the design of the elastomere pads that provide insight in the range of pile masses where the isolator springs provide effective isolation. With small diameter piles there is a chance that the mass is too low, which increases the natural frequency of the system, making it possible to get closer to the driving frequency of the hammer and resulting in poor spring activation. It has been shown that only designing very little spring stiffness may not be sufficient as the system consists of many natural frequencies and the pile mass has an considerable effect on it. The common pile dimensions, thus masses, from practice are assessed in this study and it has been shown that even with large diameter monopiles, when driving in the lower frequency range (<28 Hz), the natural frequency comes close to the driving frequency en resulting in poor spring activation.

Overall, to maintain the effectiveness of the elastomer pads in vibratory pile driving, it's important to consider the interplay between the stiffness of the pads, the operating frequency, the pile mass, and the natural frequency of the hammer system. By monitoring these factors and making adjustments as needed, effective isolation of vibrations can be ensures and the efficiency of the pile driving process can

be improved. Regular monitoring of the vibration levels during pile driving can provide valuable information about the effectiveness of the elastomere pads. This can help identify issues such as resonance, which can be addressed to improve the isolation performance.

Effect of misalignment on power consumption and displacement contribution
The study examined the impact of gear misalignment on the vibratory hammer's performance in terms of power consumption and the behaviour of the pile in terms of displacement response. The results show the following:

- Gear misalignment has a negligible effect on vibratory hammer power consumption by bending vibrations. Therefore, accounting for gear misalignment is not necessary when assessing power consumption.

- When looking at displacement, even a misalignment as small as 1° significantly affects the contribution to bending displacement when 17% of the gears are misaligned. A 3° misalignment requires only $\frac{1}{20}$ of the gears to be misaligned to affect bending displacement. Therefore, it is essential to carefully account for consequences of a possible gear misalignment. Effect decreases with increasing pile diameter.

- The vibratory hammer requires significantly less power to produce a considerable amount of bending displacement than axial displacement, owing to the pile's lower bending stiffness compared to its axial stiffness. This can have an impact on both the performance and structural stability of the pile, as well as its drivability.

- Bending vibrations do give response in all natural frequencies up to the highest driving frequency. In axial vibrations this is only the case for large diameter monopiles.

The likelihood of encountering issues related to bending vibrations during vibratory pile driving is determined by multiple factors, such as the probability of their occurrence and the properties of the pile and its surroundings. These factors collectively determine the degree to which bending vibrations can pose a problem and therefore it is essential to consider the possibility of radial vibrations resulting from bending when analyzing the drivability of a pile. Additionally, these vibrations can generate sound waves that could have adverse effects on marine life in offshore engineering applications. To accurately evaluate the sound waves produced by offshore vibratory pile driving, it is crucial to account for both the sound waves resulting from radial expansion caused by axial deformation $n = 0$ and those originating from bending-like motions $n = 1$.

Bending vibrations can be beneficial in some circumstances in the way that it can loosen and displace the soil, which can make it easier for the pile to penetrate axially. However, it is important to balance the beneficial effects of soil displacements with the potential negative effects of unintended bending-like motions, which can affect the drivability due to bending displacements and potentially affect the bearing capacity of the pile.

5.2.1. Limitations of the study and suggestions for future work
While the current study offered valuable insights into the response of piles to vibro hammer action, including the effects of imperfections, there are certain limitations to the research that should be addressed in future work. The following recommendations outline areas for improvement in the field:

- The current work's main limitation is its linear modeling of the hammer-pile-soil system, which differs from the heavily nonlinear reality. Future work should aim to take into account the nonlinear effects that may arise in the system, as these effects may deviate considerably from the results obtained from the linear model and are particularly important in pile driving process. However, it is worth noting that the insights gained from the current study remain valuable, as the main focus was on relative values rather than absolute values. If there is a desire to conduct experiments in real-life settings, the nonlinear effects should be incorporated in the model. It is

important to emphasize that the current model was designed for simple engineering models, and therefore, the choice to model the system as linear was made to ensure a quick and efficient model.

- The study does not consider the external moment produced by rotating eccentrics with misaligned masses acting on the pile, which also consumes power. However, it has been demonstrated that the power consumed by bending vibrations is negligible, even with a significant amount of misaligned masses. Therefore, the addition of an external moment may not significantly affect power consumption, but it is unpredictable how much it will change. The contribution of displacement to bending was shown to have a significant impact, so the rotation caused by the moment may be important in this regard.
- The misalignment degrees of 1° and 3° are rough estimates of what is possible in practice, and the proportion of misaligned gears up to 50% is chosen to provide insight into upper and lower limits of when it becomes a problem. More than this upper limit is likely impossible in practice. However, a probability study is needed to determine the likelihood of misalignment in practice, to what degree is expected, and what proportion of total gears will be misaligned. Such a study could emphasize or refute the importance of considering possible misalignment.
- The study only considers circumferential modes for $n = 0$ and $n = 1$, representing axial expansion/contraction mode and bending mode, respectively. Misaligned masses are assumed to cause a bending mode, but for larger diameter offshore piles requiring more than one hammer, a more precise analysis can be done by applying the hammer action to specific locations along the circumference of the pile. This will allow for a more accurate representation of the clamps and will show the effect of the horizontal force produced by misalignment, which is expected to have a different effect on the pile than just bending. However, this approach is computationally expensive and not suitable for initial design phases.
- The stiffness of elastomer pads has a significant impact on the natural frequencies of the system. A parametric study focused on this topic can be conducted to determine why the lower driving frequency still has spring activation even though it is far from the natural frequencies of the system.

References

[1] *Follow-up study: Climate change remains the most pressing global issue.* Tech. rep. SE-162 92 Stockholm, Sweden: Vattenfall AB, 2020.

[2] P. Zhai, A. Pirani, and et al. *Climate Change 2021: The Physical Science Basis. Contribution of Working Group I to the Sixth Assessment Report of the Intergovernmental Panel on Climate Change.* Tech. rep. Cambridge University Press. In Press IPCC UN Environmental programme, WMO, 2021.

[3] *Offshore Wind Outlook 2019.* Tech. rep. IEA Paris, 2019.

[4] P. Zhai, A. Pirani, and et al. *National Climate Agreement The Netherlands.* Tech. rep. Binnenhof 14, The Hague: Dutch Central Government (Rijksoverheid), 2019.

[5] A. Athanasia, G. Anne-Bénédicte, and M. Jacopo. "The offshore wind market deployment: forecasts for 2020, 2030 and impacts on the European supply chain development". In: *Energy Procedia* 24 (2012), pp. 2–10.

[6] L. Ramírez, D. Fraile, and G. Brindley. *Offshore Wind in Europe, key trends and statistics 2019.* Tech. rep. WindEurope, 2020.

[7] P. C. Meijers, A. Tsouvalas, and A.V. Metrikine. "The Effect of Stress Wave Dispersion on the Drivability Analysis of Large-Diameter Monopiles". In: *SciVerse ScienceDirect* (2017).

[8] A. Tsetas, A. Tsouvalas, and A.V. Metrikine. "Installation of Large-Diameter Monopiles: Introducing Wave Dispersion and Non-Local Soil Reaction". In: *J. Mar. Sci. Eng* 9 (2021).

[9] . *Basic principles of hammers for sheet pile installation.* Pile driving contractors association.

[10] Deltares. *New pile installation method for offshore wind monopiles.* URL: https://www.deltares.nl/en/projects/new-pile-installation-method-offshore-wind-monopiles/ (visited on 02/26/2022).

[11] V. Whenham and A. Holeyman. "Load transfers during vibratory driving". In: *Geotech. Geol. Eng.* 30 (2012), pp. 1119–1135.

[12] F. Rausche. "Modeling of vibratory pile driving". In: *GRL Engineers Inc.* ().

[13] *COMPARISON OF IMPACT VERSUS VIBRATORY DRIVEN PILES: With a focus on soil structure interaction.* Tech. rep. 14007-01. Hawthorne, NJ, US: Deep Foundation Institute, Gavin Doherty Geo solutions, Sept. 2015.

[14] E. A. L. Smith. "Pile driving analysis by the wave equation". In: *Am. Soc. of Civ. Eng. Trans.* 127.3306 (1962), pp. 1145–1193.

[15] A. J. Deeks and M. Randolph. "Analytical modelling of hammer impact for pile driving". In: *Int. Jour. for Num. and An. Meth. in Geom.* (1993).

[16] F. Petrini et al. "Structural Design and Analysis of Offshore Wind Turbines from a System Point of View". In: *Wind Engineering* 34.1 (2010), pp. 85–108.

[17] B.C. O'Kelly and M. Arshad. "20 - Offshore wind turbine foundations – analysis and design". In: *Offshore Wind Farms.* Ed. by Chong Ng and Li Ran. Woodhead Publishing, 2016, pp. 589–610. ISBN: 978-0-08-100779-2. DOI: https://doi.org/10.1016/B978-0-08-100779-2.00020-9. URL: https://www.sciencedirect.com/science/article/pii/B9780081007792000209.

[18] Dan Kallehave et al. "Optimization of monopiles for offshore wind turbines". In: *Philosophical Transactions of the Royal Society A: Mathematical, Physical and Engineering Sciences* 373.2035 (2015), pp. 1–15. DOI: 10.1098/rsta.2014.0100. eprint: https://royalsocietypublishing.org/doi/pdf/10.1098/rsta.2014.0100. URL: https://royalsocietypublishing.org/doi/abs/10.1098/rsta.2014.0100.

[19] Tougaard Lucke Tyack Madsen Wahlberg. "Wind turbine underwater noise and marine mammals: implications of current knowledge and data needs". In: *MARINE ECOLOGY PROGRESS SERIES* 309 (2006), pp. 279–295.

[20] S. L. Lee et al. "Rational wave equation model for pile-driving analysis". In: *J. Geotech. Engrg* 114.3 (1988), pp. 306–325.

[21] D. V. Isaacs. "Rational wave equation model for pile-driving analysis". In: *J. of Inst. of Eng. Austr.* 3.9 (Sept. 1931), pp. 306–325.

[22] D. C. Warrington. "Improved methods for forward and inverse solution of the wave equation for piles". PhD thesis. Chattanooga, Tennessee: The University of Tennessee at Chattanooga, Aug. 2016.

[23] H. A. Hejazi. "The influence of forced longitudinal vibrations on rods penetrating soils". PhD thesis. Columbus, OH: Ohio State University, 1963.

[24] A. V. Metrikine and A. C. W. M. Vrouwenvelder. *Dynamics of structures, Wave dynamics.*

[25] Don Warrington. "DEVELOPMENT AND POTENTIAL OF THE WAVE EQUATION IN CLOSED FORM AS APPLIED TO PILE DYNAMICS". In: (Jan. 2019).

[26] Peter Meijers, A. Tsouvalas, and Andrei Metrikine. "The Effect of Stress Wave Dispersion on the Drivability Analysis of Large-Diameter Monopiles". In: *Procedia Engineering* 199 (Dec. 2017), pp. 2390–2395. DOI: 10.1016/j.proeng.2017.09.272.

[27] C. H. Samson L. L. Lowery T. J. Hirsch. *Pile driving analysis - simulation of hammers, cushions, piles and soil.* Tech. rep. 2-5-62-33. College Station, Texas: Texas transport institution, Texas AM University, Aug. 1967.

[28] A. Ismail. "Prediction of resistance to pile driving using evolutionary neural network". In: *Multiscale and Multidisciplinary Modeling, Experiments and Design* 2 (2019), pp. 49–61. DOI: 10.1007/s41939-018-0030-z.

[29] D. Espinoza. *Application of wave propagation theory in pile driving analysis.* Tech. rep. West Lafayette, Indiana: Purdue University, Dec. 1991.

[30] Y. X. Wang. "Determination of capacity of shaft bearing piles using the wave equation". In: *Proceedings of the Third International Conference on the Application of Stress-Wave Theory to Piles.* Vancouver: Bi-Tech Publishers, 1988, pp. 337–342.

[31] K. Uto, M. Fuyuki, and M. Sakurai. "An equation for the Dynamic Bearing Capacity of a Pile Based on Wave Theory". In: *Proceedings of the International Symposium on Penetrability and Drivability of Piles.* Tokyo: Japanese Soc. of Soil Mech. and Found. Eng., 1985.

[32] A. J. Deeks. "Numerical Analysis of Pile Driving Dynamics". PhD thesis. Perth, Australia: The University of Western Australia, 1992.

[33] Don. C. Warrington. "Persisten Issues in the Wave Equation for Piling for Both Forward and Inverse Methods". In: ().

[34] *Owners Manual Vibratory Hammers.* International construction equipment. Sliedrecht, The Netherlands.

[35] K. Rainer Massarsch, Carl Wersäll, and Bengt Fellenius. "Vibratory driving of piles and sheet piles - State of practice". In: *Proceedings of the Institution of Civil Engineers - Geotechnical Engineering* (Dec. 2020), pp. 1–43. DOI: 10.1680/jgeen.20.00127.

[36] Alain E. Holeyman. "Keynote lecture: Vibratory driving analysis". In: 2019.

[37] Andreas Öchsner. *One-Dimensional Finite Elements.* Springer, 2013. ISBN: 978-3-642-31796-5.

[38] A. Tsouvalas. *Structural Response to Earthquakes.* TU Delft, 2020.

[39] Peter Wriggers. *Nonlinear Finite Element Methods.* ISBN: 978-3-540-71000-4.

[40] K. Watanabe, F. Pisanò, and B. Jeremić. "Dicretization effects in the finite element simulation of seismic waves in elastic ans elastic-plastic media". In: *Engineering with Computers* 33.3 (2017), pp. 519–545.

[41] Boyun Guo et al. "Chapter 6 - Operating Stresses". In: *Offshore Pipelines (Second Edition)*. Ed. by Boyun Guo et al. Second Edition. Boston: Gulf Professional Publishing, 2014, pp. 65–78. ISBN: 978-0-12-397949-0. DOI: https://doi.org/10.1016/B978-0-12-397949-0.00006-6. URL: https://www.sciencedirect.com/science/article/pii/B9780123979490000066.

[42] A. Tsetas, A. Tsouvalas, and A. V. Metrikine. "A non-linear three-dimensional pile-soil model for vibratory pile installation in layered media". In: *International Journal of Solids and Structures* (2023).

[43] Arthur W. Leissa. *Vibration of shells*. Scientific, Technical Information Office, National Aeronautics, and Space Administration (NASA), 1973. ISBN: 841144090.

[44] C. Rodrigues et al. "Finite element dynamic analysis of beams on nonlinear elastic foundations under a moving oscillator". In: *European Journal of Mechanics - A/Solids* 68 (2018), pp. 9–24. ISSN: 0997-7538. DOI: https://doi.org/10.1016/j.euromechsol.2017.10.005. URL: https://www.sciencedirect.com/science/article/pii/S0997753817301572.

[45] Iancu-Bogdan Teodoru and Vasile Muşat. "The Modified Vlasov Foundation Model: An Attractive Approach for Beams Resting on Elastic Supports". In: *Electronic Journal of Geotechnical Engineering* 15 (Jan. 2010).

[46] Vicente Negro. "Monopiles in offshore wind: Preliminary estimate of main dimensions". In: *Ocean Engineering* 133 (2017), pp. 253–261.
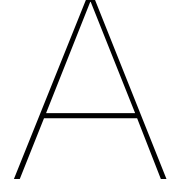
Appendix A: Matrices

Mass and stiffness matrices for thin circular cylindrical shell elements

The mass matrix $\mathbf{M}_0$ and stiffness matrix $\mathbf{K}_0$ for $n = 0$ are given as follows:

$$\mathbf{M}_0 = \rho h \ell \begin{bmatrix} \dfrac{1}{3} & 0 & 0 & \dfrac{1}{6} & 0 & 0 \\[2mm] 0 & \dfrac{13}{35} & \dfrac{11\ell}{210} & 0 & \dfrac{9}{70} & -\dfrac{13\ell}{420} \\[2mm] 0 & \dfrac{11\ell}{210} & \dfrac{\ell^2}{105} & 0 & \dfrac{13\ell}{420} & -\dfrac{\ell^2}{140} \\[2mm] \dfrac{1}{6} & 0 & 0 & \dfrac{1}{3} & 0 & 0 \\[2mm] 0 & -\dfrac{9}{70} & \dfrac{13\ell}{420} & 0 & \dfrac{13}{35} & -\dfrac{11\ell}{210} \\[2mm] 0 & -\dfrac{13\ell}{420} & -\dfrac{\ell^2}{140} & 0 & -\dfrac{11\ell}{210} & \dfrac{\ell^2}{105} \end{bmatrix} \tag{A.1}$$

$$\mathbf{K}_0 = \frac{Eh}{1-\nu^2} \begin{bmatrix} \dfrac{1}{\ell} & -\dfrac{\nu}{2R} & -\dfrac{\nu\ell}{12R} & -\dfrac{1}{\ell} & -\dfrac{\nu}{2R} & \dfrac{\nu\ell}{12R} \\[2mm] -\dfrac{\nu}{2R} & \dfrac{h^2}{\ell^3}+\dfrac{13\ell}{35R^2} & \dfrac{h^2}{2\ell^2}+\dfrac{11\ell^2}{210R^2} & \dfrac{\nu}{2R} & -\dfrac{h^2}{\ell^3}+\dfrac{9\ell}{70R^2} & \dfrac{h^2}{2\ell^2}-\dfrac{13\ell^2}{420R^2} \\[2mm] -\dfrac{\nu\ell}{12R} & \dfrac{h^2}{2\ell^2}+\dfrac{11\ell^2}{210R^2} & \dfrac{h^2}{3\ell}+\dfrac{\ell^3}{105R^2} & \dfrac{\nu\ell}{12R} & -\dfrac{h^2}{2\ell^2}+\dfrac{13\ell^2}{420R^2} & \dfrac{h^2}{6\ell}-\dfrac{\ell^3}{140R^2} \\[2mm] -\dfrac{1}{\ell} & \dfrac{\nu}{2R} & \dfrac{\nu\ell}{12R} & \dfrac{1}{\ell} & \dfrac{\nu}{2R} & -\dfrac{\nu\ell}{12R} \\[2mm] -\dfrac{\nu}{2R} & -\dfrac{h^2}{\ell^3}+\dfrac{9\ell}{70R^2} & -\dfrac{h^2}{2\ell^2}+\dfrac{13\ell^2}{420R^2} & \dfrac{\nu}{2R} & \dfrac{h^2}{\ell^3}+\dfrac{13\ell}{35R^2} & -\dfrac{h^2}{2\ell^2}-\dfrac{11\ell^2}{210R^2} \\[2mm] \dfrac{\nu\ell}{12R} & \dfrac{h^2}{2\ell^2}-\dfrac{13\ell^2}{420R^2} & \dfrac{h^2}{6\ell}-\dfrac{\ell^3}{140R^2} & -\dfrac{\nu\ell}{12R} & -\dfrac{h^2}{2\ell^2}-\dfrac{11\ell^2}{210R^2} & \dfrac{h^2}{3\ell}+\dfrac{\ell^3}{105R^2} \end{bmatrix} \tag{A.2}$$

For $n = 1$, the mass and stiffness matrices $\mathbf{M}_n$ and $\mathbf{K}_n$ are given below:

$$\mathbf{M}_{n=1} = \pi\rho h\ell \begin{bmatrix} \dfrac{1}{3} & 0 & 0 & 0 & \dfrac{1}{6} & 0 & 0 & 0 \\[2mm] 0 & \dfrac{1}{3} & 0 & 0 & 0 & \dfrac{1}{6} & 0 & 0 \\[2mm] 0 & 0 & \dfrac{13}{35} & \dfrac{11\ell}{210} & 0 & 0 & \dfrac{9}{70} & -\dfrac{13\ell}{420} \\[2mm] 0 & 0 & \dfrac{11\ell}{210} & \dfrac{\ell^2}{105} & 0 & 0 & \dfrac{13\ell}{420} & -\dfrac{\ell^2}{140} \\[2mm] \dfrac{1}{6} & 0 & 0 & 0 & \dfrac{1}{3} & 0 & 0 & 0 \\[2mm] 0 & \dfrac{1}{6} & 0 & 0 & 0 & \dfrac{1}{3} & 0 & 0 \\[2mm] 0 & 0 & \dfrac{9}{70} & \dfrac{13\ell}{420} & 0 & 0 & \dfrac{13}{35} & -\dfrac{11\ell}{210} \\[2mm] 0 & 0 & -\dfrac{13\ell}{420} & -\dfrac{\ell^2}{140} & 0 & 0 & -\dfrac{11\ell}{210} & \dfrac{\ell^2}{105} \end{bmatrix} \tag{A.3}$$

$$\mathbf{K}_{n=1} = \frac{Eh}{1-\nu^2} \begin{bmatrix} K_{11} & K_{12} & K_{13} & K_{14} & K_{15} & K_{16} & K_{17} & K_{18} \\ K_{21} & K_{22} & K_{23} & K_{24} & K_{25} & K_{26} & K_{27} & K_{28} \\ K_{31} & K_{32} & K_{33} & K_{34} & K_{35} & K_{36} & K_{37} & K_{38} \\ K_{41} & K_{42} & K_{43} & K_{44} & K_{45} & K_{46} & K_{47} & K_{48} \\ K_{51} & K_{52} & K_{53} & K_{54} & K_{55} & K_{56} & K_{57} & K_{58} \\ K_{61} & K_{62} & K_{63} & K_{64} & K_{65} & K_{66} & K_{67} & K_{68} \\ K_{71} & K_{72} & K_{73} & K_{74} & K_{75} & K_{76} & K_{77} & K_{78} \\ K_{81} & K_{82} & K_{83} & K_{84} & K_{85} & K_{86} & K_{87} & K_{88} \end{bmatrix} \tag{A.4}$$

The stiffness matrix coefficients K_{11} to K_{88} can be found in Appendix A, eq. **??**

Stiffness matrix coefficients for Case n = 1

$$K_{11} = \frac{\pi}{\ell} - \frac{\pi\ell(\nu-1)}{6R} \tag{A.5}$$
$$K_{12} = \frac{3\pi\nu}{4} - \frac{\pi}{4}$$
$$K_{13} = -\frac{\pi\nu}{2}$$
$$K_{14} = \frac{\pi\nu\ell}{12}$$
$$K_{15} = -\frac{\pi}{\ell} - \frac{\pi\ell(\nu-1)}{12R}$$
$$K_{16} = \frac{\pi(\nu+1)}{4}$$
$$K_{17} = -\frac{\pi\nu}{2}$$
$$K_{18} = \frac{\pi\nu\ell}{12}$$
$$K_{21} = \frac{3\pi\nu}{4} - \frac{\pi}{4}$$
$$K_{22} = \frac{\pi h^2\ell}{36R^3} - \frac{\pi R(\nu-1)}{2\ell} - \frac{\pi h^2(\nu-1)}{24R^3\ell^2} - \frac{\ell}{12R^3}$$

$$K_{23} = -\frac{\pi h^2}{12R\ell} - \frac{7\pi h^2 \ell}{240R^3} - \frac{-7\pi \ell}{20R}$$

$$K_{24} = -\frac{\pi h^2 \nu}{12R} - \frac{\pi h^2 \ell^2}{240R^3} - \frac{\pi}{20\ell^2 R}$$

$$K_{25} = -\frac{\pi(\nu + 1)}{4R}$$

$$K_{26} = \frac{\pi h^2 \ell}{72R^3} + \frac{\pi R(\nu - 1)}{2\ell} + \frac{\pi\left(2h^2(\nu - 1) + \frac{\ell^2}{3}\right)}{2R\ell}$$

$$K_{27} = \frac{h^2}{12R\ell} - \frac{\pi h^2 \ell}{80R^3} - \frac{3\pi \ell}{20R^3}$$

$$K_{28} = \frac{\pi \ell^2 h^2}{30R^3} + \frac{\pi \ell^2}{30R}$$

$$K_{31} = \frac{-\pi \nu}{2}$$

$$K_{32} = \frac{\pi h^2 \nu}{12R\ell} - \frac{2\pi h^2}{12R\ell} - \frac{7\pi h^2 \ell}{240R^3} - \frac{7\pi \ell}{20R}$$

$$K_{33} = \frac{\pi h^2 R}{\ell^3} + \frac{\pi h^2}{5R\ell} + \frac{13\pi h^2 \ell}{420R^3} + \frac{13\pi \ell}{35R}$$

$$K_{34} = \frac{\pi h^2 R}{2\ell^2} + \frac{99\pi h^2 \ell^2}{22680R^3} + \frac{99\pi}{1890R} + \frac{\pi h^2((\nu + \frac{1}{5}) + \ell^2)}{12R}$$

$$K_{35} = \frac{\pi \nu}{2}$$

$$K_{36} = -\frac{\pi h^2 \nu}{12R\ell} - \frac{\pi h^2}{6R\ell} + \frac{\pi h^2 \ell}{80R^3} + \frac{3\pi \ell}{20R}$$

$$K_{37} = -\frac{\pi h^2 R}{\ell^3} - \frac{\pi h^2}{5R\ell} + \frac{3\pi h^2 \ell}{280R^3} + \frac{3\pi \ell}{70R}$$

$$K_{38} = \frac{\pi h^2 R}{2\ell^2} + \frac{\pi h^2}{60R} - \frac{13\pi h^2 \ell^2}{5040R^3} - \frac{13\pi \ell^2}{420R}$$

$$K_{41} = \frac{\pi \nu \ell}{12}$$

$$K_{42} = -\frac{\pi h^2 \nu}{12R} - \frac{^2 \ell^2}{240R^4} - \frac{\pi \ell^2}{20R^4}$$

$$K_{43} = K_{34}$$

$$K_{44} = \frac{\pi h^2 R}{3\ell} + \frac{\pi^2 \ell}{45R} + \frac{\pi h^2 \ell^3}{1260R^3} + \frac{\pi \ell^3}{105R}$$

$$K_{45} = K_{41}$$

$$K_{46} = -\frac{\pi h^2 \ell^2}{360R^3} - \frac{\pi \ell^2}{30R}$$

$$K_{47} = -K_{38}$$

$$K_{48} = \frac{\pi h^2 R}{6\ell} - \frac{\pi h^2 \ell}{180R} - \frac{\pi h^2 \ell^3}{1680R^3} - \frac{\pi \ell^3}{140R}$$

$$K_{51} = -\frac{\pi R}{\ell} - \frac{\pi \ell(\nu - 1)}{12R}$$

$$K_{52} = \frac{\pi(\nu - 1)}{4}$$

$$K_{53} = \frac{\pi \nu}{2}$$

$$K_{54} = \frac{\pi \nu \ell}{12}$$

$$K_{55} = \frac{\pi R}{\ell} - \frac{\pi \ell(\nu - 1)}{6R}$$

$$K_{56} = \frac{\pi}{4} - \frac{3\pi\nu}{4}$$

$$K_{57} = \frac{\pi\nu}{2}$$

$$K_{58} = -\frac{\pi\ell\nu}{12}$$

$$K_{61} = \frac{\pi(\nu+1)}{4}$$

$$K_{62} = \frac{\pi h^2 \ell}{72R^3} + \frac{\pi R(\nu-1)}{2\ell} + \frac{\pi\left(2(\frac{h^2}{12}(\nu-1) + \frac{\ell^2}{3})\right)}{2R\ell}$$

$$K_{63} = \frac{\pi h^2}{12R\ell} - \frac{\pi h^2 \ell}{80R^3} - \frac{3\pi\ell}{20R}$$

$$K_{64} = -\frac{\pi\ell^2 h^2}{360R^3} - \frac{\pi\ell^2}{30R}$$

$$K_{65} = K_{56}$$

$$K_{66} = \frac{\pi h^2 \ell}{36R^3} - \frac{\pi R(\nu-1)}{2\ell} - \frac{\pi\left(2\frac{h^2}{12}(\nu-1) - \frac{2\ell^2}{3}\right)}{2R\ell}$$

$$K_{67} = -\frac{\pi h^2}{12R\ell} - \frac{7\pi h^2 \ell}{240R^3} - \frac{7\pi\ell}{20R}$$

$$K_{68} = \frac{\pi h^2 \nu}{12R} + \frac{\pi h^2 \ell^2}{240R^3} + \frac{\pi\ell^2}{20R}$$

$$K_{71} = -\frac{\pi\nu}{2}$$

$$K_{72} = K_{36}$$

$$K_{73} = K_{37}$$

$$K_{74} = -K_{38}$$

$$K_{75} = \frac{\pi\nu}{2}$$

$$K_{76} = \frac{\pi h^2 \nu}{12R\ell} - \frac{\pi h^2}{6R\ell} - \frac{7\pi h^2 \ell^2}{240R^3\ell} - \frac{7\pi\ell}{20R}$$

$$K_{77} = K_{33}$$

$$K_{78} = -K_{34}$$

$$K_{81} = \frac{\pi\ell\nu}{12}$$

$$K_{82} = -K_{46}$$

$$K_{83} = K_{38}$$

$$K_{84} = K_{48}$$

$$K_{85} = -\frac{\pi\ell\nu}{12}$$

$$K_{86} = K_{68}$$

$$K_{87} = K_{78}$$

$$K_{88} = K_{44}$$

B

Appendix B: Figures

B.0.1. Time domain responses
Time-domain responses for main model and verification models
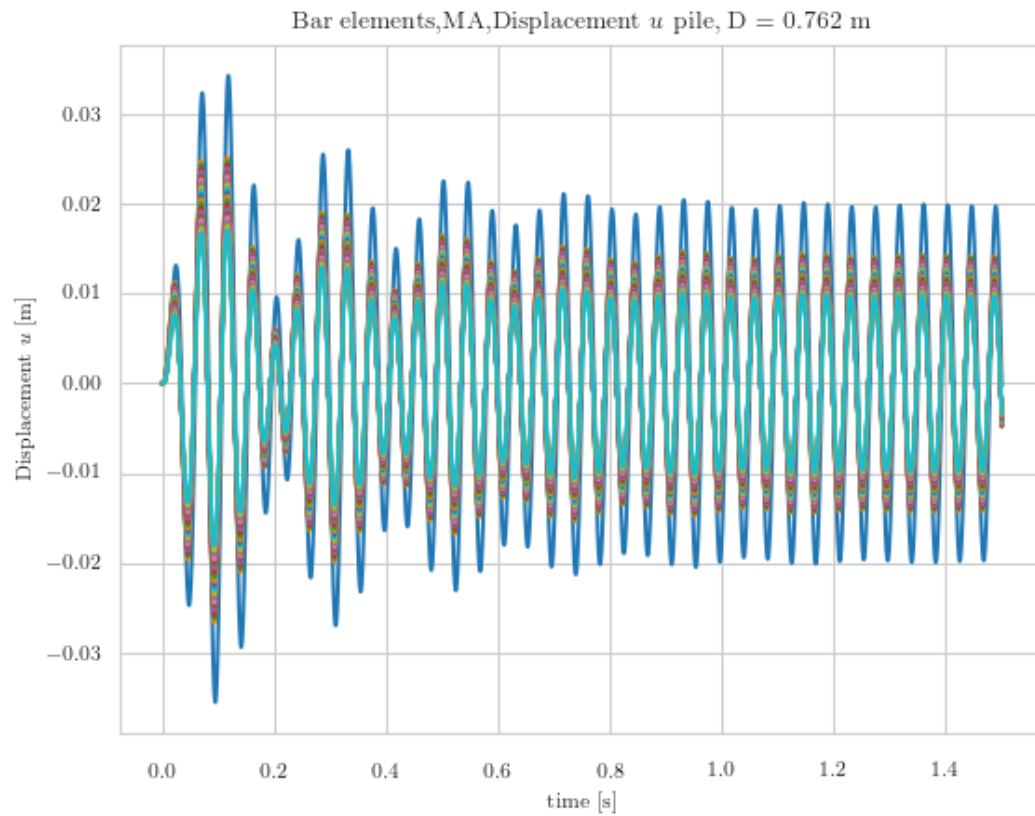
Figure B.1: Axial displacement response with 1D bar elements
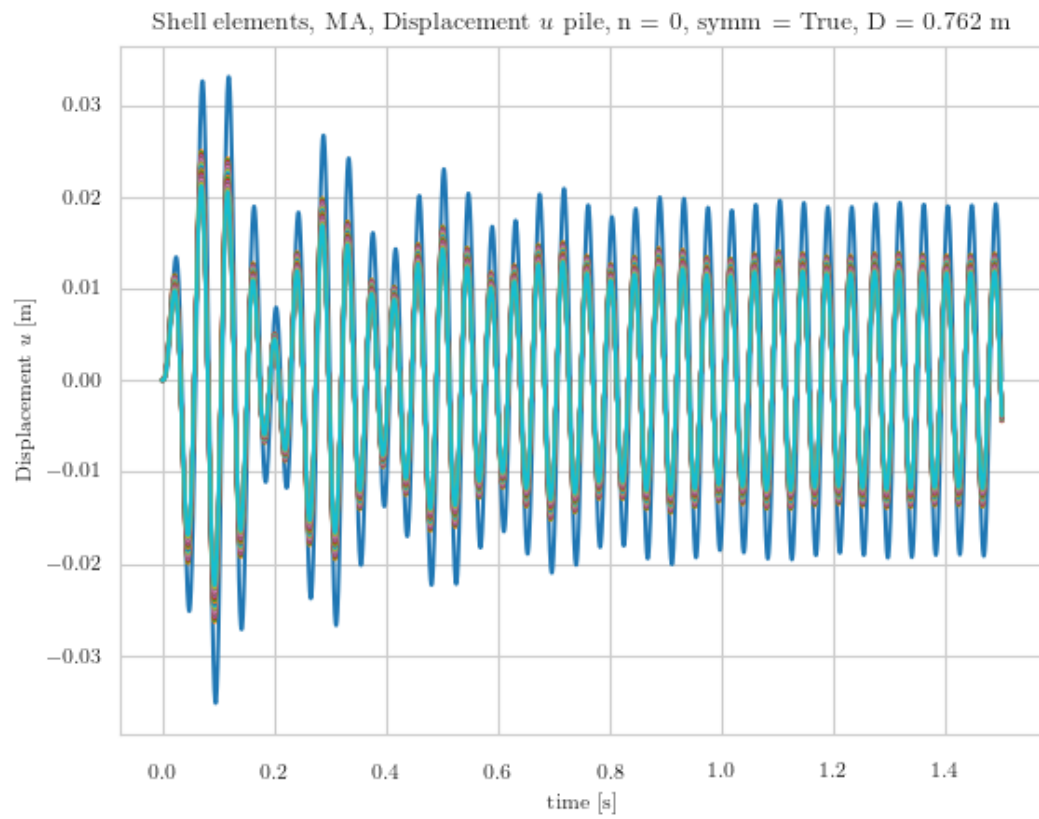
Figure B.2: Axial displacement response with shell elements, $n = 0$
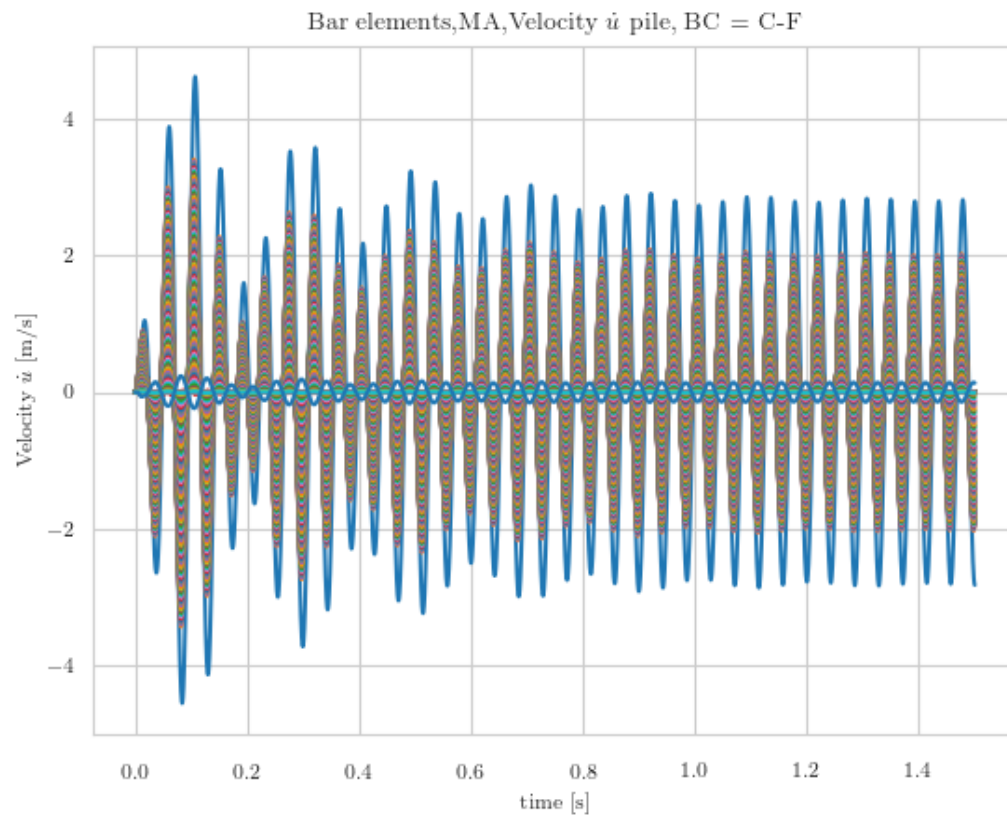
Figure B.3: Axial velocity response with 1D bar elements
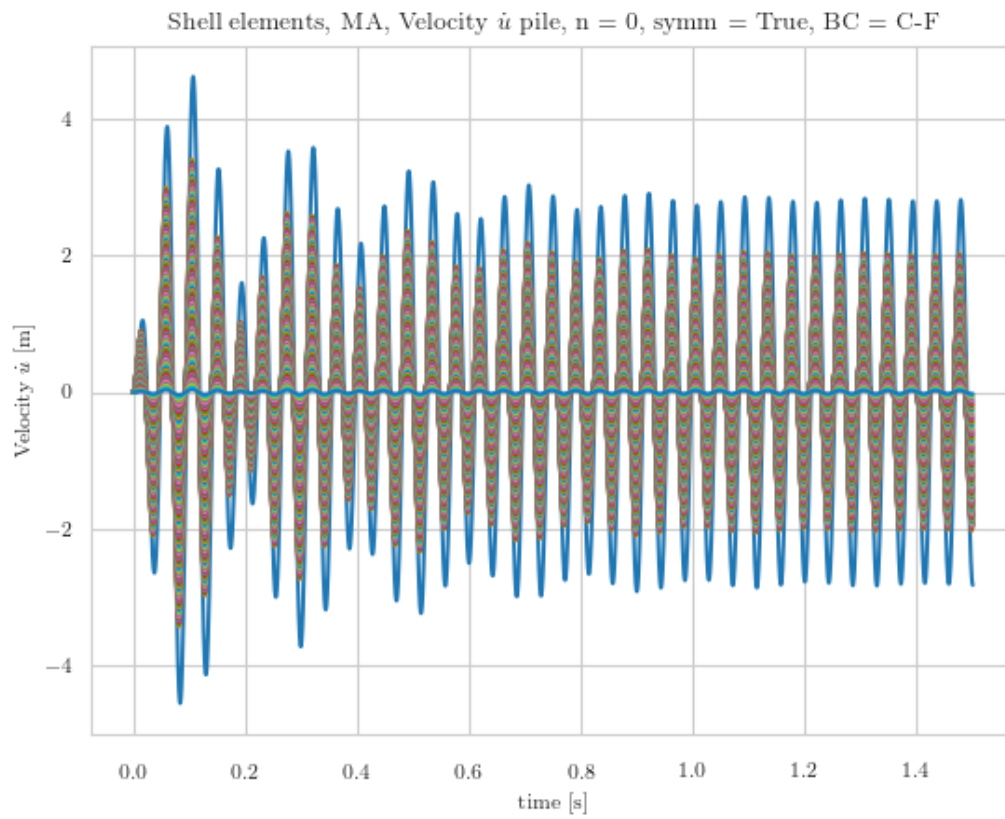
Figure B.4: Axial velocity response with shell elements, $n = 0$
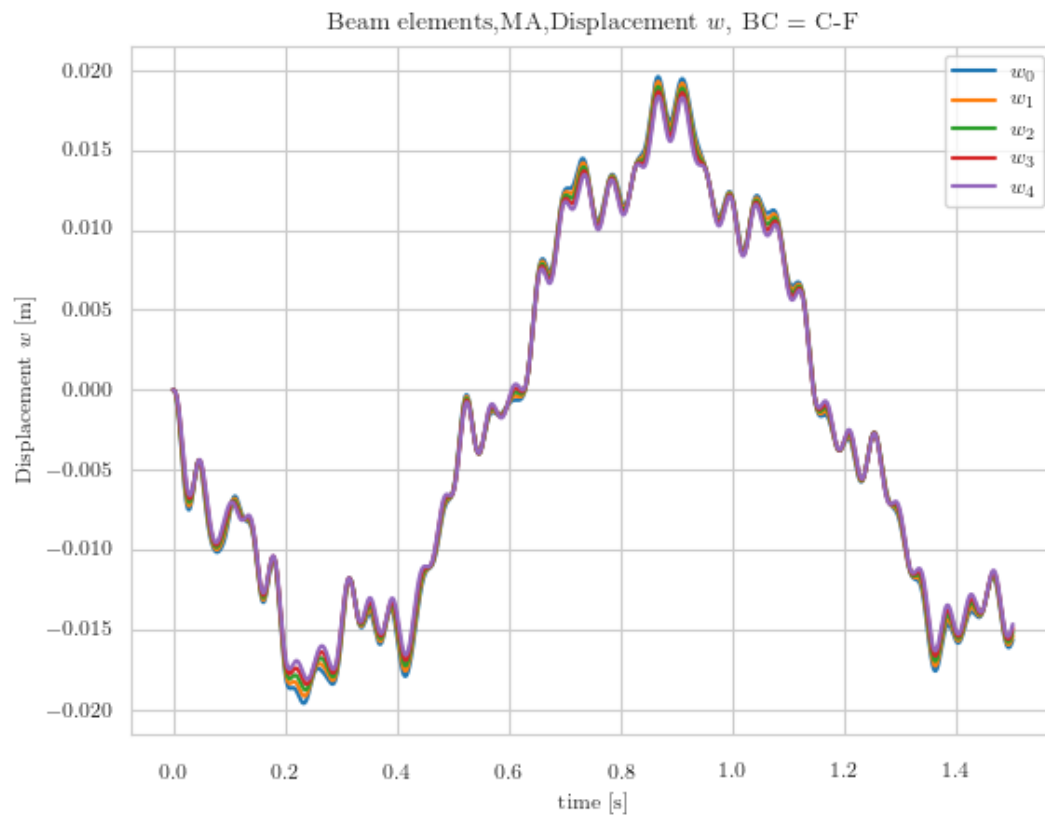
Figure B.5: Bending displacement response with 1D beam elements
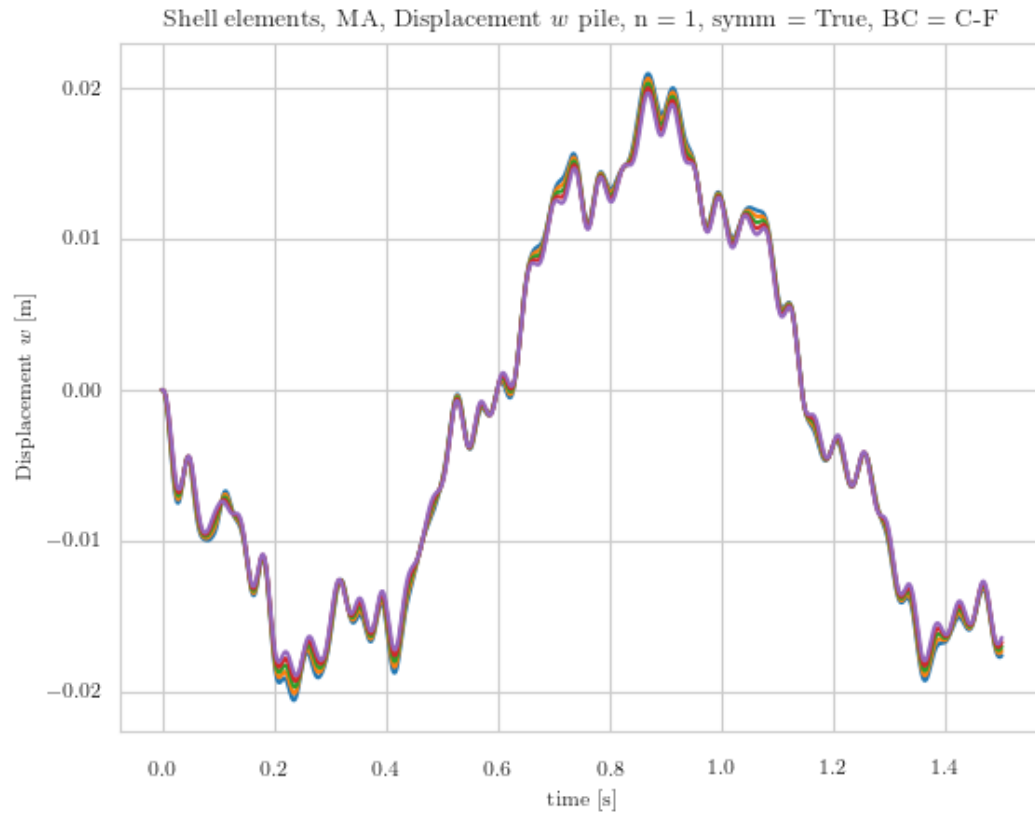
Figure B.6: Bending-like displacement response with shell elements, $n = 1$

B.0.2. Effect of increased amount and degree of misalignment

Only embedment depths of $\frac{L}{3}$ were included, as the effect of embedment depth was only investigated for the parameters in the parametric study, which did not consider an increased amount of misaligned gears. Furthermore, the study showed that the impact of embedment depth was minimal, so the results from the models for the impact of an increased amount of misaligned gears are solely based on this embedment depth.

Power consumption by bending vibrations for 25% misaligned gears, loose soil
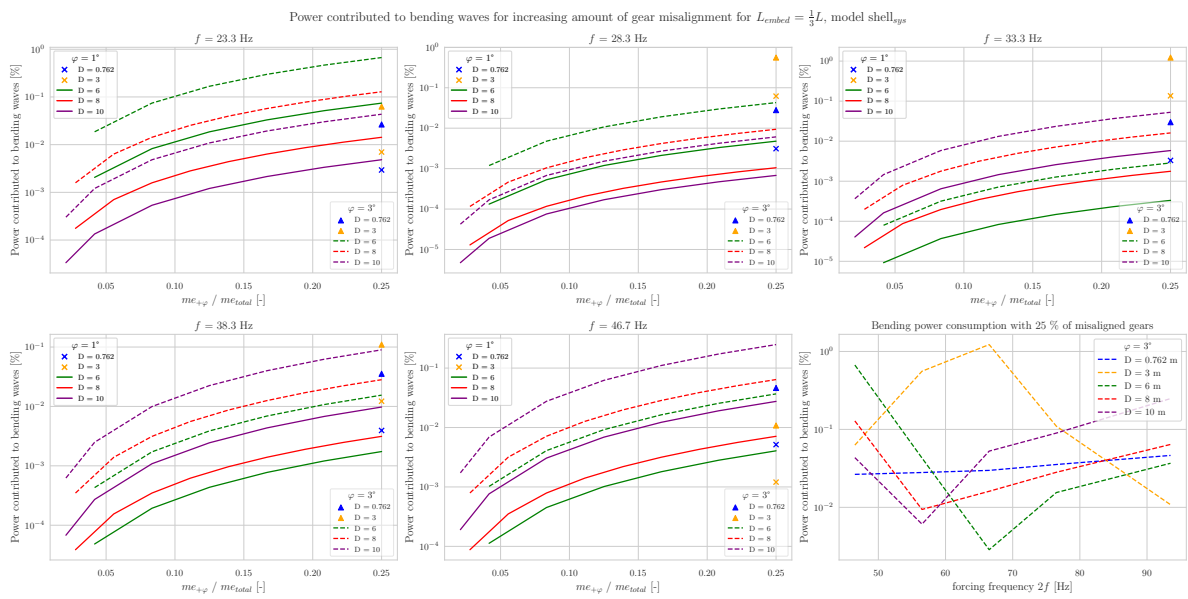
Figure B.7: Power consumed by bending vibrations with 25% of misaligned gears, $\varphi = 3°$, $L_{embed} = \frac{L}{3}$

Power consumption by bending vibrations for 25% misaligned gears, stiff soil
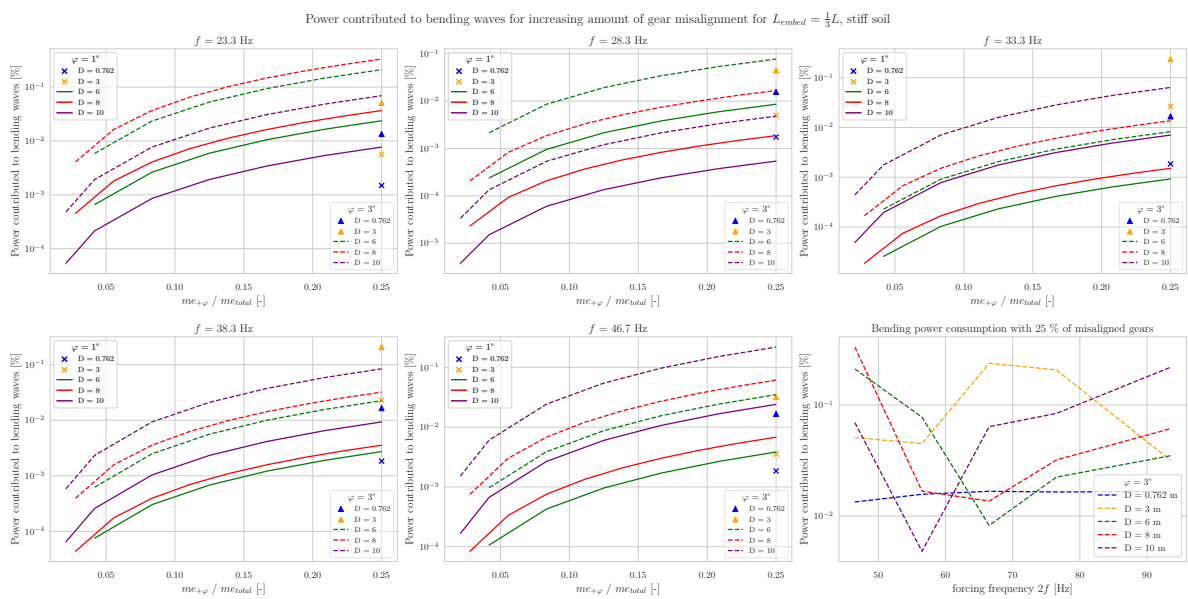
Figure B.8: Power consumed by bending vibrations with 25% of misaligned gears, $\varphi = 3°$, $L_{embed} = \frac{L}{3}$, stiff soil

Power consumption by bending vibrations for 50% misaligned gears, loose soil
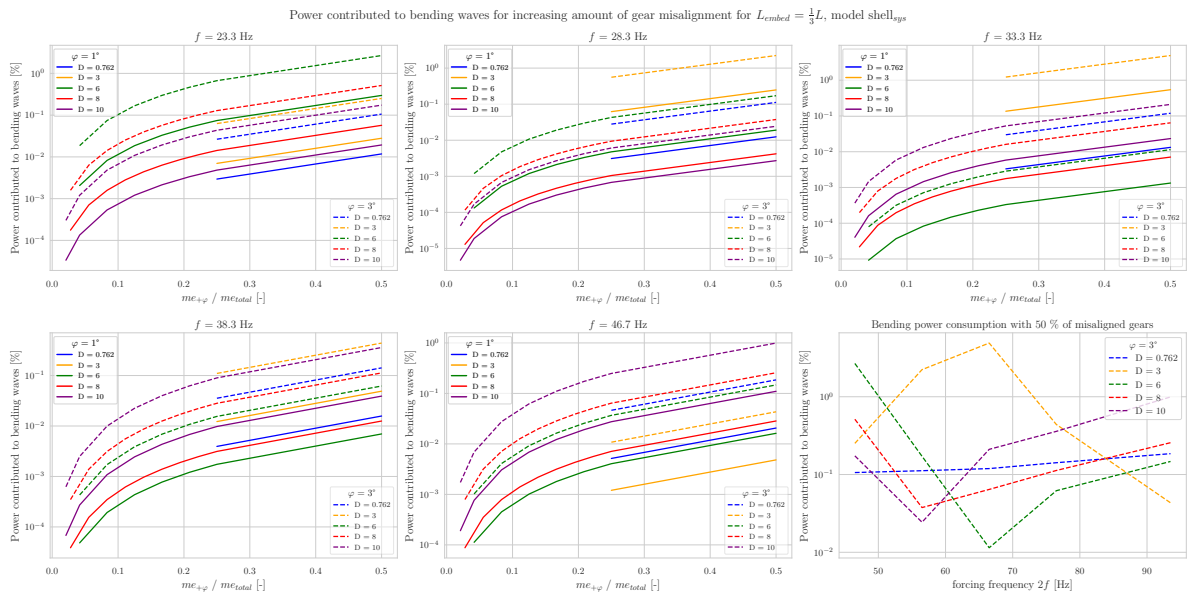
Figure B.9: Power consumed by bending vibrations with 50% of misaligned gears, $\varphi = 3°$, $L_{embed} = \frac{L}{3}$

Power consumption by bending vibrations for 50% misaligned gears, stiff soil
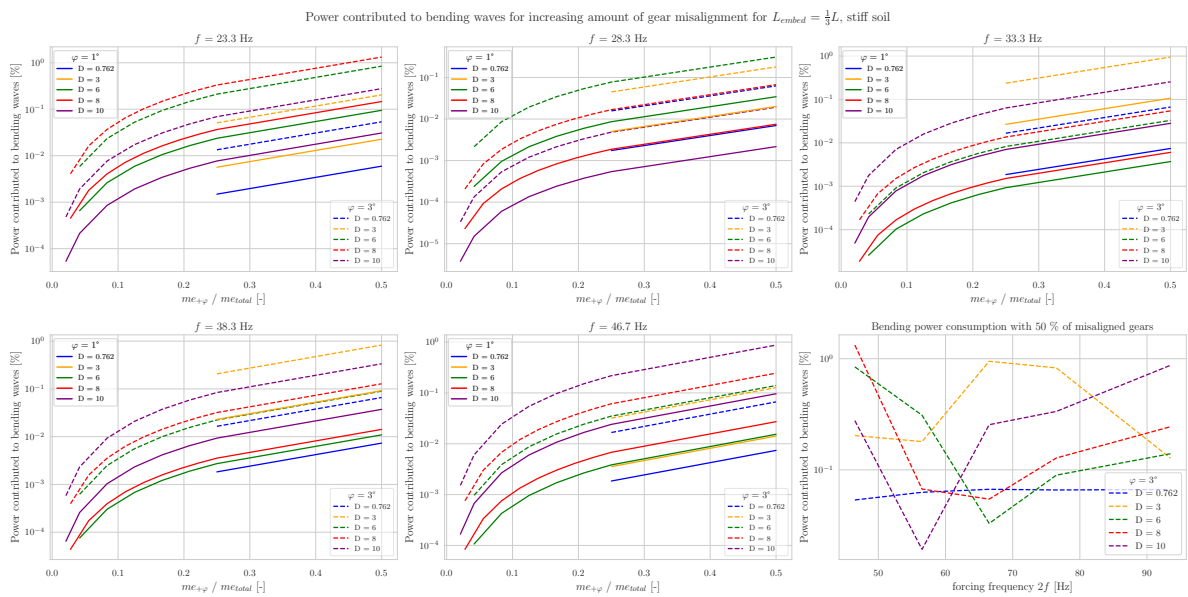
Figure B.10: Power consumed by bending vibrations with 50% of misaligned gears, $\varphi = 3°$, $L_{embed} = \frac{L}{3}$, stiff soil

Increase of power consumption by bending vibrations with increasing degree of misalignment
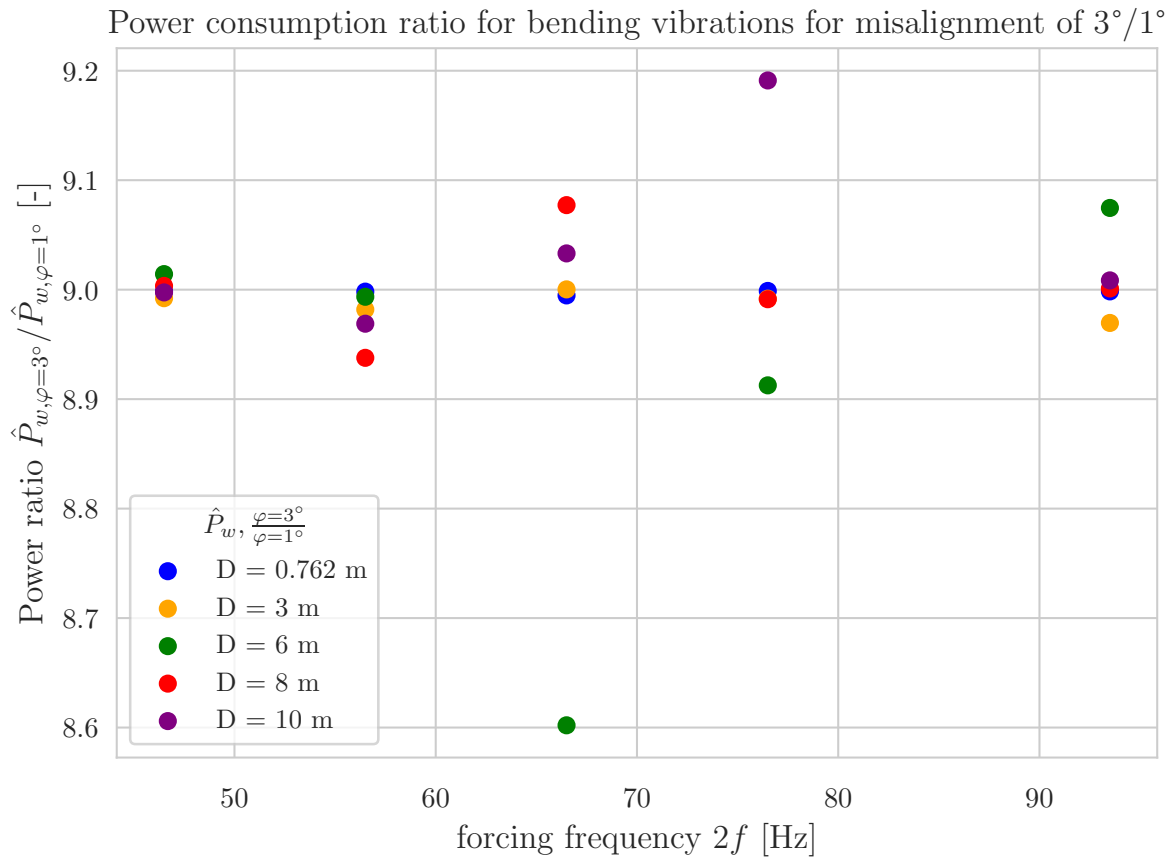
Figure B.11: Power consumption ratio in bending vibrations for various degrees of misalignment

Displacement contribution to bending for 25% misaligned gears, loose soil
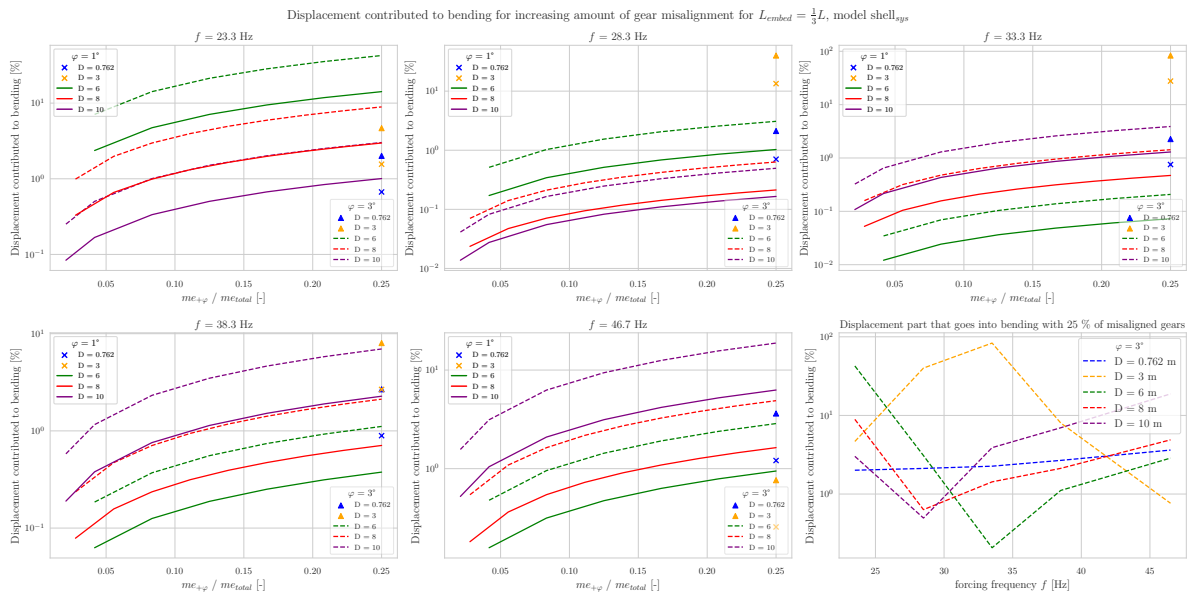
Figure B.12: Displacement ratio with increased amount of misaligned gears up to 25% of total gears, $\varphi = 3°$, $L_{embed} = \frac{L}{3}$

Displacement contribution to bending for 25% misaligned gears, stiff soil
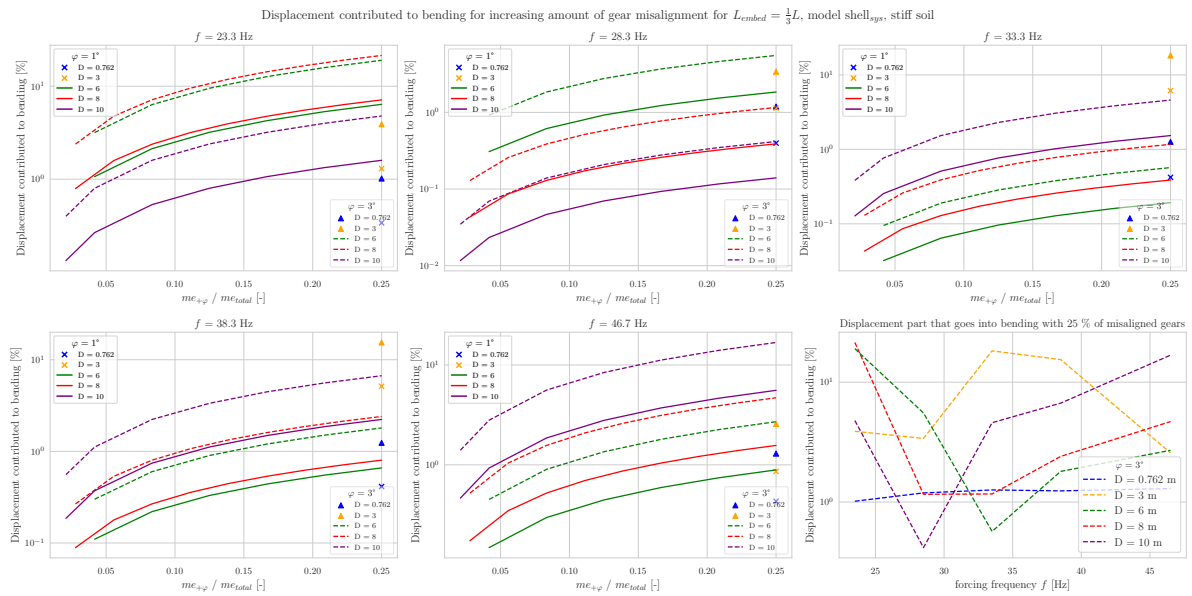
Figure B.13: Displacement ratio with increased amount of misaligned gears up to 25% of total gears, $\varphi = 3°$, $L_{embed} = \frac{L}{3}$, stiff soil

Displacement contribution to bending for 50% misaligned gears, loose soil
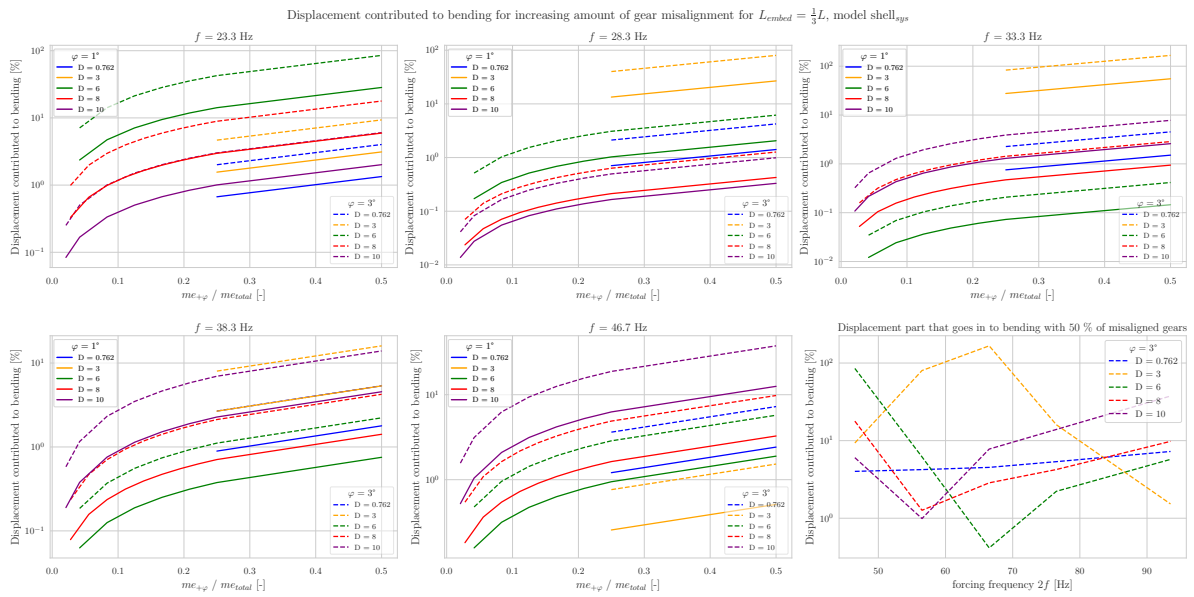
Figure B.14: Displacement ratio with increased amount of misaligned gears up to 50% of total gears, $\varphi = 3°$, $L_{embed} = \frac{L}{3}$

Displacement contribution to bending for 50% misaligned gears, stiff soil
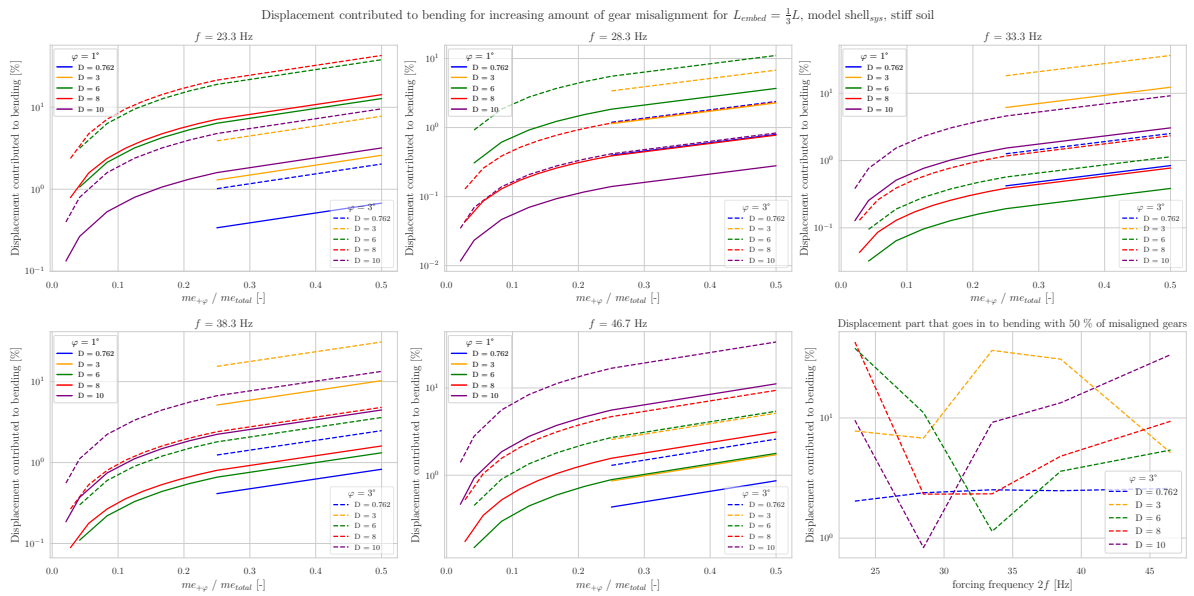
Figure B.15: Displacement ratio with increased amount of misaligned gears up to 50% of total gears, $\varphi = 3°$, $L_{embed} = \frac{L}{3}$, stiff soil

Increase of displacement contribution to bending with increasing degree of misalignment
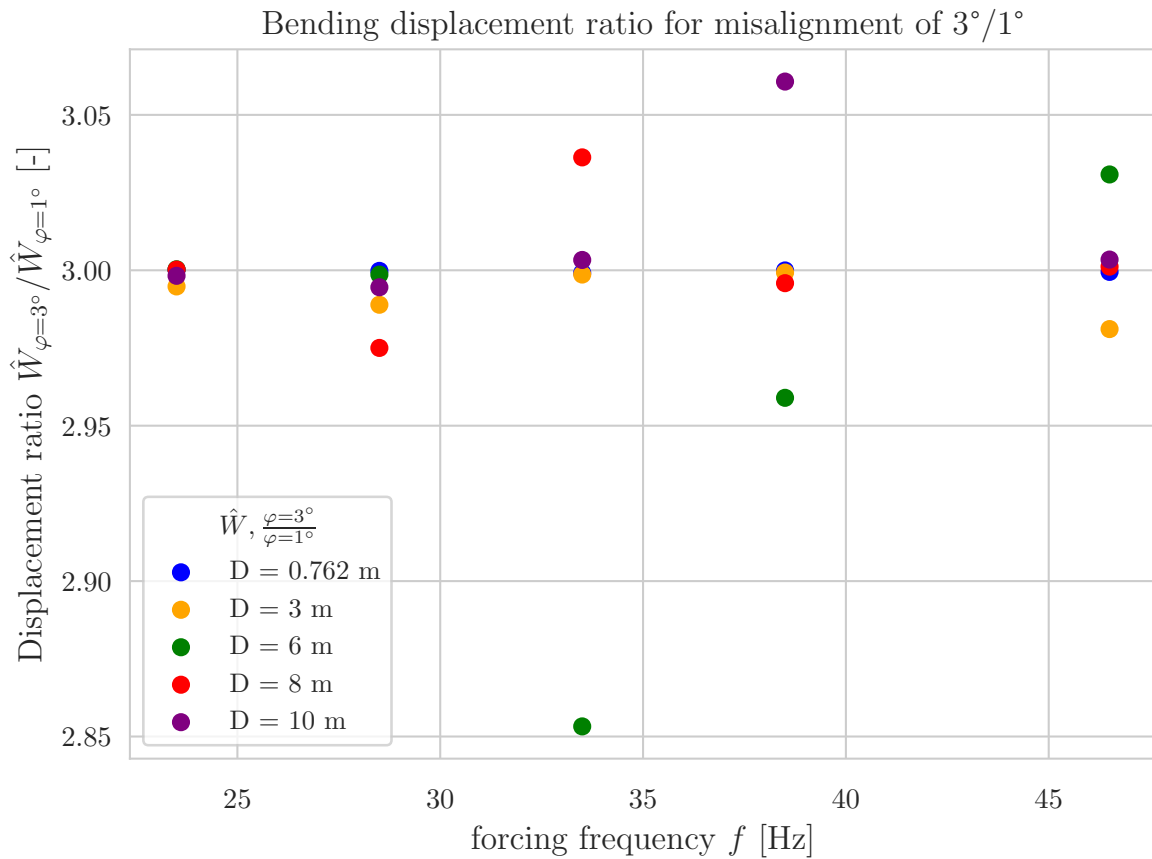
Figure B.16: Bending displacement ratio for various degrees of misalignment

Effect of embedment depth and soil stiffness on bending displacement contribution

(a) Displacement contributed to bending vibrations for all three embedment depths

(b) Displacement contributed to bending vibrations for all three embedment depths in stiffer soil
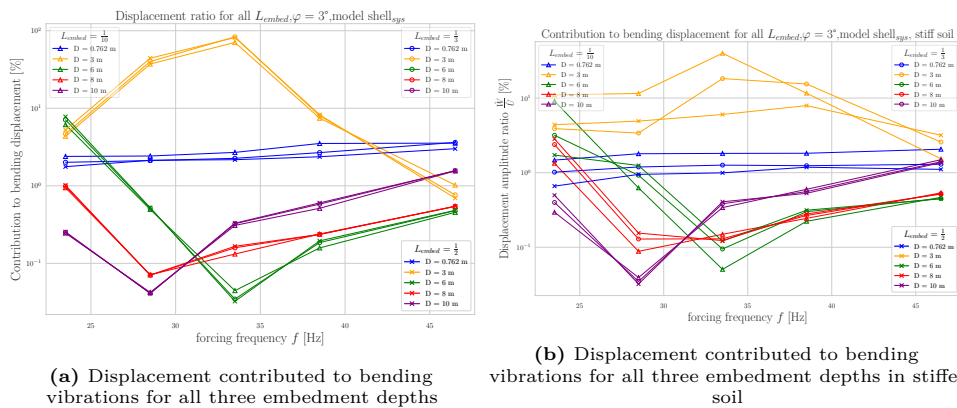
Figure B.17: The effect of embedment depth and soil stiffness on the displacement contribution to bending in **(a)** looser soil and **(b)** stiffer soil

B.0.3. Frequency and modal responses
Axial and bending frequency response
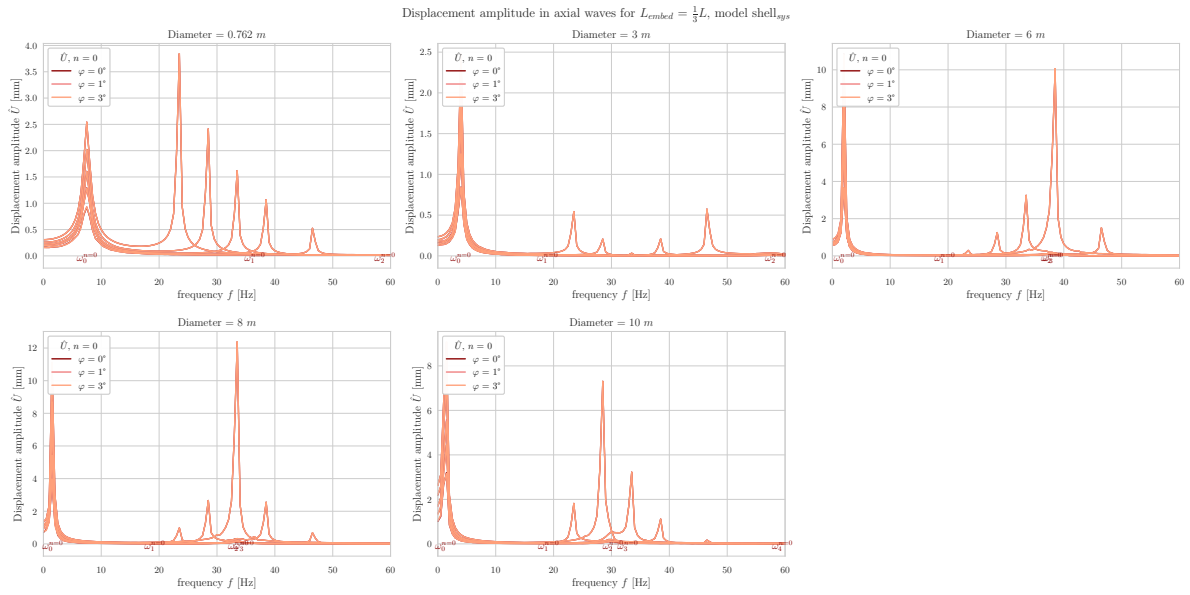
Figure B.18: Axial displacement frequency response
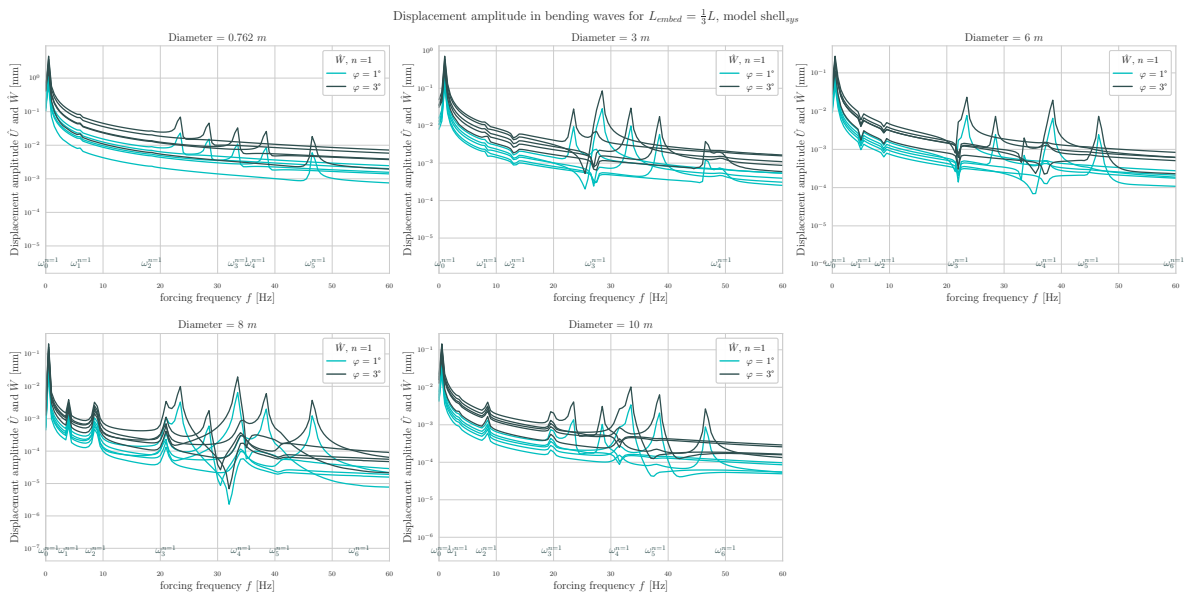
Figure B.19: Bending displacement frequency response

Axial and bending modal amplitudes and mode shapes for both soil types
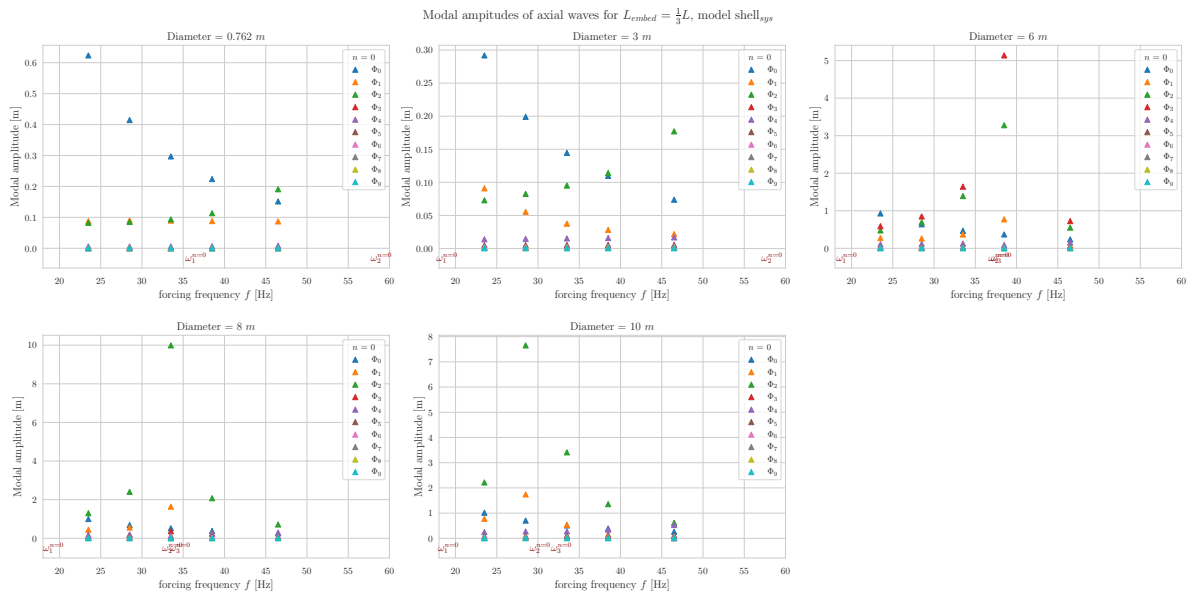
Figure B.20: Axial modal amplitudes
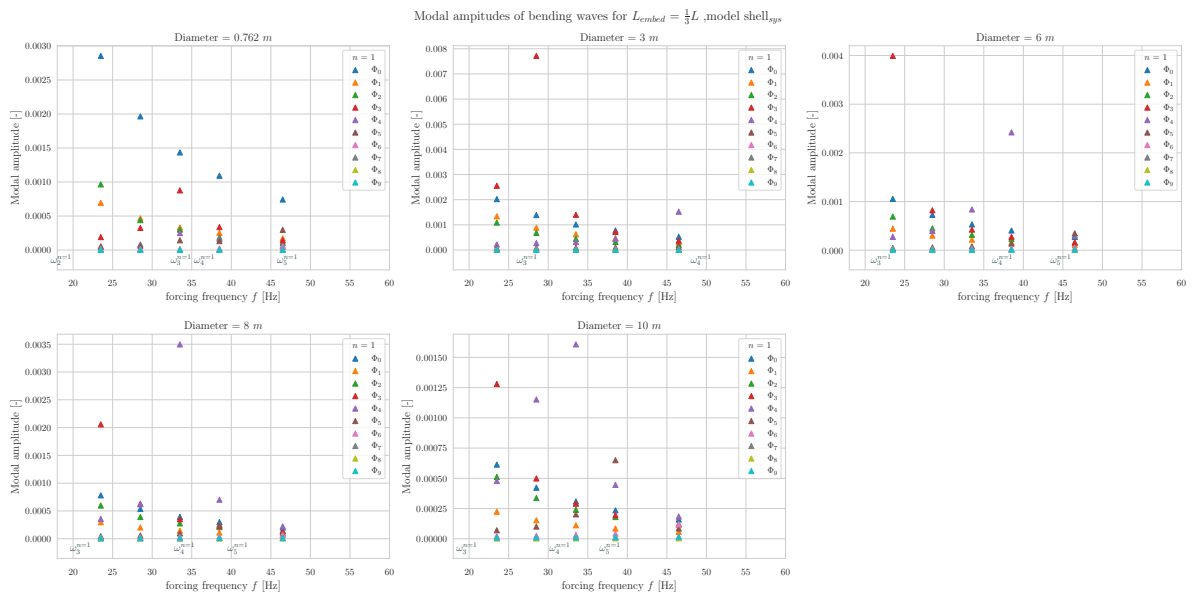
Figure B.21: Bending modal amplitudes

Mode shapes of axial waves for $L_{embed} = \frac{1}{3}L$, model shell$_{sys}$

Figure B.22: Axial mode shapes

Mode shapes of bending waves for $L_{embed} = \frac{1}{3}L$, model shell$_{sys}$

Figure B.23: Bending mode shapes
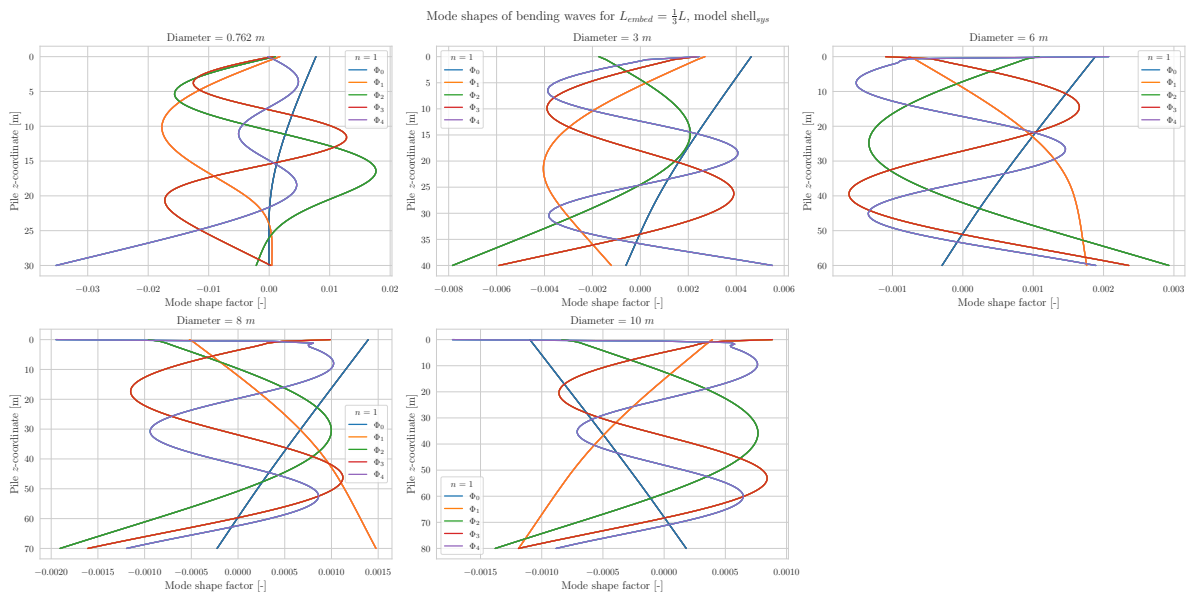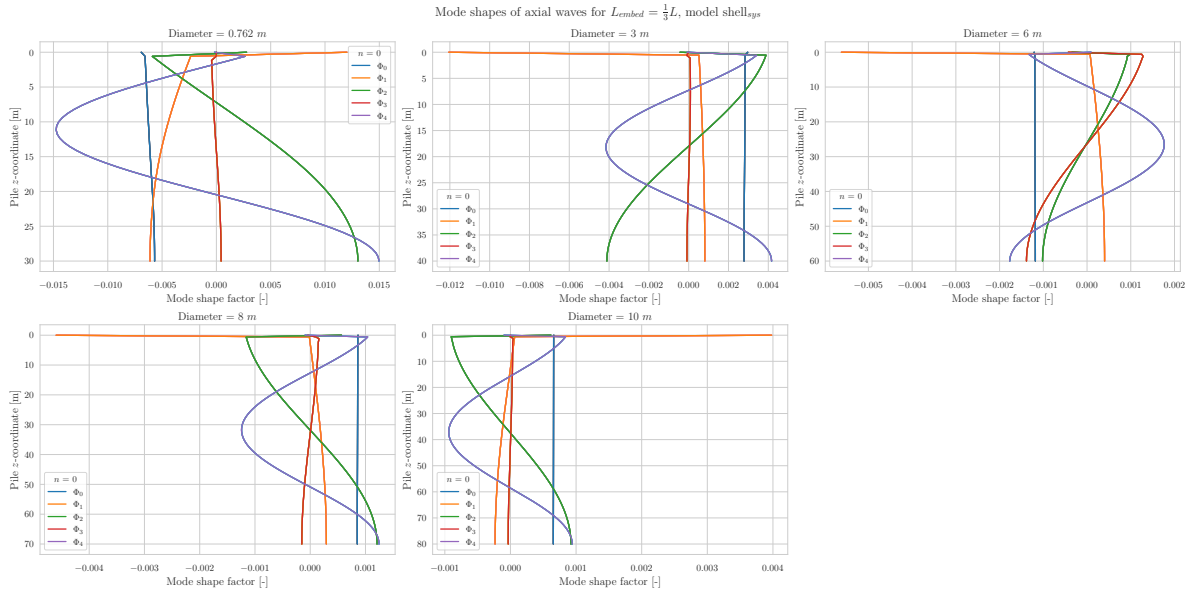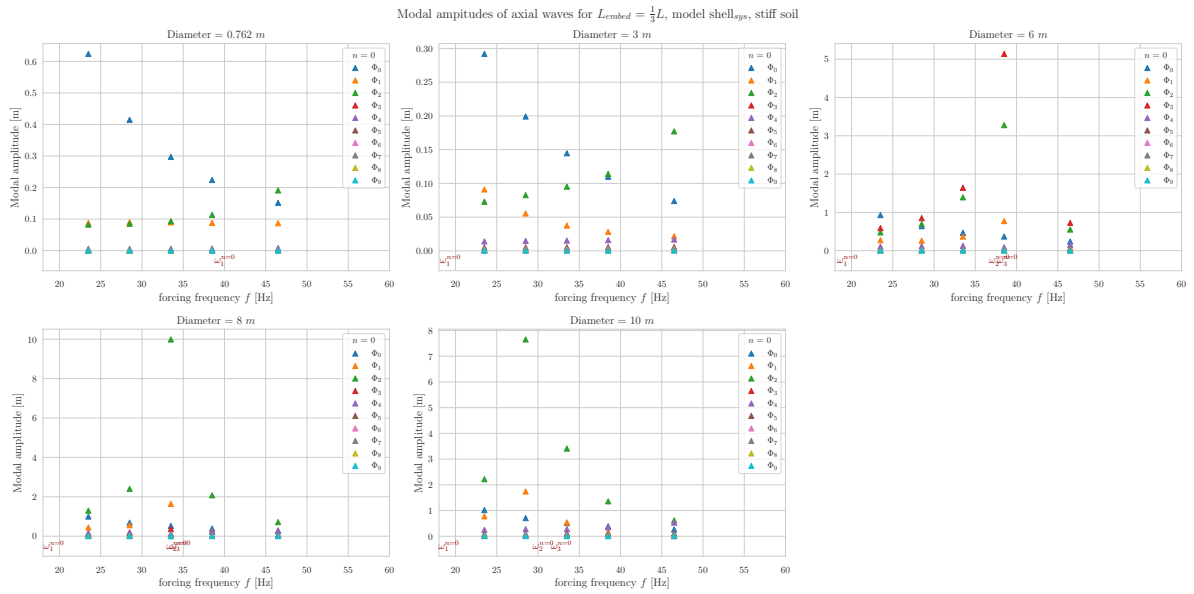
Figure B.24: Axial modal amplitudes, stiff soil
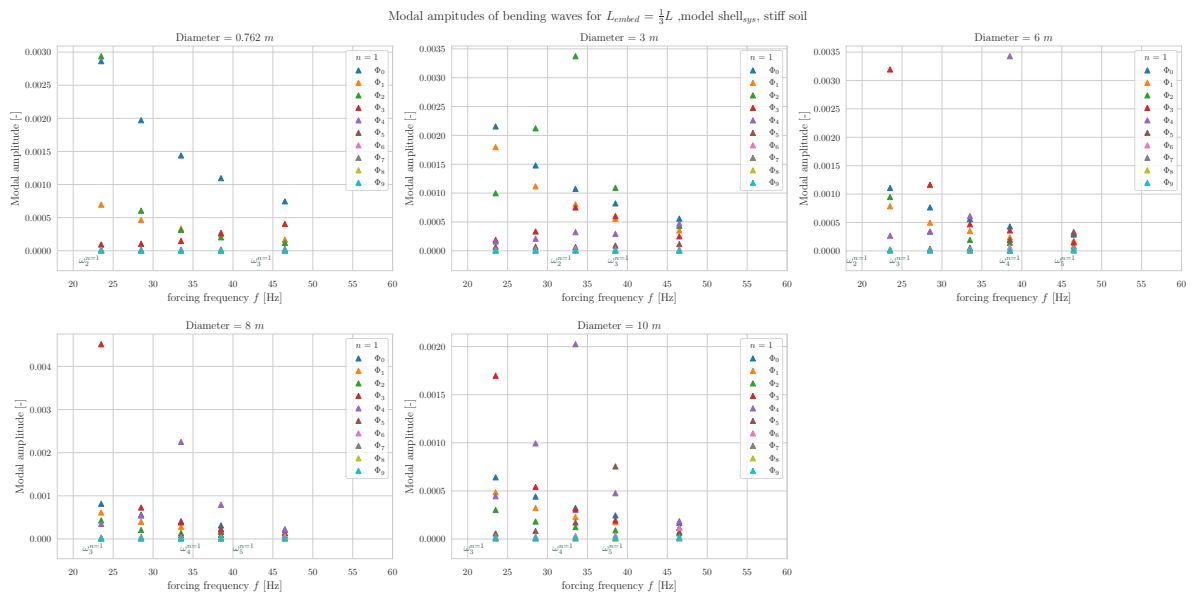
Figure B.25: Bending modal amplitudes, stiff soil

Figure B.26: Axial mode shapes, stiff soil

Figure B.27: Bending mode shapes, stiff soil
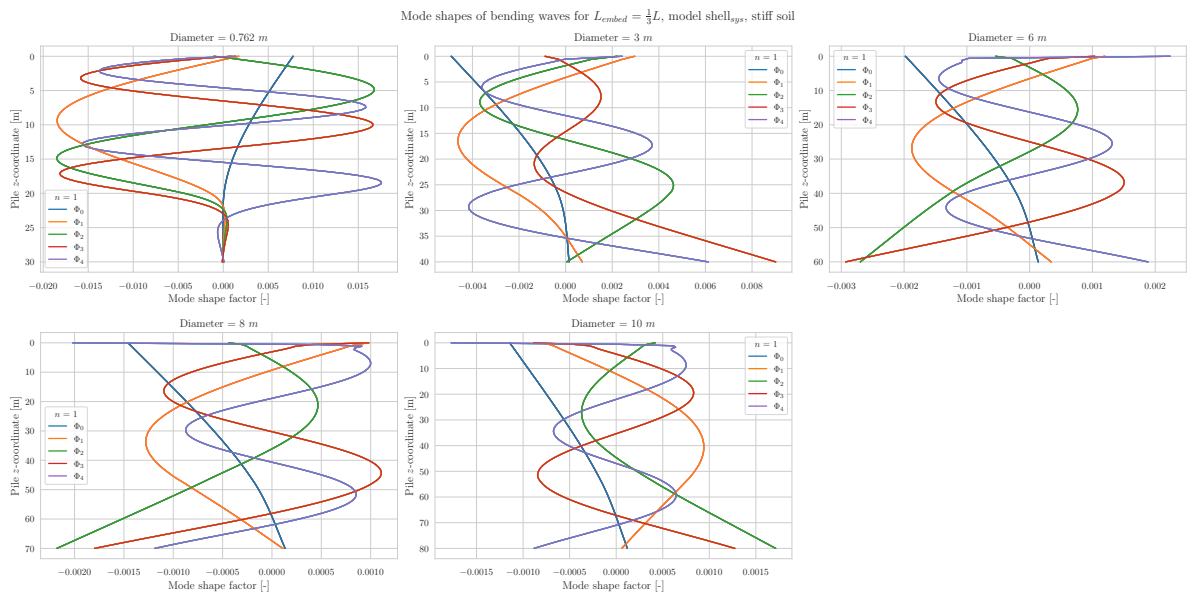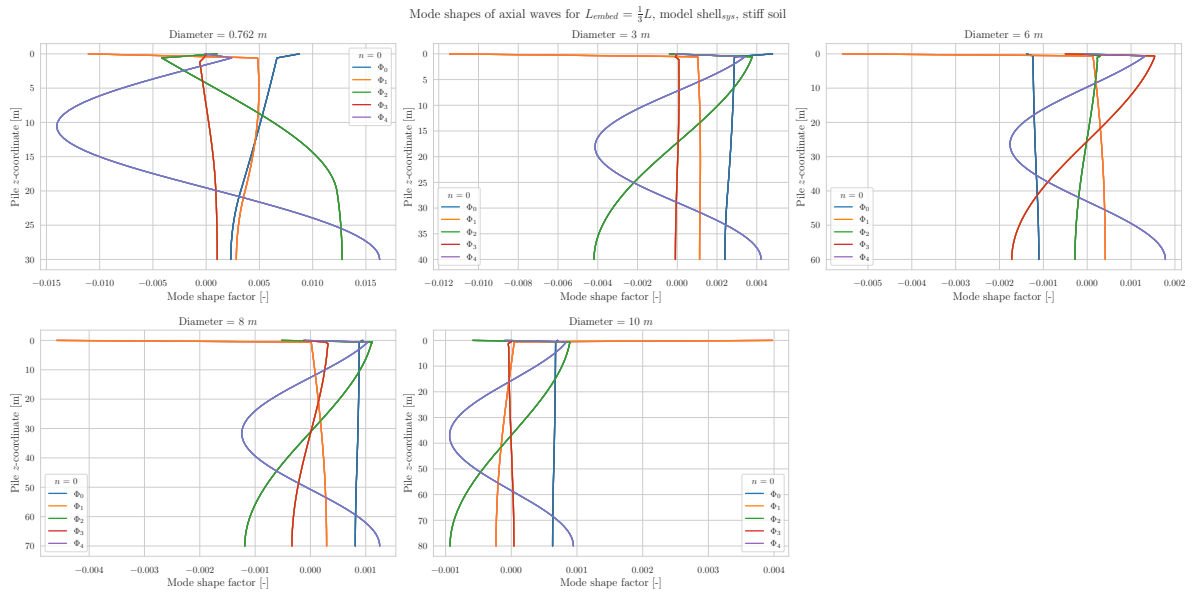
B.0.4. Force transfer for all embedment depths and soil types
Force transfer for all embedment depths, loose soil
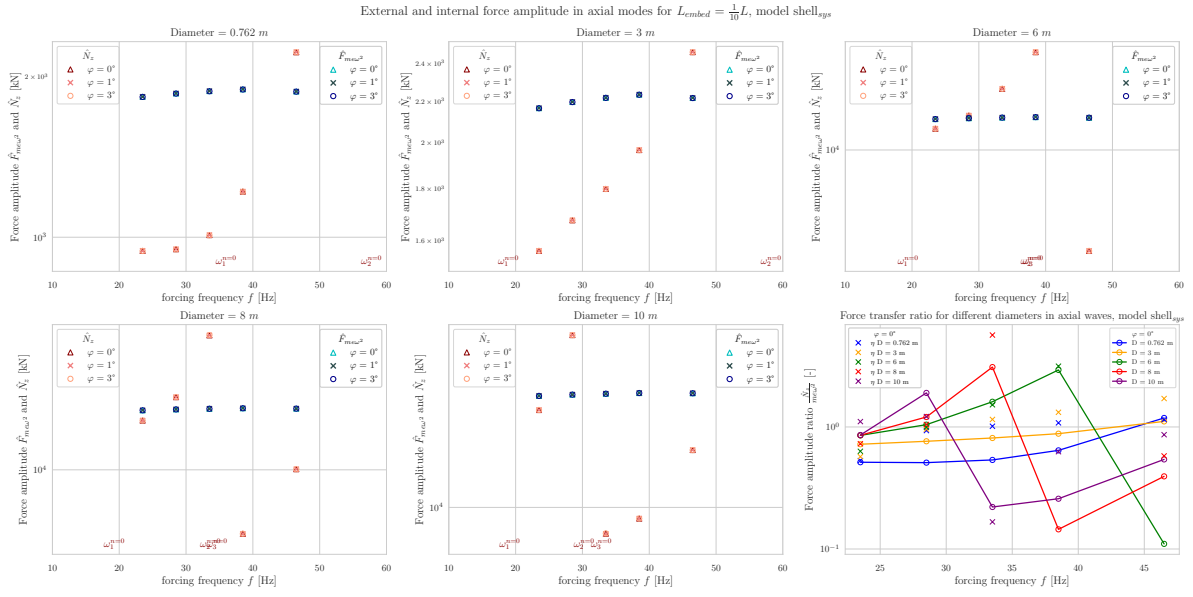
Figure B.28: Force transfer ratio, $L_{embed} = \frac{L}{10}$
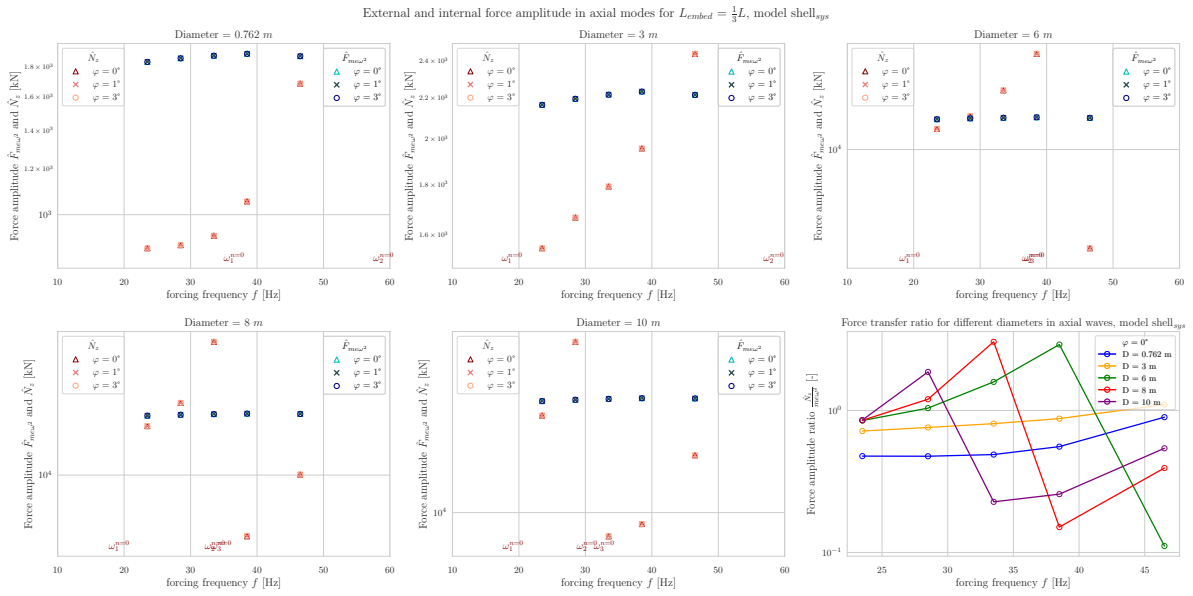
Figure B.29: Force transfer ratio, $L_{embed} = \frac{L}{3}$
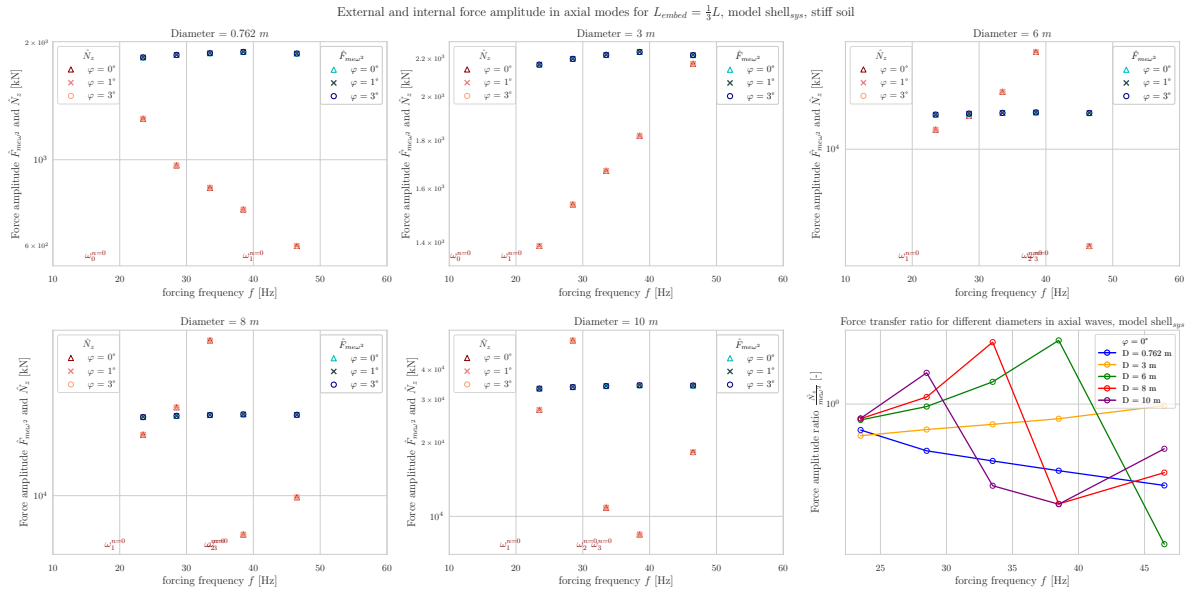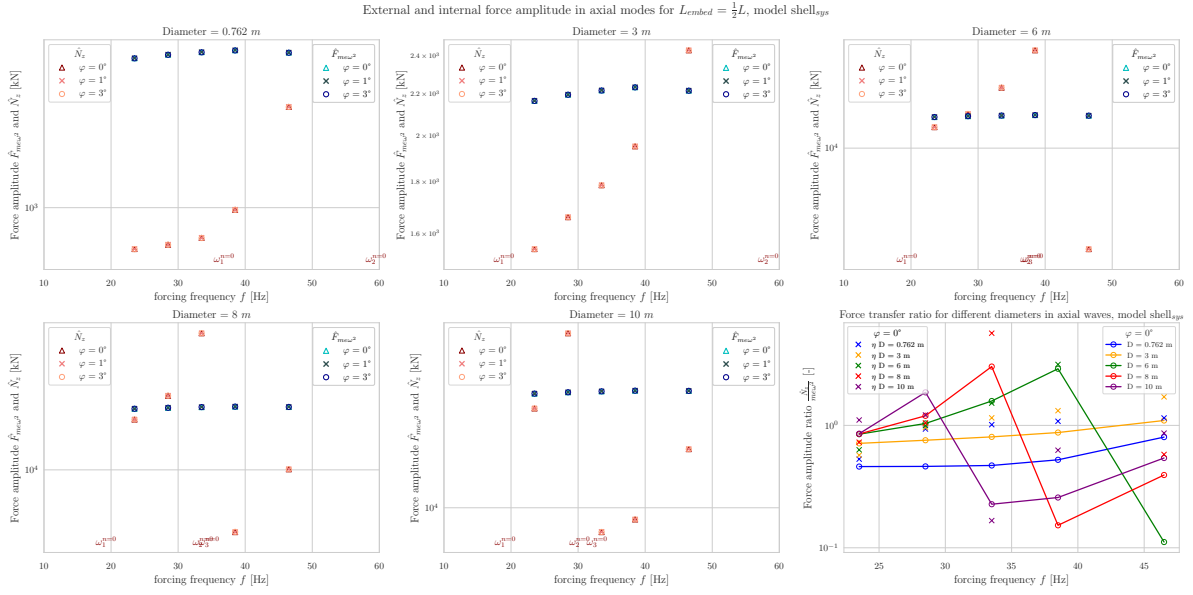
Figure B.30: Force transfer ratio, $L_{embed} = \frac{L}{2}$

Figure B.31: Force transfer ratio, $L_{embed} = \frac{L}{3}$, stiff soil

The output for other embedment depths for stiff soil is not included. The summary is given in Figure 4.7b.

B.0.5. Spring activation for all embedment depths and soil types
Spring activation for all embedment depths, loose soil
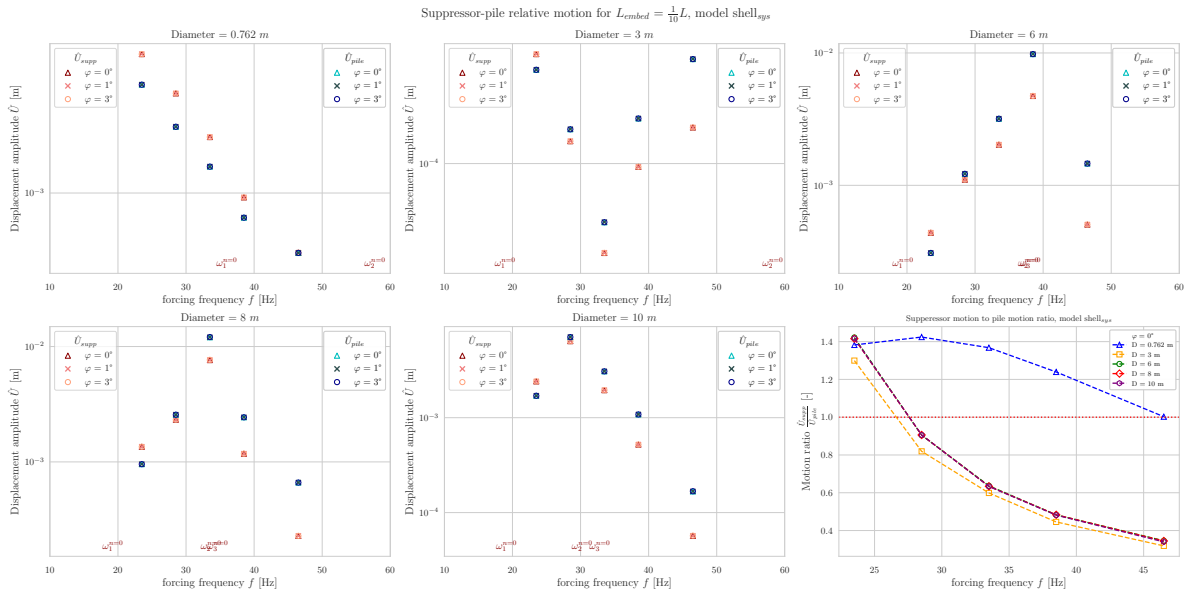
Figure B.32: Relative motion suppressor housing and pile head $L_{embed} = \frac{L}{10}$
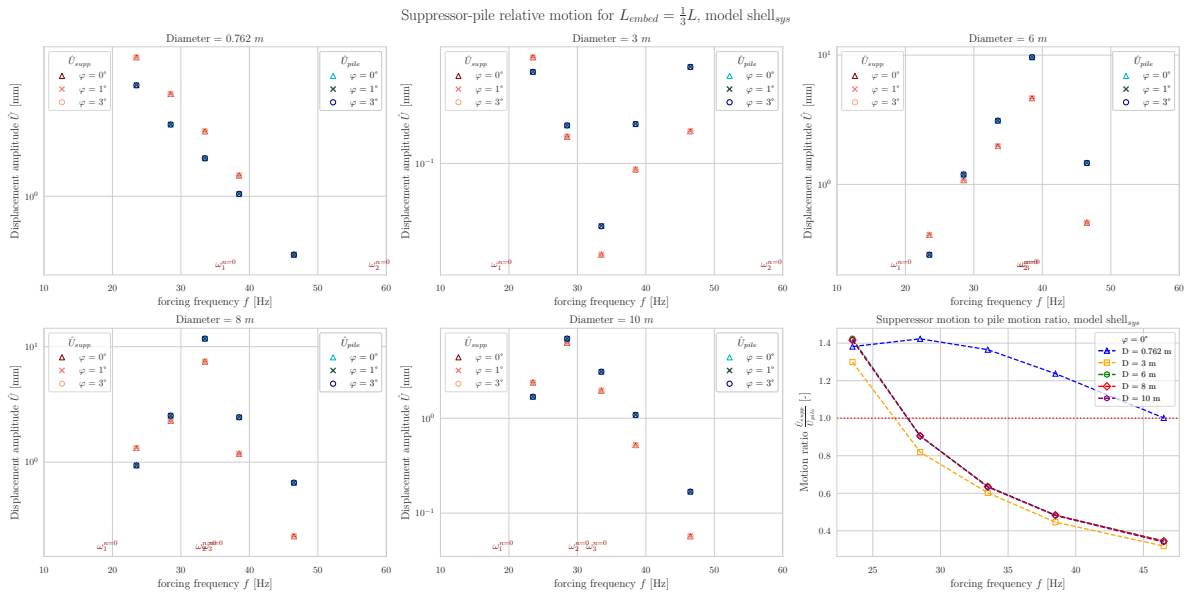
Figure B.33: Relative motion suppressor housing and pile head $L_{embed} = \frac{L}{3}$
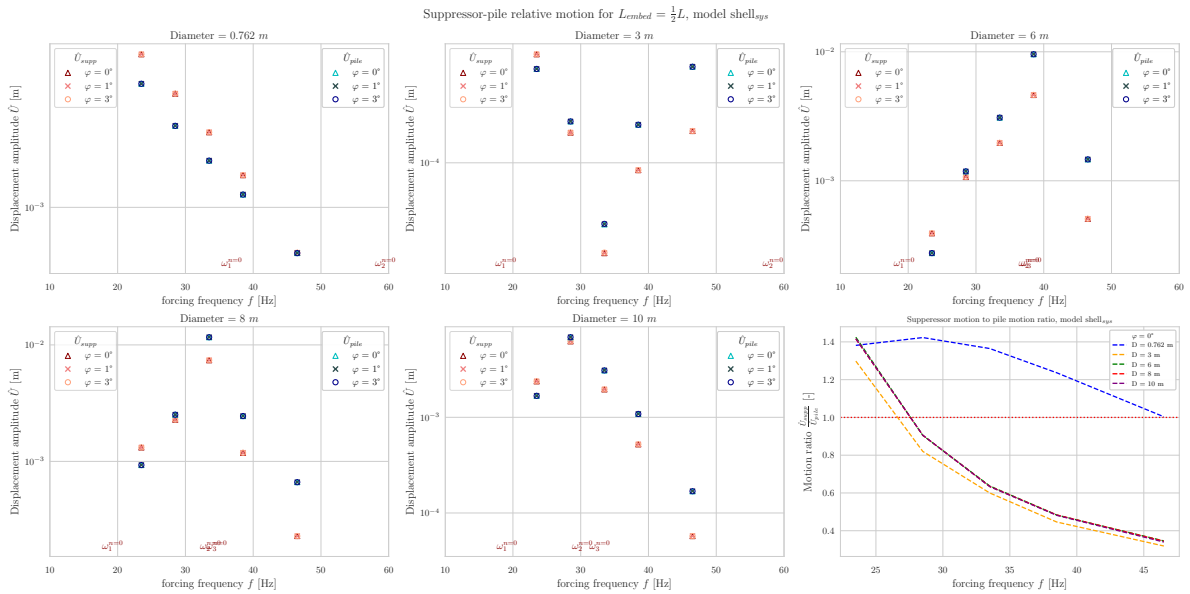
Figure B.34: Relative motion suppressor housing and pile head $L_{embed} = \frac{L}{2}$

Spring activation for all embedment depths, stiff soil
The output for other embedment depths for stiff soil is not included. The summary is given in Figure 4.10b.

B.0.6. Power consumption by bending-like motions for all embedment depths and soil types

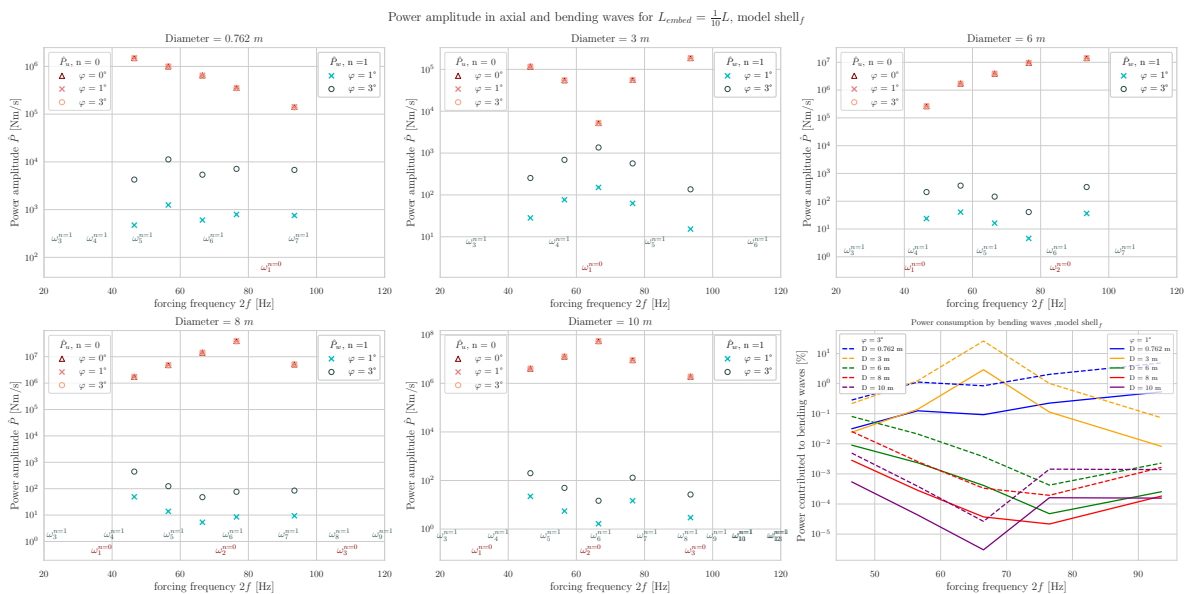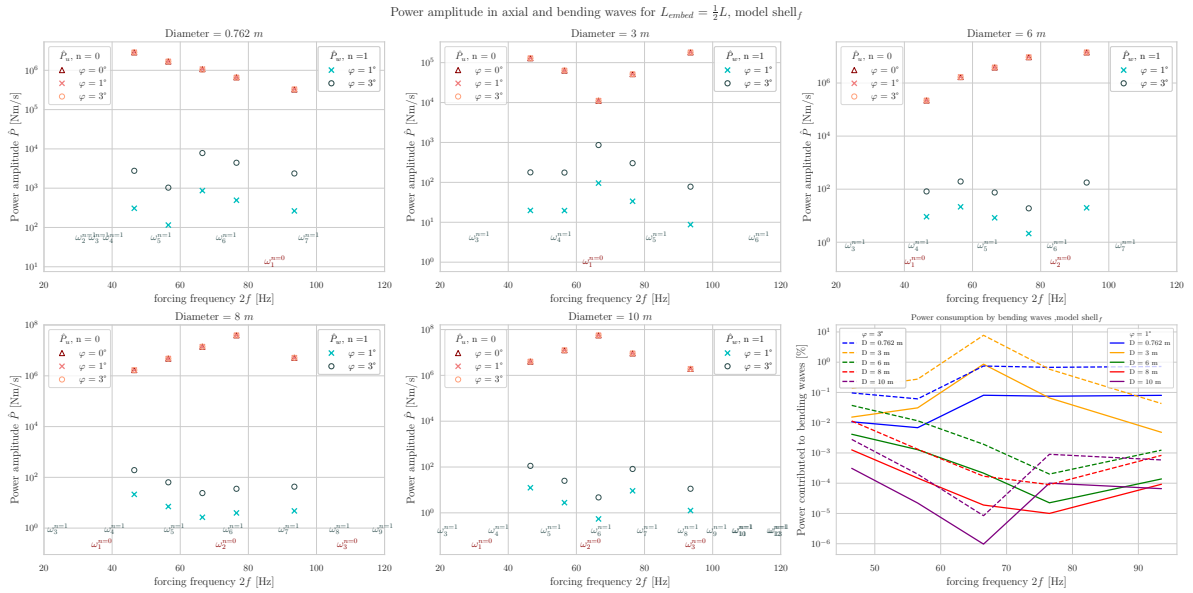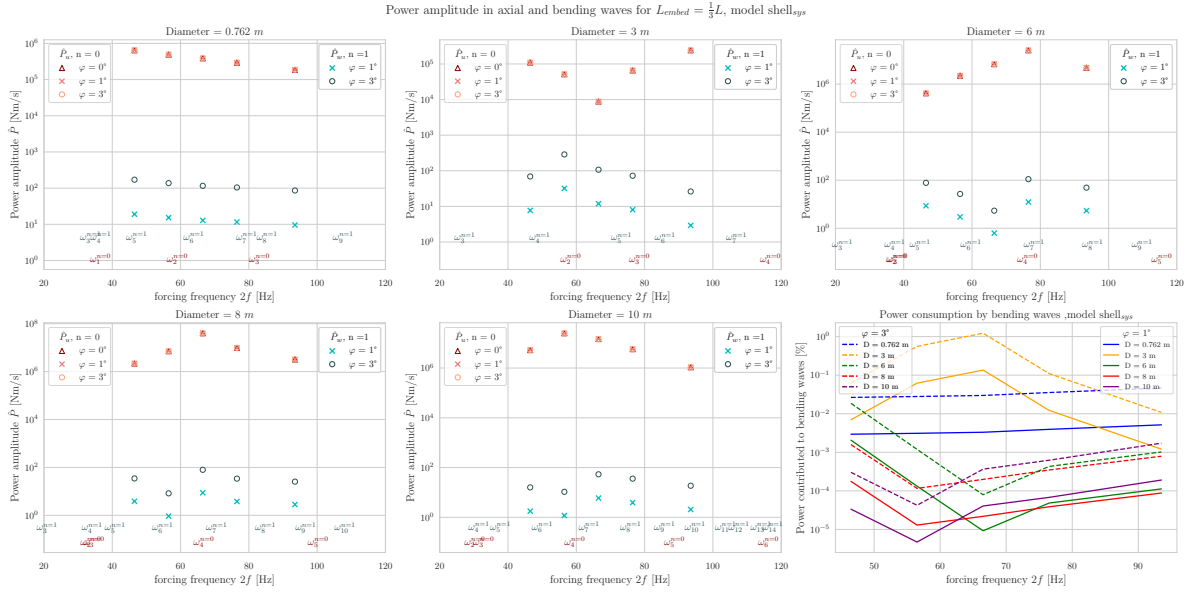**Power consumption by bending-like motions for all embedment depths, loose soil**

Figure B.35: Power consumption by bending-like motion, $L_{embed} = \frac{L}{10}$

Figure B.36: Power consumption by bending-like motion, $L_{embed} = \frac{L}{3}$

Figure B.37: Power consumption by bending-like motion, $L_{embed} = \frac{L}{2}$

The output for other embedment depths for stiff soil is not included. The summary is given in Figure 4.12b.

B.0.7. Bending-like displacement contribution for all embedment depths and soil types

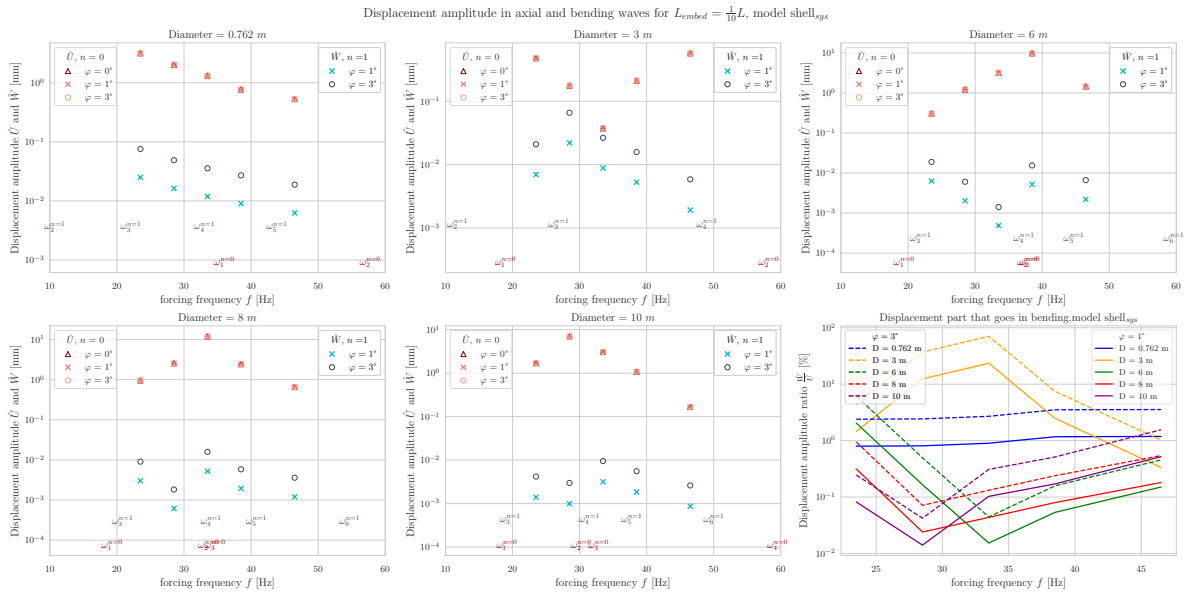**Bending-like displacement contribution for all embedment depths,loose soil**

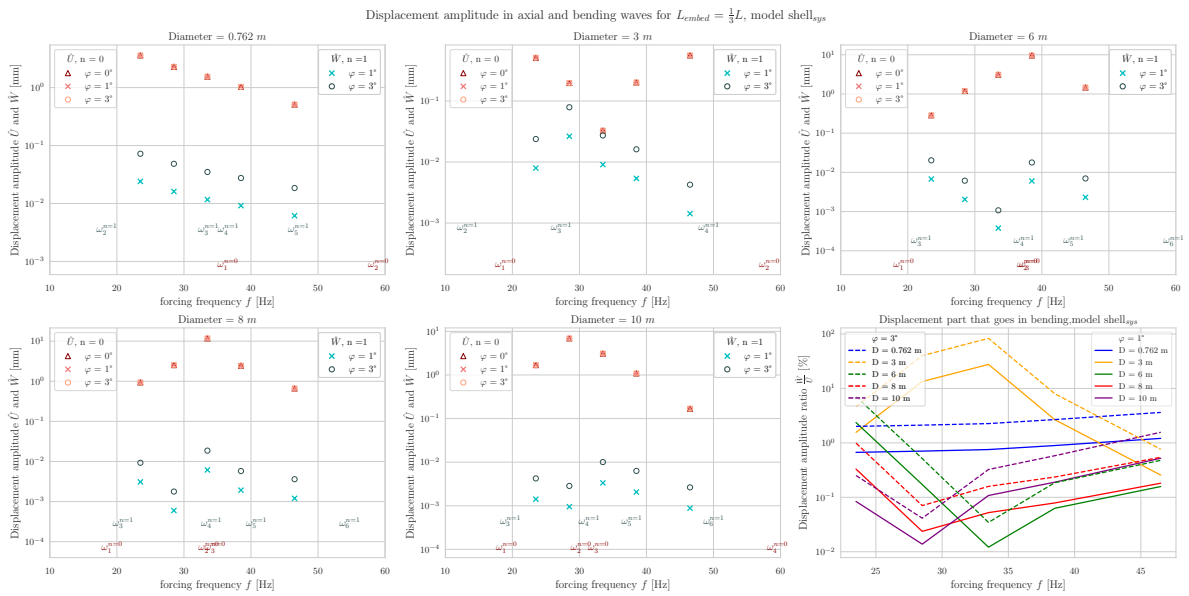**Figure B.38:** Displacement contributed to bending-like motion, $L_{embed} = \frac{L}{10}$

Figure B.39: Displacement contributed to bending-like motion, $L_{embed} = \frac{L}{3}$
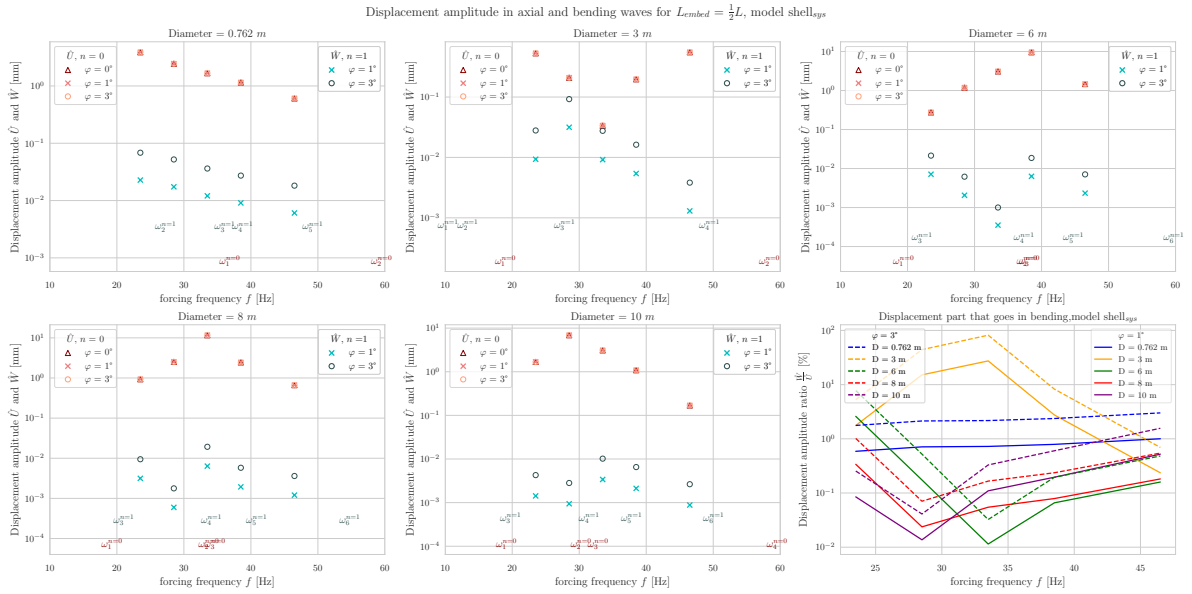
Figure B.40: Displacement contributed to bending-like motion, $L_{embed} = \frac{L}{2}$

The output for other embedment depths for stiff soil is not included. The summary is given in Figure B.17b.